5-2016

# Defect Assisted Growth of Copper-Silicide Nanostructures on Si(100) and Si(111)

Endu Sekhar Srinadhu
*Clemson University*, esrinad@clemson.edu

# Defect Assisted Growth of Copper-Silicide Nanostructures on Si(100) and Si(111)

---

A Dissertation
Presented to
the Graduate School of
Clemson University

---

In Partial Fulfillment
of the Requirements for the Degree
Doctor of Philosophy
Physics

---

by
Endu Sekhar Srinadhu
May 2016

---

Accepted by:
Dr. Chad Sosolik, Committee Chair
Dr. Endre Takacs
Dr. Catalina Marinescu
Dr. William R Harrell

# Abstract

As the dimensions of the smallest feature on the integrated circuit has miniaturized into the range of tens of nanometers, patterning of highly ordered nanostructures with tunable size and shape in large scale on the surface of substrate is highly demanding and increasingly challenges the limits of nanolithography. To overcome the conventional lithographic limitations, self assembled methods have been explored. While strain driven self assembly is widely viewed as a promising technique for patterning at the nanoscale, to follow this approach and create structures in a desired manner, a reliable means to engineer and characterize the shape and sizes of nanostructures during self assembly is essential. The work presented here describes a detailed analysis of the morphological and compositional evolution of patterns in $Cu_3Si$ strain-driven self assembles.

The first project described in this thesis is the fabrication of self assembled copper silicide nanostructures on $SiO_2$/Si(111) and $SiO_2$/Si(100) with electron beam evaporation in ultrahigh vacuum. The copper silicide growth was determined to be defect assisted. In order to create defect sites or voids at the surface, the $SiO_2$/Si substrates in this work were annealed at 500°C for 10-12 hours in a vacuum system prior to the deposition of Cu. The development of these nucleation centers or voids at the surface is discussed along with the deposition of Cu at low temperatures ($T < 450$°C) and the deposition of Cu and growth of nanostructures in an optimal

temperature range (450°C < T < 600°C). The variation in the density of voids at the sample surfaces was investigated with SEM-EDS and XRD techniques. Copper silicide phase and orientation of nanostructures were investigated with SEM-EDAX techniques. For the growth of $Cu_3Si$ nanostructures on $SiO_2$/Si(111), equilateral triangles of various sizes were found to grow up to a critical size, beyond which the shape transitioned from equilateral triangular to trapezoid. For $Cu_3Si$ nanostructures on the $SiO_2$/Si(100) surface, square islands were found to grow up to a critical size, beyond which rectangular islands and long nanowires were formed. A growth mechanisms for $Cu_3Si$ nanostructures based on the strain induced shape transition growth model is discussed.

The second project discussed in this thesis is the nanopatterning of self assembled copper silicide nanostructures on $SiO_2$/Si(111) and $SiO_2$/Si(100) with highly charged ion beams (HCIs) of argon. Since the void creation at surface using the thermal annealing technique requires long times, we investigated the use of highly charge ion beams to induce defect sites on the surface of the substrate. $Ar^{q+}$ ion beams of varying fluence and charge state (q=1,4,8) were used to produce nucleation centers or voids at the surface of $SiO_2$/Si substrates. This approach could provide an alternative method for probing the sputter yields of HCI irradiated oxides. The deposition of Cu and the growth of nanostructures at an optimal temperature of 600°C are discussed. The variation in the density and orientation of $Cu_3Si$ nanostructures as a function of HCI charge state and fluence were investigated with the SEM-EDS technique. For the growth of $Cu_3Si$ nanostructures on $SiO_2$/p-Si(111) and on $SiO_2$/p-Si(100) surfaces, square islands have been found to grow up to a critical size, beyond which rectangular islands and long nanowires were formed. In general, the growth results were similar to the previous study. However, the size and hence the growth rate was significantly longer.

The final project presented in this thesis is modification of the surface properties of polycarbonate with HCIs. Polycarbonate (PC, Lexan) has many industrial applications because of its excellent transparency and high impact resistance. However, PC requires a surface modification to improve adhesion for metallization and optical applications. The surface of PC samples were irradiated with highly charged ion beams of argon and oxygen in order to understand the role of low energy HCIs on the surface modification. Surface characterization of PC prior to and after HCI irradiation was performed using the XPS technique. Chain scission and cross linking were determined to occur during the HCI polymer interaction. The change in the relative intensities of C-C,C-O and C=O functional groups with HCI species, charge state and fluence were discussed. An increase in the relative intensities of C-O, C=O and a decrease in C-C bond intensities were discussed in terms of potential energy dependent sputtering.

# Dedication

To my parents, Mr. Bangaru Setti and Mrs. Padmavathi, without whose support, love and encouragement this task would have been impossible.

# Acknowledgments

In the course of a long graduate career, one acquires a debt to many people who have made it all possible. I learned a lot of things from a lot of people, and it was of course more than just about physics. I will start by saying: Thank you to everyone who has been around me, and if I fail to list your name here, it is really my failure, and I apologize to those that I am surely likely to forget.

Foremost among the people, I want to acknowledge my advisor Dr. Chad Sosolik for giving me an opportunity to work in his lab. Without his guidance, technical expertise and motivation, none of this work would have been possible. I would also like to thank him for providing access to AMRL imaging facility, enabling me to pursue internship at Applied Materials, and his endless patience when reading manuscripts. I would also like to thank my committee members Dr. Endre Takacs, Dr. Catalina Marinescu and Dr. William R Harrell for their insights, comments and suggestions. Much appreciation also goes to Dr. Jim Harriss for his support during my research work. He has provided me with all of the silicon wafers needed for this work and also supported me with oxidation and dicing of the wafers. I would also like to thank Department of Physics for providing me teaching assistantship during my PhD.

Thanks to all the past and current members of the SINS group. Thanking in just a few words after working with them for several years is the hardest part.

Especially i would like to thank Radhey Shyam, Daniel Field, Dhruva Kulkarni, Jason Puls and Selcuk Temiz. They have been a wonderful group of people to work with and they definitely made my life in the lab more enjoyable. A special thanks to Lamar Durham, Jon Simpson in the Physics and Astronomy machine shop for their help.

Moving on to those who are thousands of miles away, thanks to my parents for their love and support. I extend my deepest gratitude to my father for his staunch support, invaluable guidance and work ethic, was in many ways a great role model. My mother deserves much of the credit for who I am today. I doubt that I could ever pay her back for all that she had done, no matter how hard I tried. I am indebted to my brother, Mr. Ram Kiran, for supporting me financially, keeping me sane and was quite confident in my abilities. My sister, Mrs. Satya Vani, and their two little kids are always special. I would like to thank her for reminding me that there is life outside of the laboratory. Thank you to the rest of my family for all of your love and support.

# Contents

# List of Tables

# List of Figures

# Chapter 1

# Introduction

## 1.1 Background and Motivation

Metal silicon interactions and the growth of silicides are important both to fundamental science and to the semiconductor industry. A metal silicide is a compound formed by deposition of metal on silicon followed by thermal annealing, laser irradiation or ion beam mixing. It may possess several phases and its equilibrium phase depends on the stoichiometry and temperature. Metal silicides are versatile and driven by their excellent electrical and mechanical properties suitable for applications such as ohmic contacts, Schottky barrier contacts, interconnects and diffusion barriers, have been widely researched and used in the microelectronics industry [1, 2]. At present, three silicides are widely used for applications such as interconnects and contacts in micro electronic industry, namely $TiSi_2$, $CoSi_2$ and $NiSi_2$ [1, 3–7]. For example, magnetic silicides such as $FeSi_2$ were studies for its excellent thermoelectric and photovoltaic properties [8–10]. Metal silicides also exhibit novel properties in nanoscale, which are in particular important for the development of nanoscale devices. Many physical and chemical properties can be greatly enhanced when a structure is

reduced to sufficiently small dimensions nanostructures. Thin metal silicdes are easy to fabricate and they are generally metallic[11–13]. As the dimensions of the smallest feature on the integrated circuit has miniaturized into the range of tens of nanometers, patterning of highly ordered nanostructures with tunable size and shape in large scale on the surface of substrate is highly demanding and increasingly challenges the limits of nanolithography. To overcome the conventional lithographic limitations, self assembled methods have been also explored. While self assembly is widely viewed as a promising technique for patterning at the nanoscale, to follow this approach an create structures in a desired manner, a reliable means to engineer and characterize the shape and sizes of nanostructures during self assembly is essential. With the current available technology, self assembled metal silicides can be fabricated in the nanoscale regime.

Although many metals will form silicides, studies of metal silicide nanostructures are mostly focused on a few CMOS compatible metals such as NiSi, $TiSi_2$, $CoSi_2$, $NiSi_2$, $TaSi_2$, $PtSi_2$, PtSi, $FeSi_2$, FeSi etc [1, 3–8, 14–16]. Metal silicide films can be grown epitaxially through techniques such as molecular beam epitaxy (MBE), solid phase epitaxy (SPE) and reactive deposition epitaxy (RDE). Generally a metal silicide phase is achieved by depositing metal on sa ilicon surface at high temperature (RDE) or depositing the metal at room temperature followed by high temperature annealing (SPE). In the literature metal silicides deposited on Si exhibiting different growth morphologies have been reported. Several possible reasons proposed to explain the growth morphology included stress induced shape transition, endotaxy, anisotropic lattice mismatch, island edge diffusion and creation of dislocations. However the growth of metal silicides on silicon substrates capped with ultrathin oxide layer has not been explored. In this thesis, we aim to address the following: (1) what are the types of nanostructures that can form on $SiO_2$/Si substrates of (111) and

(100) orientations with p and n type dopants? (2) What is the optimum temperature for the growth of silicides? (3) What is the growth mechanism responsible for the formation of different shaped nanostructures? (4) Do the islands form above the substrate (epitaxy) or below the substrate(endotaxy)? (5) Is the growth of each type of silicide influenced by strain? Addressing these issues will help us better understand the growth process involved in the formation of silicide nanostructures.

We note that other CMOS compatible metals such as Cu, which is widely available and more commonly found in IC technology are less studied. Cu offers lower resistivity than $CoSi_2$ and NiSi and can easily diffuse into Si and forms copper silicide ($Cu_3Si$). Cu-Si has been researched extensively due to its applications in energy storage devices such as batteries, solar cells etc. Recently its use has been studied for possible anodes in energy storage technology. Kaiqi *et al*. showed that an excellent electrochemical performance was obtained in a Si-$Cu_3Si$-Cu composite electrode [17]. It is also shown recently that Cu-Si nanowires exhibit superior field-emission properties and serve as highly efficient anti-reflective layers. It is also known to serve as an effective catalyst in reactions[18–21]. Yuan *et al*. recently reported that Cu-Si nanostructures also possess novel optical properties [9]. Wen *et al*. showed that Cu-Si nanostructures can be used as a catalyst to fabricate Si nanowires [22]. For its vast applications in diverse fields, it is clear that there is a need to revisit the growth studies for the $Cu_3Si$ islands in more details in order to understand how and why the nanostructures of different shapes form. The growth processes to account for $Cu_3Si$ nanostructure formation can be driven by energetics and/or kinetics considerations, and the study will of it need to investigate growth over a wide range of temperatures as well as for different Cu coverages. In particular, we will focus on how these growth factors influence the morphology of $Cu_3Si$ nanostructures on the Si(100), Si(111) substrates in terms of its geometry, structure, density and distribution for both types

of islands.

For the growth of $Cu_3Si$ nanostructures, we discuss the formation of epitaxial copper silicide islands due to shape transition for endotaxial systems on Si(111) and Si(100) substrates of p and n type dopants, which was not reported before. Time and temperature dependent growth kinetics of $Cu_3Si$ nanostructures were studied in detail in chapter 3. For the growth of islands on n-Si(111), equilateral triangles of various sizes have been found to grow up to a critical size, beyond which the shape transition is from equilateral triangular to trapezoid. For epitaxial islands on a p-Si(100) and p-Si(111) substrate, square islands have been found to grow up to critical size, beyond which the rectangular islands and long nanowires are formed. In chapter 4 we discuss HCI assisted growth of $Cu_3Si$ nanostructures on Si(111) and Si(100) substrates of p type dopants. Charge state (potential energy) and fluence dependent growth kinetics of $Cu_3Si$ nanostructures were studied in detail. These results will be discussed in chapter 5.

## 1.2 Goals and Objectives

The goal of this thesis is to study the growth process of self assembled Cu-Si nanostructures on Si substrates grown by ebeam deposition technique in UHV. From previous researcher's work, it is evident that the ebeam evaporation method in UHV would result in self assembled Cu-Si nanostructures on Si(100), Si(110), and Si(111). The first objective of this thesis is to demonstrate the growth process of defect assisted self assembled epitaxial Cu-Si nanostructures on Si(111) and Si(100) substrates. The fabrication procedure, kinetics and characterization techniques will be discussed in chapters 2 and 3. Based on Cu-Si phase diagram, that the Cu-Si nanostructures phase we observed was found to be $Cu_3Si$, and experimental studies such as XRD

and SEM-EDAX were used to confirm the phase. Surface morphologies of $Cu_3Si$ nanostructures were studied using SEM and EDAX analysis. Image analysis using Matlab was performed to acquire average densities and dimensions of nanostructures. Crystallographic orientations and phases were studied using XRD. Orientation of $Cu_3Si$ nanostructures on Si(001), Si(111) was also studied using SEM-EDAX.

The second objective was to nanopattern Cu-Si nanostructures on Si substrates and this will be discussed in Chapter 4. Nanopattering of self-assembled Cu-Si nanostructures on Si substrates is important for major applications in the semiconductor industry. Since, the growth of these silcides are found to be defect assisted, we have taken a completely new approach to create defect sites(voids) on the Si substrates using highly charged ion(HCI) beams of Ar. $Ar^{q+}$ (q=1,4,8) HCI beams of different charge states and varying fluences were used to create voids on the substrate. $Cu_3Si$ nanostructures were fabricated on HCI irradiated substrates using Ebeam technique in UHV. By this approach we were able to eliminate the over night annealing step which involves a high thermal budgets and consumes 10-18 hours. This approach also provides alternate method to understand the sputter yields of HCI irradiated materials. To the best of our knowledge, there is no research performed on HCI assisted nanopattering of $Cu_3Si$ nanostructures on Si substrates. Therefore this study is important since it involves low thermal budgets and eliminates photolithographic steps, for example.

It is also interesting to know what happens when a slow HCI beams interact with polycarbonate (PC, Lexan). PC is a promising polymeric material, characterized by excellent electronic, thermal, physical and optical properties. They have attracted much interest in variety of engineering applications such as optical lenses, solar cells and nuclear track detectors because of their light weight, durability, high optical transmittance, high deformation temperature, design flexibility and cost effectiveness

[23–25]. PC being hydrophobic, there has been increasing interest to make it more adhesive or convert it to hydrophilic by modifying its surface properties. In the third objective of this thesis, modification of surface properties of polycarbonate using HCI beams of argon and oxygen were investigated and are discussed in Chapter 5. $Ar^{8+}$ ,$O^{3+}$ and $O^{5+}$ beams of varying fluences were used for this study. X-ray photoelectron spectroscopy (XPS) measurements were performed on untreated and polycarbonate substrates irradiated with HCI beams of $Ar^{8+}$, $O^{3+}$ and $O^{5+}$ to study the structural and chemical modifications. Surface modification in terms of bond intensities of C-C, C-0 and C=0 were discussed in detail. Finally, Chapter 6 includes a summary and a discussion of future work.

# Key Issues

The key issues that will be addressed in this thesis are:

1. Identification of the underlying causes for the growth behavior of $Cu_3Si$ islands.
2. Determining if the growth and shape evolution of the islands are influenced by energetics and strain or limited by kinetics.
3. Nanopattering of $Cu_3Si$ islands on silicon substrates using highly charged ion beams and identification of their growth behavior and dynamics.
4. Lastly, surface modification of polycarbonate using highly charged ion beams.

Thin $Cu_3Si$ films in this thesis are grown epitaxially on $SiO_2$/Si(111) and $SiO_2$/Si(100) through RDE technique. The heteroepitaxially grown $Cu_3Si$ formed islands exhibited Volmer-Weber (VM) growth mode. To understand the growth kinetics of $Cu_3Si$ islands it is important to understand the epitaxial growth of thin films

on $SiO_2$/Si substrates. In the next section thin film growth kinetics will be discussed in detail.

## 1.3 Thin Film Growth

Thin film technology is a fast growing field and the number of applications increases every day. Ever since the size of the microelectronics devices and circuits miniaturize into the range of nanometers there has been increasing challenges to grow films of high quality in nano dimensions. In this section we describe the basic phenomena of thin film growth process and associated growth modes.

During the earliest stage of film formation, when a sufficient number of vapor atoms (flux, F) or molecules impinge on the substrate surface can undergo different surface processes as shown in Fig. 1.1. An approaching atom can either be reflected or adsorbed on to the surface of the substrate and the process is dependent on the incoming flux of atoms, sticking coefficient and the trapping probability. Close to the surface few atomic diameters from the substrate the atoms experiences weak vander Waals force and undergoes physisorption. Once an atom sticks to the surface, it creates a tension in the surface due to stretching of substrate atoms in response to the absorption of the atom. Atoms are not strongly bound to the substrate and undergo hopping or diffusion to find the heterogeneous nucleation sites that possess minimum surface energy such as stacking faults, steps, kinks, terraces, grain boundaries etc. to settle. Diffusion is generally considered to be random walk phenomena and increases with temperature, i.e, hopping probability is equal both forward and backwards. A newly approaching atom can either find a new location to settle or form a strong chemical bond with already existing atom by undergoing chemisorption. Both physisorpiton and chemisorption have to overcome local energy barriers and the rates

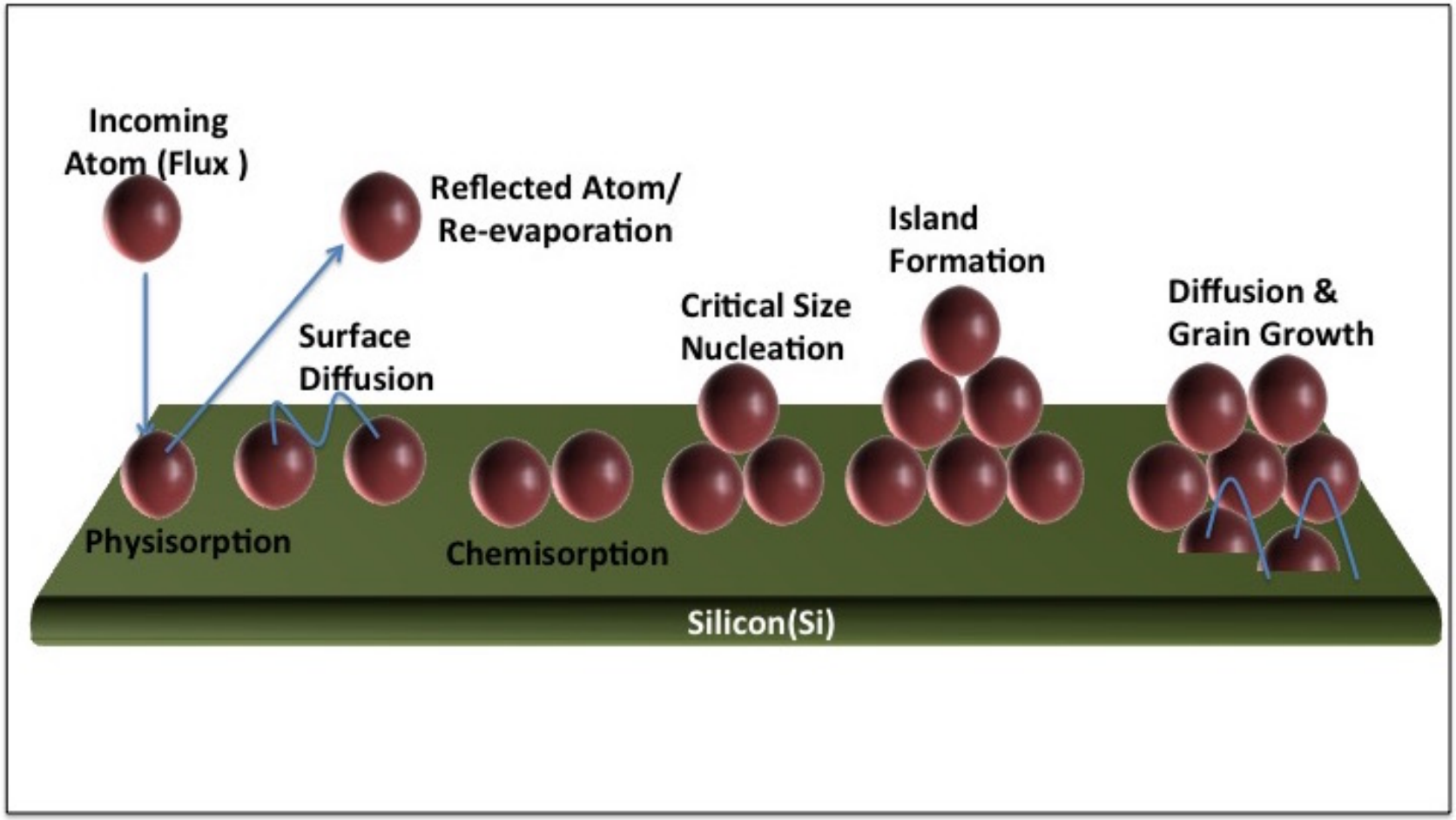


Figure 1.1: Schematic illustrations of the various kinetic processes on a substrate surface.

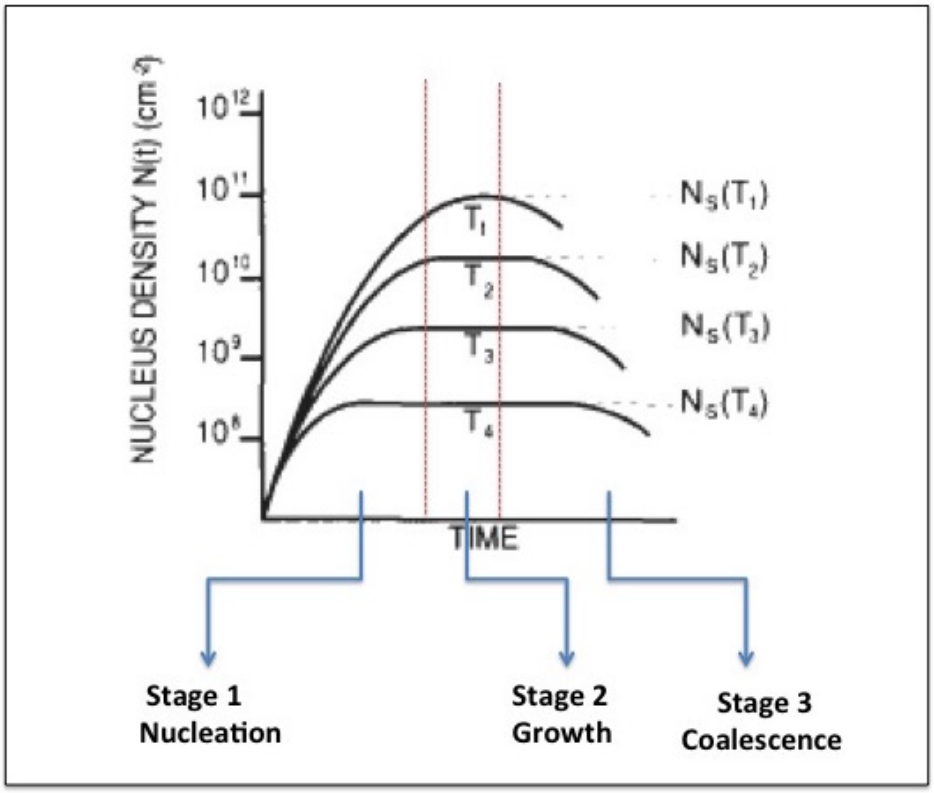


Figure 1.2: Dependence of N(t) with time and substrate temperature. Figure adapted from [26].

are thermally activated. The diffusion rates and activation energies can be determined from Arrhenius type plots. As the deposition continues a sufficient number of atoms nucleate on the surface to form a nuclei of critical size. The critical size required to form a stable nucleus is defined by various factors such as temperature, deposition rate, vapor deposition pressure, incoming flux etc. With time as the atoms arrive and stick to the existing nucleus, it increases in size and forms a stable island. There are three different types of island formation observed as shown in Fig. 1.3.

As the deposition proceeds, more islands begin to nucleate on the surface, thereby increasing the density of the islands. Stage 1 nucleation is considered to be at this point, when the rate of island nucleation is high. When a sufficient number

of island have nucleation on the surface, the probability of island nucleation begins to decrease as atoms are captured by existing islands. During this stage (stage 2: Growth stage), the islands will start to grow in size while the rate of nucleation of islands decreases. With further deposition, the rate of nucleation eventually reaches zero as all arriving atoms on the surface are captured by the islands. As deposition proceeds, the islands will grow larger until they 'touch' each other on the surface. During this stage (Stage 3: Coalescence stage), islands coalesce together to form even bigger islands resulting in a decrease in the number density of islands on the surface. With further deposition, the islands grow larger and finally coalesce to form a film. How the coalescence will occur depends on the mobility of atoms on the surface and the higher the mobility, the more the coalescence. Coalescence decreases the island density and growth continues to form a closed network of islands. With further deposition, the voids fill in completely and the film is said to be continuous.

The dependence of nucleus intensity (N(t)) on time and substrate temperature ($T_4 > T_3 > T_2 > T_1$) is shown in Fig. 1.2. The first region where the nucleus(island) density increases to maximum is known as nucleation stage. At the end of the nucleation stage, new island generation decreases and an onset of increase in the area of existing islands begins which is shown in region 2 marked as growth stage. With further deposition, coalescence of islands minimizes the island density and tends towards the formation of a uniform thin film which is shown as coalescence stage. These growth stages are also temperature dependent since the diffusion and activation energies are temperature dependent. It can also be inferred from Fig. 1.2 that as the temperature increases the density decreases and the area increases which signifies the growth mode to be diffusion limited. Growth of $Cu_3Si$ nanostructures in all these three stages are explored and will be discussed in detail in Chapter 3.

**Thin Film Growth Modes:**

The three distinct island growth modes are defined based on the balance between the surface free energies of substrate ($\gamma_s$), film ($\gamma_f$) and the interface ($\gamma_i$) between substrate and the film.

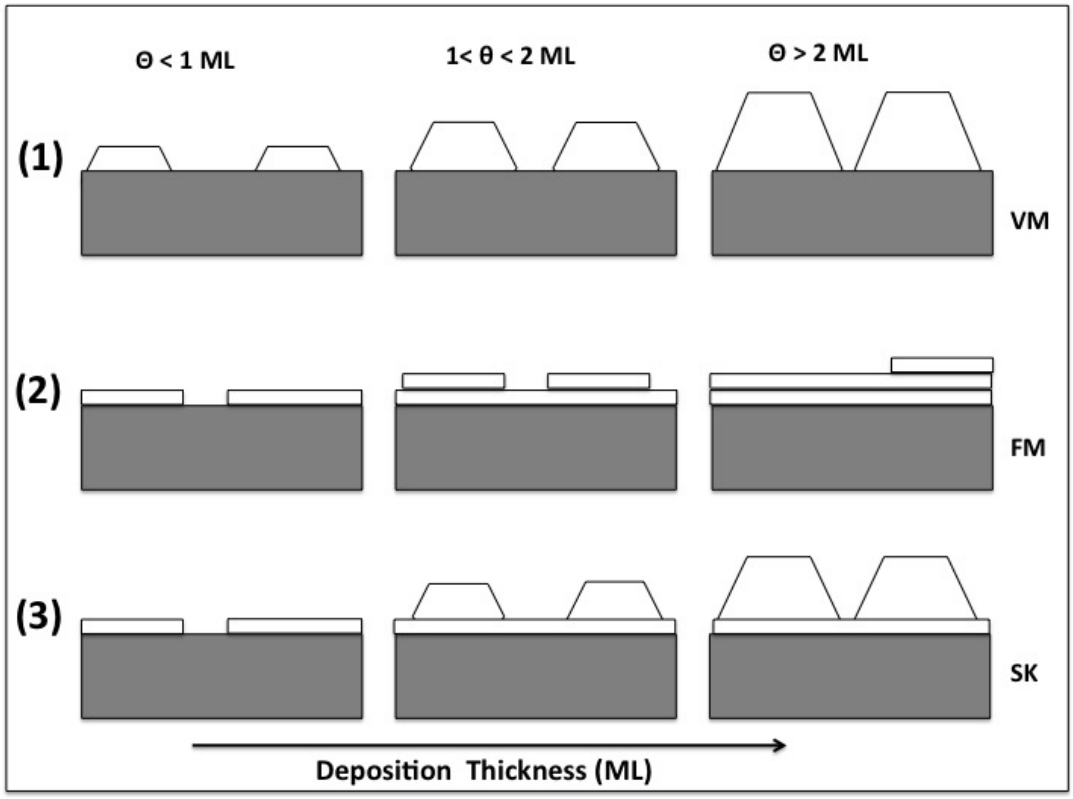


Figure 1.3: Basic modes of thin film growth with (1) Volmer-Weber, (2)Frank-van der Merwe(FM), and (3) Stranski-Krastanov growth.

The fundamental growth modes of thin film can be distinguished from the equation [1.1]

$$\gamma_s = \gamma_f + \gamma_i cos\theta \tag{1.1}$$

Where $\gamma_s$, $\gamma_f$ and $\gamma_i$ are surface energy per unit area of substrate, film and interface and $\theta$ is the contact angle between the film and interface.

- when $0 < \cos\theta < 1$ ; $\gamma_s < \gamma_f + \gamma_i$
- when $\theta = 0$; $\gamma_s = \gamma_f + \gamma_i$
- When $\cos\theta \leq 1$ ; $\gamma_s \geq \gamma_f + \gamma_i$

These thin film growth mechanisms have been named after their authors. The experimentally observed three fundamental thin film growth modes are described in this section.

1. Volmer-Weber (VM):

Clusters of atoms nucleate on the substrate and grow in three dimensions to form islands. This happens when the deposited atoms or molecules are stronger bonded to each other than to the substrate[27]. As the deposition time or thickness increases the islands grow bigger as shown in Fig. 1.3(1).

From Eq.1.1, For island growth $\theta > 0$, and therefore $\gamma_s < \gamma_f + \gamma_i$

e.g: Au/NaCl, As/NaCl , $Cu_3Si$/Si(111) , metals on insulators, graphite, mica etc.

2. Framk-van der Merwe (FM):

The growth mode is opposite to that of VM. Here, the smallest stable nucleus grow in two dimensions resulting in the formation of planar sheets. This growth mode involves filling up one atomic layer before the next layer starts to form.Film atoms are more strongly bound to substrate than to each other[28]. With deposition time or thickness layers start piling on each other as shown in Fig 1.3(2).

From Eq.1.1, For layer growth $\theta = 0$, and therefore $\gamma_s = \gamma_f + \gamma_i$

e.g: GaAs/GaAs, AlAs/GaAs , single crystal epitaxial growth etc.

3. Stranski-Krastanov growth (SK):

This is a combination of layer and island growth, which starts with the formation of a few layers and continues with island formation. With the increase in the

deposition time beyond critical layer thickness the growth mode shift from 2d layer to 3d island, which depends on lattice mismatch, strain energy relaxation and chemical potential of the deposited film [29]. The growth with deposition thickness is shown in Fig 1.3(3).

From Eq.1.1, For SK growth $\gamma_s \geq \gamma_f + \gamma_i$

e.g: Ag/Si(111), metal-metal systems, metal-semiconductor systems.

### 1.3.1 Thin Film Deposition Techniques

Methods used to deposit thin films are generally split into two categories. physical vapor deposition (PVD) and chemical deposition processes [30].

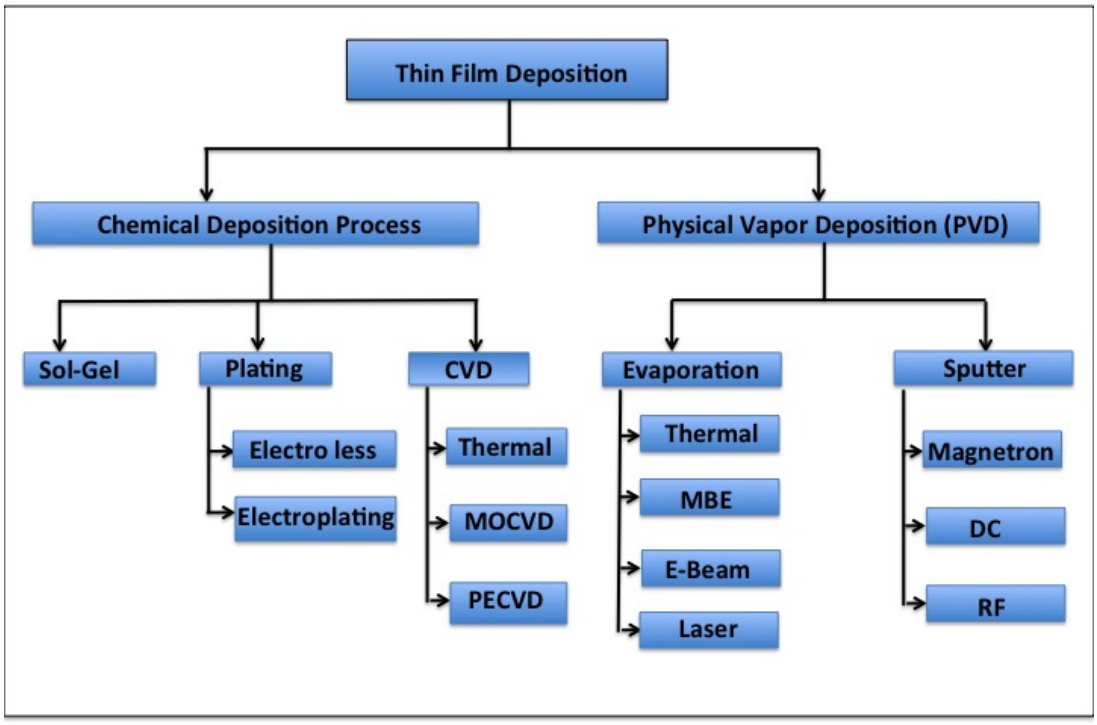


Figure 1.4: Schematic representation of thin film deposition techniques.

In PVD processes, a source of pure material(target) to be deposited is vapor-

ized and transported in the form of vapor through a vacuum or low gas environment to the substrate where it condenses. The target material is evaporated following different techniques depending on its melting point, conductivity and nature. Some of the familiar methods involve thermal, ebeam , and laser heating. In certain cases, a subsequent high temperature annealing step might be required to crystallize the films. In the final step the film is analyzed to evaluate the process.

The PVD process is divided into two major categories: Sputtering and thermal evaporation[30] as shown in Fig. 1.4.

Sputter deposition, commonly called sputtering, is when a solid surface is bombarded with energetic particles such as accelerated ions, removes atoms/molecules from a solid target's surface, projecting them into the gas phase from which they condense on another surface (substrate). Since sputtering produces a vapor of electrode material, it is also used as a method of film deposition similar to evaporation deposition. Several sputtering systems are being used for thin film deposition including dc diode, rf diode, magnetron, reactive ion beam deposition, ion assisted deposition and ion beam sputtering[31, 32].

Thermal evaporation deals with the evaporation of the source materials in a vacuum chamber through the use of resistive element heating. Typically the bulk material is placed into a source (evaporation boat, basket, or filament-heated crucible), and as power is applied, the temperature rises to facilitate evaporation. The next step involves transport of evaporated vapor from the source to the substrate followed by the condensation of vapor on to substrate surface to form a solid film. This process is conventionally called thermal evaporation. In the final step the film is analyzed to evaluate the process. Achieving precise control over temperature can be difficult and some evaporants have a tendency to alloy with the source material. Additional complications include requirements for high vacuum, difficulty to achieve

high temperatures for evaporating targets with resistive heating and the need for the process monitoring and control [31, 33].

Because of the mentioned challenges this technique is not quite as universal as others. Besides regular thermal evaporation, ebeam evaporation and molecular beam epitaxy (MBE) are the most reliable deposition processes for growing epitaxial films in a high vacuum[34]. Electron beam evaporation sources include components that evaporate the base material through the use of a high energy electron beam, generating very high deposition rates. A Magnetic field is used to focus the electron beam on to the target material, and bombardment of the electrons generates enough heat to evaporate a wide range of materials with very high melting points. This process is performed in UHV and can achieve precise control over deposition flux and deposition rates. Electron beam evaporation (ebeam) is considered to be one of the most efficient thermal process to achieve controlled deposition of alloys and compounds in the range of monolayer (ML) thickness and we have also used the same technique to deposit copper silicides on silicon. The ebeam technique will be described in detail in chapter 3.

Methods of film formation by purely chemical processes in the gas or vapor phases include chemical vapor deposition (CVD), plating and sol gel. CVD is a materials synthesis process whereby constituents of the vapor phase react chemically near or on a substrate surface to form a solid product. Fundamental principles of CVD encompass an interdisciplinary range of gas-phase reaction chemistry, thermodynamics, kinetics, transport mechanisms, film growth phenomena, and reactor engineering. The main feature of CVD is its versatility for synthesizing both simple and complex compounds with relative ease at generally low temperatures. Both chemical composition and physical structure can be tailored by control of the reaction chemistry and deposition conditions. When a plasma beam is used to enhance or assist the the

chemical vapor deposition reaction, the process is usually denoted as plasma enhanced chemical vapor deposition (PECVD) [34, 35].

### 1.3.2 Types of Films

Epitaxial film growth has been classified into two categories based on the crystal strucuture of the film and the substrate.

1. Epitaxial :

Epitaxy is defined as the growth of a single-crystalline layer on a single crystalline substrate, randomly oriented polycrystalline or amorphous substrate and depends critically on the interaction strength between adatoms and the surface. Homoepitaxy or heteroepitaxy are said to occur if epitaxial film growth takes place on a similar or a different substrate, respectively. Epitaxial film growth will be discussed in the next section in detail. For example, silicon on silicon is one of the most commonly grown epitaxial film.

2. Polycrystalline:

It is the randomly oriented growth of a crystalline, polycrystalline or amorphous substrate. In general, deposition at lower temperatures and high gas concentration leads to polycrystalline growth. Due to the high concentration of atoms, many nuclei of different orientations are formed. Upon coalescence, a film consisting of many randomly oriented grains will be formed. During the film growth, favorable grains grow at the expense of less favorable ones. This results in finer-grained films. Most elemental metals like Cu, Al etc. grown at room temperature are polycrystalline in nature.

3. Amorphous:

Amorphous means that crystallization is completely absent but some short range atomic ordering could be present. Unlike crystallinity, amorphicity is obtained in general at low temperature and high supersaturations. Under these conditions a very high number of nuclei whose mobility is very low arises on the substrate surface. These nuclei are randomly oriented and upon coalescence a film consisting of unoriented or randomly oriented grains is obtained. For example, amorphous $SiO_2$ film is grown by thermal oxidation of silicon in oxygen ambiance.

All films in this thesis are epitaxially grown on non lattice matched seed layers (film) and substrates. In this thesis we will discuss heteroepitaxially grown metal silicide (copper silicides) on Si(100) and Si(111) substrates in chapters 3 and 4. Nanowires are the predominant and stable shape observed in most of the metal/semiconductor heteroepitaxial systems. Copper silicides nanostructures grown on silicon substrates did show similar behavior and exhibited the nanowire as its stable shape. In the next section epitaxial thin film growth mechanism will be discussed in detail.

### 1.3.3 Epitaxy

In recent years there has been a lot of research devoted to both the basic science of epitaxy and its engineering applications. In this section the basic science of epitaxy and its classifications will be discussed. Two ancient Greek words, epi (placed or resting upon) and taxis (arrangement) are the root of the modern word epitaxy. Epitaxy is the most important phenomenon in semiconductor thin-film device technology. Epitaxial thin film growth means that the film which is grown is influenced by the structurally-ordered fashion of the material that it is deposited on. Epitaxy

arises when the system lowers its interfacial energy to align the lattice of the film with that of the substrate. Epitaxial layer is generally free of defects, is purer than the substrate and can be doped independently of it.

An important quantity which characterizes epitaxy is the lattice misfit $f$, which is defined as

$$f = \frac{a_0(s) - a_0(f)}{a_0(f)} \tag{1.2}$$

where $a_0(f)$ and $a_0(s)$ refer to the unstrained lattice parameters of film and substrate respectively. Positive $f$ implies that the initial layers of the epitaxial film will be stretched in tension while the substrate is compressed. Negative $f$ means film compression and an extended substrate. For example, the $\eta$ phase of $Cu_3Si$ has lattice parameters of a = 4.06 Åand c = 7.33 Å, where as Si ((111) and (100)) condenses in the diamond structure with a cubic lattice constant of a = 3.84 Å. The misfit along 'a' direction for 2-D lattice Si and $\eta-$ $Cu_3Si$ is -5.4% and misfit along 'c' direction is -47.6%. Negative misfit means the film undergoes compression and the substrate extends.

There are two types of epitaxy.

1. Homoepitaxy: where the film and the substrate are of the same material. There will be no strain between the film and the substrate because their lattice parameters are perfectly matched. Lattice misfit $(f)$ is 0 for homoepitxay films. Epitaxially grown layers are purer than the substrate and can be doped independently of it. e.g: Si deposited on Si wafers is the most significant example of homoepitaxy.

2. Heteroepitaxy: where the film and substrate are composed of different materials like in this thesis. If the lattice mismatch is very small, then the heteroepitaxial structure is essentially like that of homoepitaxy. In most of the cases of heteroepitaxy

the lattices are not matched where $f$ is not zero. Hence, the deposited film can either be strained to match the substrate coherently or relaxed by introducing dislocations where possible in a semi or incoherent manner. Metal/semiconductor interconnects, optoelectronic devices such as LEDs and lasers utilizing compound semiconductors, are based on heteroepitaxial film structuruces. e.g: AlAs deposited on GaAs, NiSi on Si and Cu on Si.

The heteroepitaxially grown $Cu_3Si$ films in this thesis on $SiO_2$/Si substrates exhibited nanowire as stable shape. This stable nanowire shape is attributed to the strain induced shape transition mechanism proposed by Tromp. In order to understand the growth kinetics of $Cu_3Si$ naonowires, it is important to understand the growth mechanism of metal silicide nanowires. The metal silicde nanowire growth mechanism is explained in detail in the next section.

### 1.3.4 Metal Silicide Nanowires

Generally metal silicides are used as contacts on gate, source and drain in CMOS logic and memory devices as shown in Fig. 1.5. The most important benefit of using copper in integrated circuits is that copper offers lower resistivity than $CoSi_2$ and NiSi, which historically has been the dominant contact material. Using a lower resistivity contact material like copper decreases the contact resistance, which, in turn, increases the transistor speed.

Growth of metal silicide nanostructures can be summarized into four categories as shown in Fig. 1.6. In general, epitaxial layer can be grown when the lattice constant of the epilayer matches that of the substrate on which it is grown.

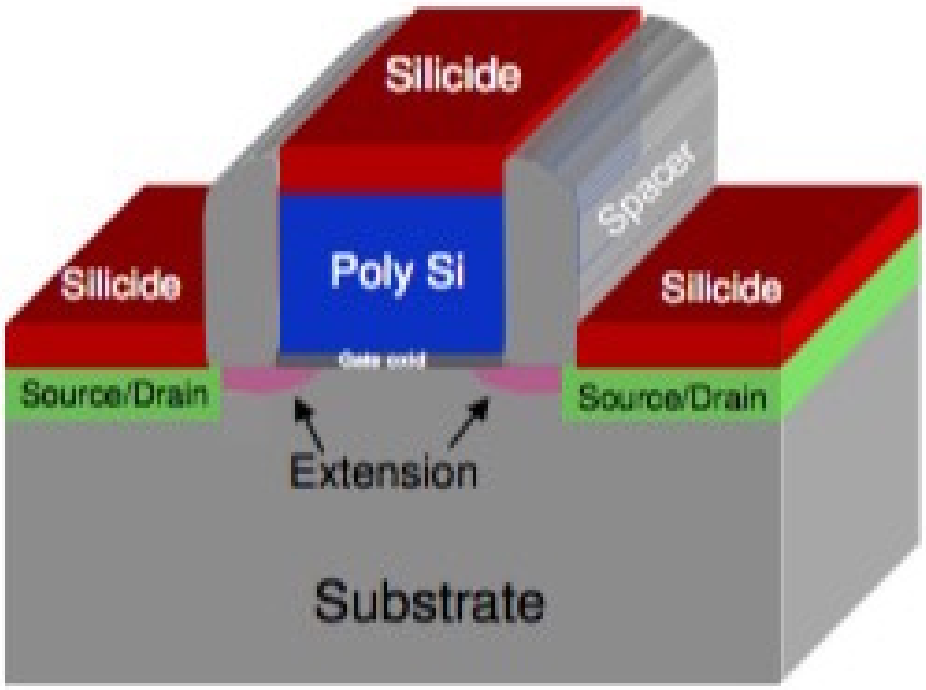


Figure 1.5: A simplified schematic of CMOS transistor.

1. Generation of dislocations:

For a system with symmetric lattice mismatch i.e, Ge on Si(001) and InAs on GaAs(001), the strain energy in the deposited film can be relaxed by the creation of islands or dots at the substrate/film interface[36–38]. This type of growth mode generally results in VM growth.

2. Anisotropy Lattice Mismatch:

Rare-earth metals like Sm, Dy, Er, Pt, Gd were deposited on heated Si(100) substrate to form self assembled metal disilicide nanowires utilizing anisotropic lattice mismatch. The shape is believed to be because of small anisotropic lattice mismatch ($\sim 0\%$) in the larger direction (longitudinal) and larger mismatch ($>3\%$) in the narrow (axial) direction as a result of anisotropic strain. In order to achieve the lowest strain energy with regards to substrate, silicides adjust their shape into nanostructures. The lattice mismatch will limit the lateral growth. Shape and aspect ratios of nanowires grown by this method were strongly influenced by their asymmetric lattice mismatches with respect to substrate lattice [16, 39–47].

3. Strain Induced Shape Transition:

Another major mechanism that has been widely recognized in recent years which that constitutes strain relief, rely on the shape transition such as island formation to relieve the stress generated during the silicide growth. As in agreement with the Tersoff, Tromp and Jesson *et al*. "strain-driven shape transition"[48, 49] model, below a critical size, islands have a compact symmetric shape. For larger sizes, they adopt a long thin wire shape, which allows better relaxation of the island's stress. Systems like $Au_4Si$/Si(111), $CoSi_2$/Si(100) and Ti/ Si(111) exhibit the elongated island growth [4–6, 50].

4. Endotaxy:

He *et al.* have described an endotaxial growth mechanism that applies to a range of transition metals on Si(100), Si(110) and Si(111). Endotaxy involves epitaxial growth into the substrate (Type B) without anisotropic lattice mismatch. A twinning relationship between the substrate and silicide breaks the symmetry of the surface and leads to asymmetric growth of islands. A variety of metal silicides like $CoSi_2$, $TiSi_2$, $FeSi_2$ on Si(100) were grown by this method. The nanowires grown by this method are long, narrow with high aspect ratio[7, 14, 51]. Endotaxy growth involves lattice constraints on multiple, non parallel interfaces whereas anisotropic lattice mismatch method involves lattice constraints only on a single interface parallel to surface. Endotaxy growth is possible for both Type A and Type B interfaces[7, 14, 51].

### 1.3.5 Stress development in Metal/Si systems

Stresses in thin films can cause failure of the films through cracking or buckling. Stress affect the physical properties of the films and can, for example, be used to tailor the band structure of films and also to modify the magnetic anisotropy of the film. One of the most common causes of the stress in thin films is a difference in the thermal expansion between film and substrate. Upon annealing of a metal/Si system, the film inevitably undergoes certain volume changes, inherent to the annealing process. As the film is attached to the substrate, it cannot fully undergo its desired volume change: the film/substrate system curves and stress builds up in the film. It is usual to divide the observed stresses into two categories: intrinsic and extrinsic.

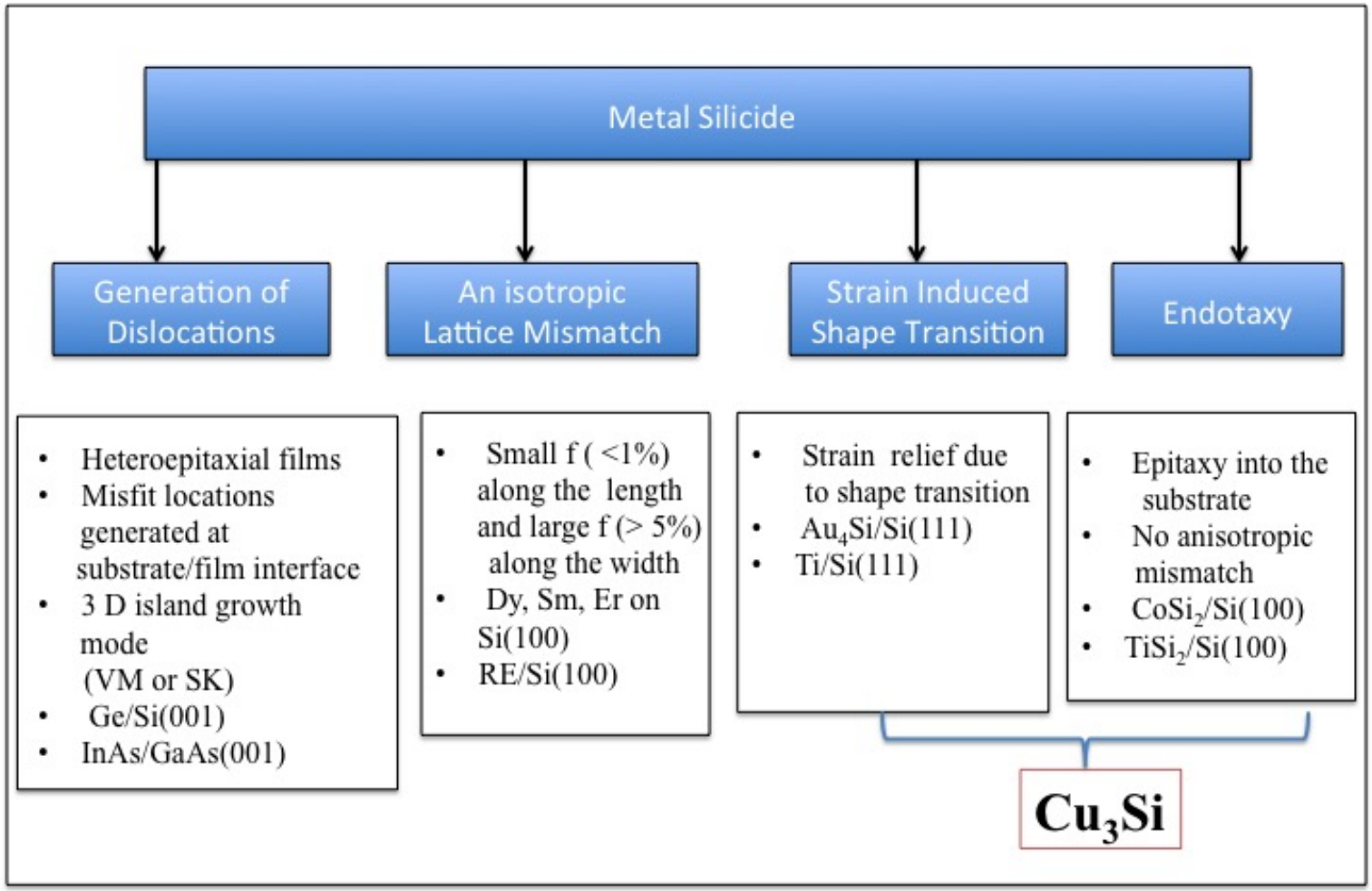


Figure 1.6: Classification of Metal Silicide growth modes

**Extrinsic:**

Thermal stress is an example of extrinsic stress, and is often a larger contributer to the total film stress. The film and substrate are both characterized by a particular linear thermal expansion coefficient. Upon thermal treatment, the film and substrate necessarily undergo a specific material related expansion. However, as the film and substrate are laterally attached to one another, they are therefore restricted from fully thermally expanding/contracting. If $\alpha_f$ and $\alpha_s$ represent the linear thermal expansion coefficient of film and substrate, an incremental change in temperature from $T_0$ to $T$ ($\Delta T$) will result in thermal stress in film and substrate.

$$Strain = \Delta\alpha\Delta T \tag{1.3}$$

Hooke's law can be used to calculate the corresponding stress where Y represent Young's modulus.

$$Stress = Y\Delta\alpha\Delta T \tag{1.4}$$

**Intrinsic:**

Intrinsic stresses are defined to be those stresses which arise during the deposition or growth, which are not due to thermal expansion mismatches. Internal stress are generally irreversible, in contrast to thermal-expansion mismatch stresses that can be reversed by simply changing the temperature. Among the mechanisms that can introduce intrinsic stresses are coalescence of grain boundaries, lattice misfit stress, annihilation of excess vacancies, introduction of defects and dopants, oxidation and reaction at metal/oxide interface. Internal stress due to lattice misfit is given by

$$f = \frac{a_0(s) - a_0(f)}{a_0(f)} \tag{1.5}$$

where $a_0(f)$ and $a_0(s)$ refer to the unstrained lattice parameters of film and substrate respectively. Total stress is given by

$$Stress = Y\Delta\alpha\Delta T + \frac{a_0(s) - a_0(f)}{a_0(f)} \tag{1.6}$$

# Chapter 2

# Experimental Techniques

## 2.1 Introduction

This chapter provides an overview of various experimental tools used for the present study. The main experimental techniques utilized for investigating the growth of $Cu_3Si$ nanostructures on $SiO_2$/Si(111) and $SiO_2$/Si(100) substrates are scanning electron microscope (SEM-EDAX), X-ray diffraction (XRD) and ellipsometer. X-ray photoelectron spectroscopy (XPS) was used to study the structural and chemical modifications of pristine and HCI irradiated polycarbonate.

## 2.2 Scanning Electron Microscope (SEM)

Scanning electron microscopy (SEM) is essentially a high magnification microscope, which is widely used technique to investigate the morphology of the prepared samples. SEM in this thesis is a high resolution S4800 and variable pressure S3400 Hitachi model, which is located at the Electron Microscope Laboratory, Clemson University, Clemson.

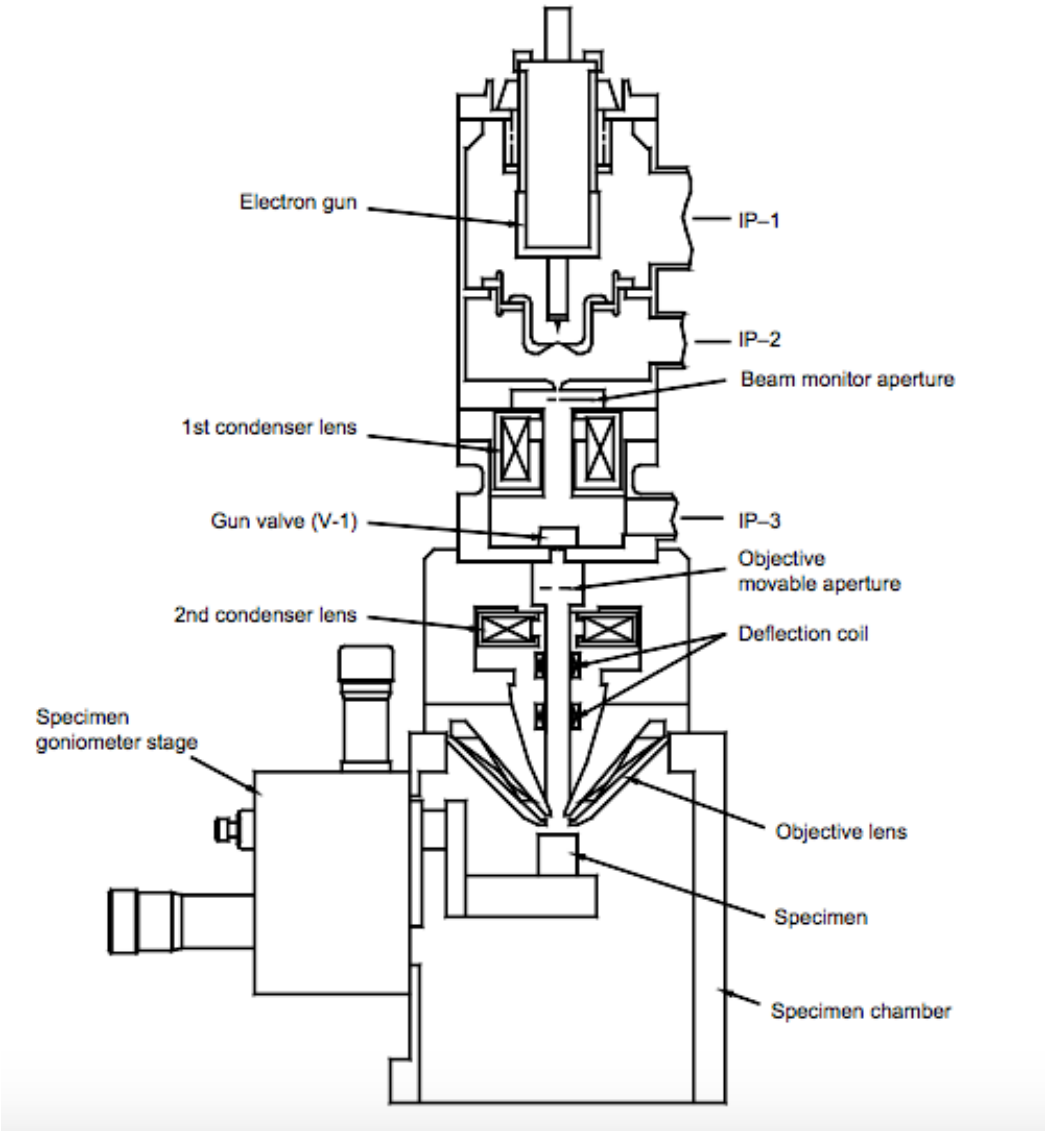


Figure 2.1: Sectional view of the Hitachi S-4800 SEM. Adapted from [52].

A simplified schematic of an SEM (Hitachi S4800) is shown in Fig. 2.1, which is comprised of an electron gun, a condenser, an aperture, an X-Y coil, an objective lens, and a detector. An electron beam is generated through thermionic or field emission. The generated electron beam is attracted towards the anode and is condensed by a condenser lens system. By using an objective lens system, the condensed electron beam is focused to a very fine point on the sample. The primary electrons of the electron beam strike the specimen surface and exhibit inelastic scattering by the atoms in the sample. The scattered electrons are collected by a secondary or backscatter detector and converted to a voltage and amplified. The amplified voltage is applied to the CRT grid and forms a clear image of the sample. The quality of the image depends on the electron beams voltage and current. Typical SEM images of islands formed by deposition of Cu on $SiO_2$/Si substrates in the temperature range 550-600°C is shown in Fig. 2.2.

A variable pressure scanning electron microscope (Hitachi S3400) was used to image HCI irradiated polycarbonate samples. Generally insulating samples like polycarbonate need to coated with conducting layer in order to image using SEM. The S3400 model SEM is capable of imaging dielectric samples without coating a conducting layer and has the capability to magnify image up to 300X.

### 2.2.1 Operating Procedure

The general operating procedure used with the two SEM systems for all measurements is outlined here.

- Specimen preparation: Specimens should be mounted on the sample holder using either double-sided sticky tape. Samples may be blown free of dust and debris using a nitrogen spray gun. Adjust the specimen height using the speci-

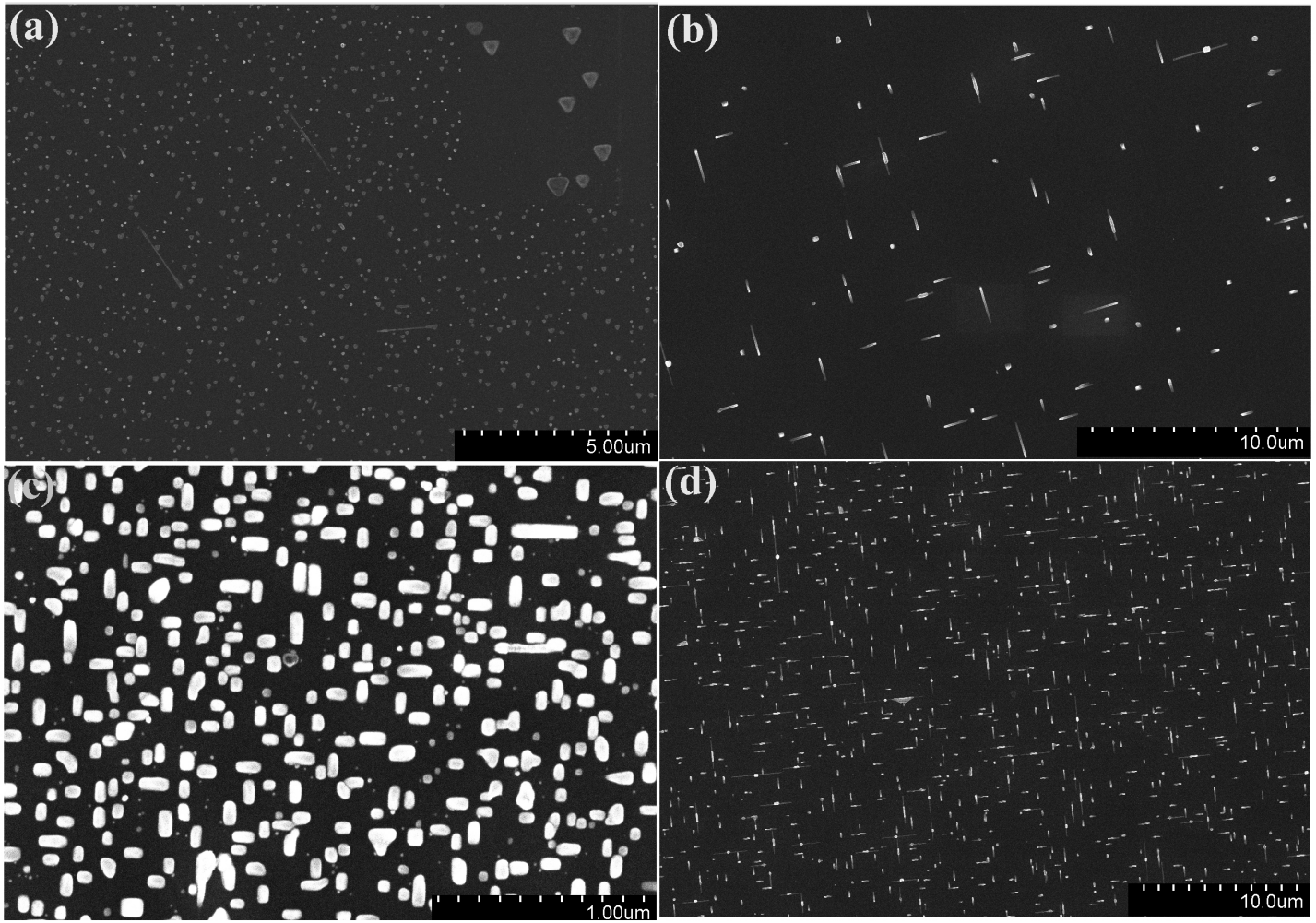


Figure 2.2: SEM images of $Cu_3Si$ islands formed by deposition of Cu on $SiO_2$/Si at constant deposition time (5 mins). (a) n-type Si(111) at 600°C (zoomed image shown in inset), (b) p-type Si(111) at 600°C, (C) p-type Si(100) at 550°C, (d)p-type Si(100) at 600°C.

men height gauge.

- Loading a sample: Load the sample into the SEM console using load lock. Turn on the vacuum pump and wait until vacuum (5 x $10^{-6}$ Torr) is achieved. Move the sample to exchange position.

- Apply SEM high voltage: Turn on high voltage. Monitor the emission current. The Hitachi recommended emission current for normal SEM operation is 10 uA.

- Imaging mode: Choose secondary electron detector. Minimize astigmatism error before acquiring images. Adjust brightness and contrast. At the end save the images.

- Unloading sample: When finished imaging, turn off the high voltage. Move the sample stage to the exchange position. Vent the load lock and unload the sample.

### 2.2.2 Material Composition with energy dispersive X-ray spectrometer (EDAX)

The interaction of high energy electrons with the specimen also produces X-rays and these X-rays are detected by the SEM equipped with energy dispersive X-ray spectrometer (EDS) and wavelength dispersive X-ray spectrometer (WDS), which allows elemental analysis. During an inelastic scattering, an electron strikes an atom, the atom ejects an electron originally positioned in an inner shell (K shell). To return the atom to its lowest energy state, this 'vacancy' is immediately filled by an electron moving down from a higher-energy shell in the atom. In doing so, this high-energy electron must release some of its energy in the form of X-ray energy. As

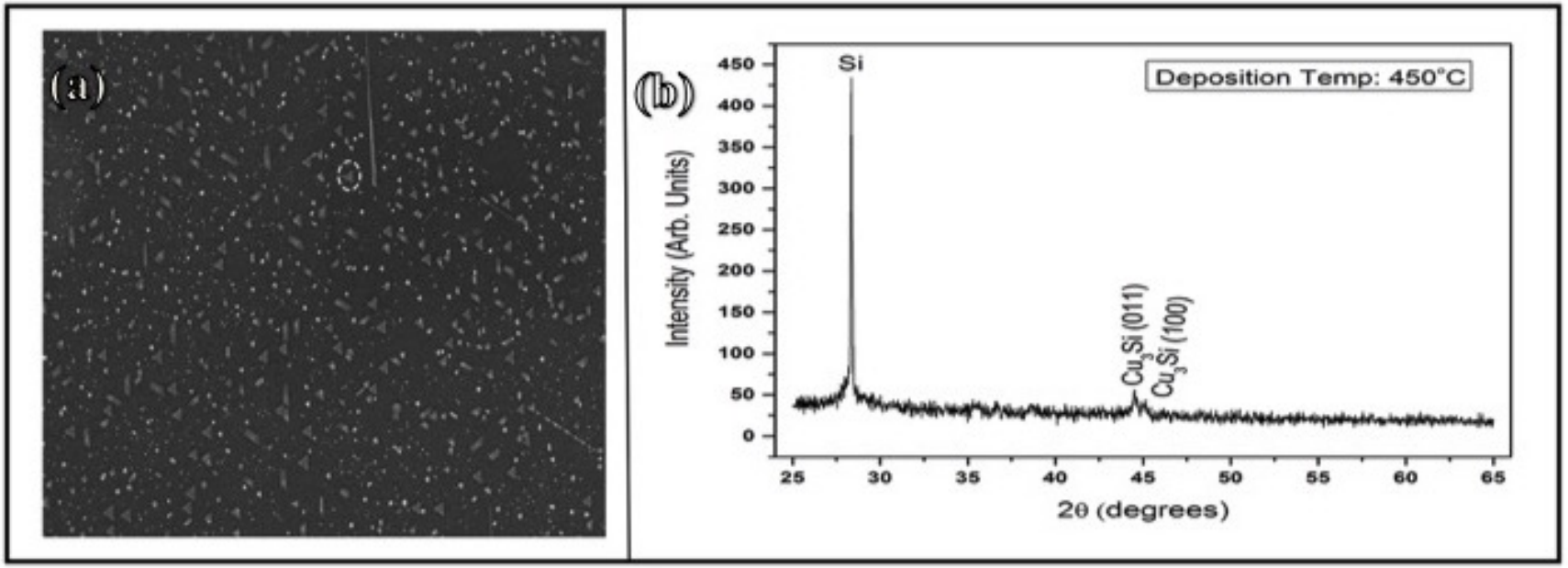


Figure 2.3: (a) SEM image of Cu deposited on $SiO_2$/Si(111) at 450°C. (b) XRD pattern of $Cu_3Si$ islands grown on $SiO_2$/Si(111) at 450°C.

a consequence, the energy released (expressed in eV) is exactly equal to the energy difference between the two energy levels. Since each atom has its own distinctive energy emission, identification of an unknown material is possible. A typical SEM image of $Cu_3Si$ nanostructures grown on $SiO_2$/Si(111) at 450°C is shown in Fig. 2.3(a). X-ray analysis revealed the growth phase to be $Cu_3Si$ shown in Fig. 2.3(b).

## 2.3 Xray Diffraction (XRD)

XRD is an analytical technique, where a single crystal is bombarded with X-rays to produce diffraction patterns which are recorded and analyzed systematically to study the nature of the crystal. X-ray diffraction analysis for the present work was performed on a Rigaku diffractometer operated at 40 KV located in the Clemson University chemistry department.

Two primary types of XRD analysis techniques are X-ray powder diffraction and single-crystal XRD. The underlying principles of the experiment are the same in both powder diffraction and single crystal diffraction.

When two parallel monochromatic X-ray beams of wavelength $\lambda$ incident on successive planes of a crystal at an angle $\theta$, constructive interference of the reflected beams from two successive planes occurs only when the path difference between the two diffracted beams fulfills the Bragg condition; $2d\sin\theta = n\lambda$, where $n$ is an integer, $\lambda$ is the wave length of the X-ray beam and $d$ is the distance between the planes[53]. As X-rays have a wavelength of the same order of magnitude as the lattice constants of crystals, the positions of the diffraction peaks and their intensities can be used to find out the structure, phase, etc., of a sample.

There are two types of commonly used X-ray diffraction techniques.

- Single Crystal X-ray Diffraction: It is used most commonly for determination

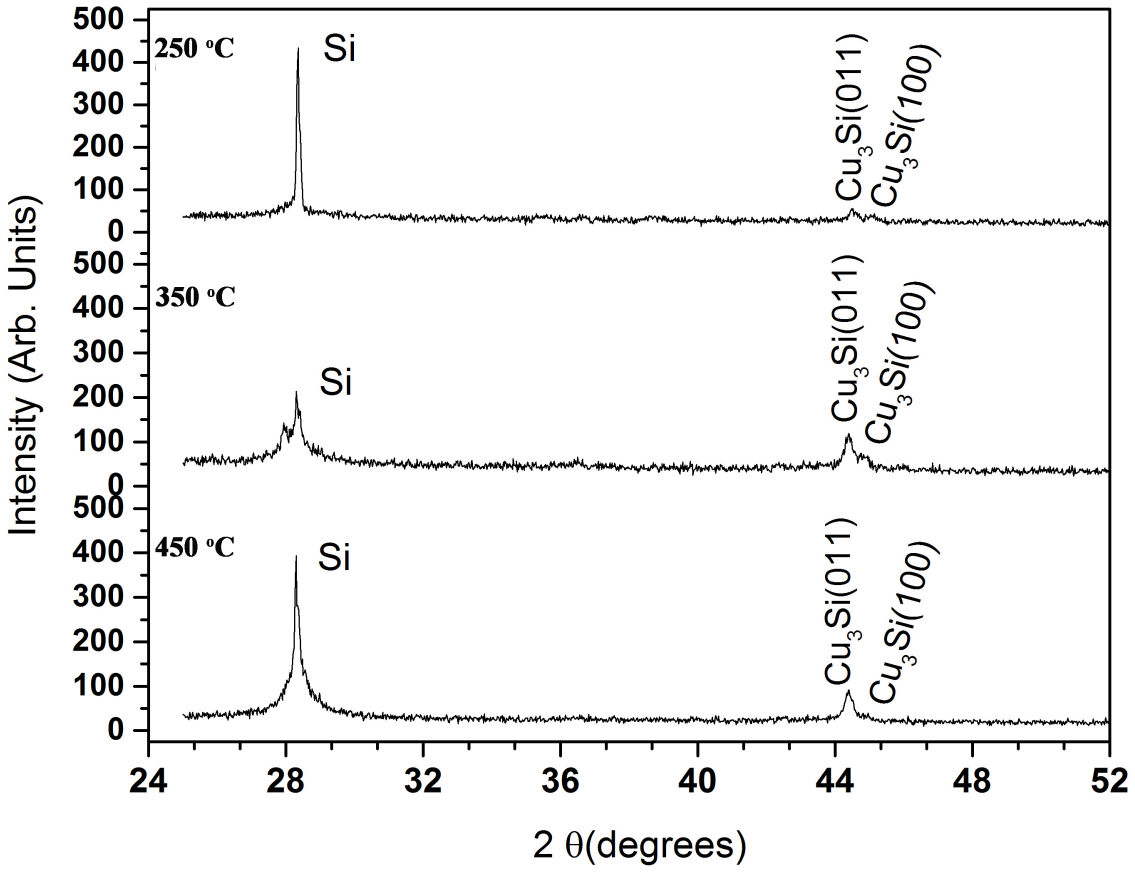


Figure 2.4: X-ray powder diffraction patterns of $Cu_3Si$ nanostructures grown on $SiO_2$/Si(111) in the temperature range from 250- 450°C. Peaks in the $Cu_3Si$ diffraction pattern are labeled with Miller indices, (h k l) indicating the set of lattice planes responsible for that diffraction peak.

of unit cell dimensions and the position of atoms within a crystal lattice. It is a popular technique, which does not require sample preparation (more than a clean surface), is non-destructive, and without need for lengthy evaluations.

- X-ray Powder Diffraction : It is far more common. The samples for powder diffraction may be large crystals, or they may be in the form of a powder composed of microcrystals that are too small to be seen by the human eye. For the present study powder diffraction studies were performed on $Cu_3Si$ samples as shown in Fig. 2.4.

Powder diffraction patterns are typically plotted as the intensity of the diffracted X-rays vs the angle $2\theta$. Peaks will appear in the diffraction pattern at $2\theta$ values when constructive interference is at a maximum, that is, when Bragg's Law is satisfied. By measuring the $2\theta$ values for each diffraction peak, we can calculate the $d$-spacing (the distance between the diffracting planes) for each diffraction peak.

Fig. 2.4 shows typical XRD spectra of Cu deposited on $SiO_2$/Si samples at temperature $> 250°$C. The Cu atoms in Cu/$SiO_2$/Si system interact with the Si atoms at the interface and form $Cu_3Si$ phase when the deposition temperature is above 250°C. As the spectra show, as the deposition temperature is increased to 450°C, three peaks at 28°, 44.6° and at 45.2° are visible. The peak at 28° corresponds to Si(111) and $Cu_3Si$ phase exhibiting diffraction peaks at 44.6° and at 45.2°, is the main phase present on the surface, based on the XRD pattern. The peak identities are confirmed from XRD database.

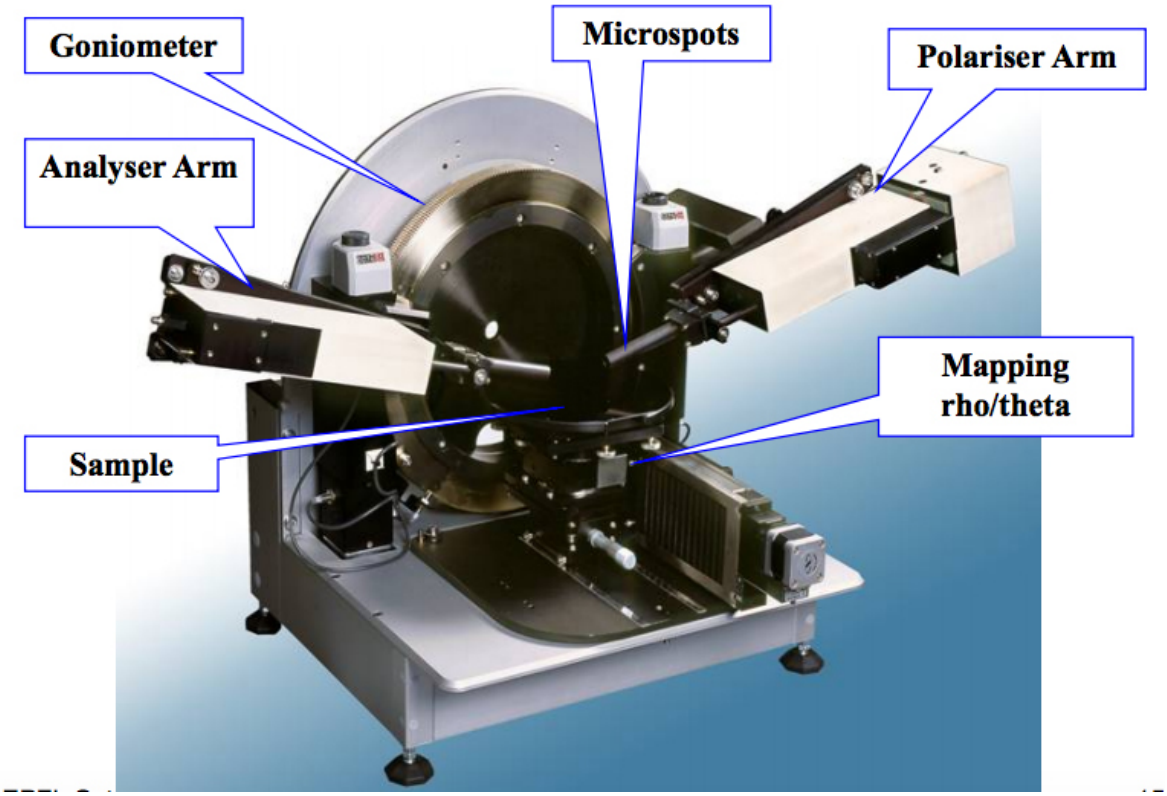


Figure 2.5: SOPRA GES5 Spectroscopic Ellipsometer. Figure adapted from [54].

## 2.4 Ellipsometer

It is a non-contact, non-destructive optical technique that detects the change in the thin film parameters. It is generally used to measure the thickness of films precisely up to few angstroms. Ellipsometry is a method based on measurement of the change of the polarization by analyzing light reflected (or transmitted) from the sample, both in amplitude and phase after non normal incidence on the surface to study. Ellipsometer measurements for the present work were performed on a SOPRA GES5 Spectroscopic Ellipsometer, which is located in the Clemson University Biomolecular Interactions Lab. In the present work the substrates are ultra thin oxide layers grown on silicon substrates ($SiO_2$/Si ) with both p and n type dopants.

An ellipsometer measures the changes in the polarization state of incident

light when it is reflected from a sample to deduce film on overlayer thickness[55]. One measures the amplitude ratio $tan\psi$ and the phase difference $\delta$ between p and s polarized light waves, and if a sample undergoes a change, for e.g, a thin film on the substrate changes its thickness, these reflection properties will change.

The SOPRA GES5 spectroscopic ellipsometer consists of a goniometer, an analyser arm, microspots, a polariser arm and sample and mapping stages as shown in Fig. 2.4.

- Goniometer: Used to automatically set the measurement angle (from 10° to 90°) to the optimum angle of measurement.

- Microspots: Allows the light beam to be focused on a very small area of the sample. A spot down to 50 $\mu m$ can be achieved for specific applications. Also used when measuring thin transparent substrates as it enables physical extraction from the measurement of the parasitic light coming from backside reflection of the substrate.

- Mapping stage: Allows automatic cartography measurements on several types of substrates of variable dimensions.

- Polariser and Analyser arms: These both consist of quartz Rochon prisms ($M_gF2$ for 190nm transparency) mounted on hollow axis stepper motors.

A schematic of the samples used for the present study is shown in Fig. 2.6. An ultra thin thermal oxide of 1.5 nm was grown on 3 inch diameter Si(111) and Si(100) substrates with p and n-type dopants. Oxide thickness measurements were performed at five different locations on each wafer (center and 4 corners) utilizing the ellipsometer. The average thickness was found to be approximately 1.5 $\pm$ 0.05 nm.

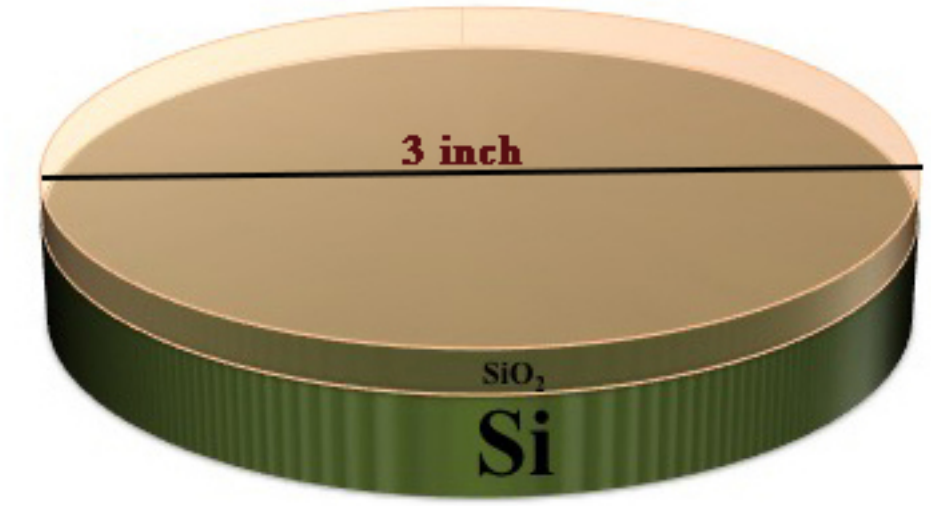


Figure 2.6: Schematic of $SiO_2$/Si wafers used for the present study.

## 2.5 Xray Photoelectron Spectroscopy (XPS)

X-ray photoelectron spectroscopy (XPS), also known as electron spectroscopy for chemical analysis (ESCA), uses soft X-rays to produce photoelectrons from the surface layers of atoms in a solid sample. The emitted electrons are analyzed according to their kinetic energy and the spectrum so produced is used to identify the elements present and their chemical states. The XPS spectra in this dissertation were obtained on a Kratos XPS spectrometer utilizing monochromatic $K_\alpha$ X-ray ($h\nu$=1486.6 eV), which is located at Georgia Tech University.

XPS is based on the photoelectric effect. Each atom has core electrons with characteristic binding energies that are conceptually equivalent to the ionization energy of that electron. When an X-ray beam strikes a sample surface, the energy of the X-ray photon can be absorbed by the core electron of an atom, and if the photon energy, $h\nu$, is large enough, the core electron will escape from the atom be emitted out of the surface. The emitted electron with the kinetic energy (KE) is referred to

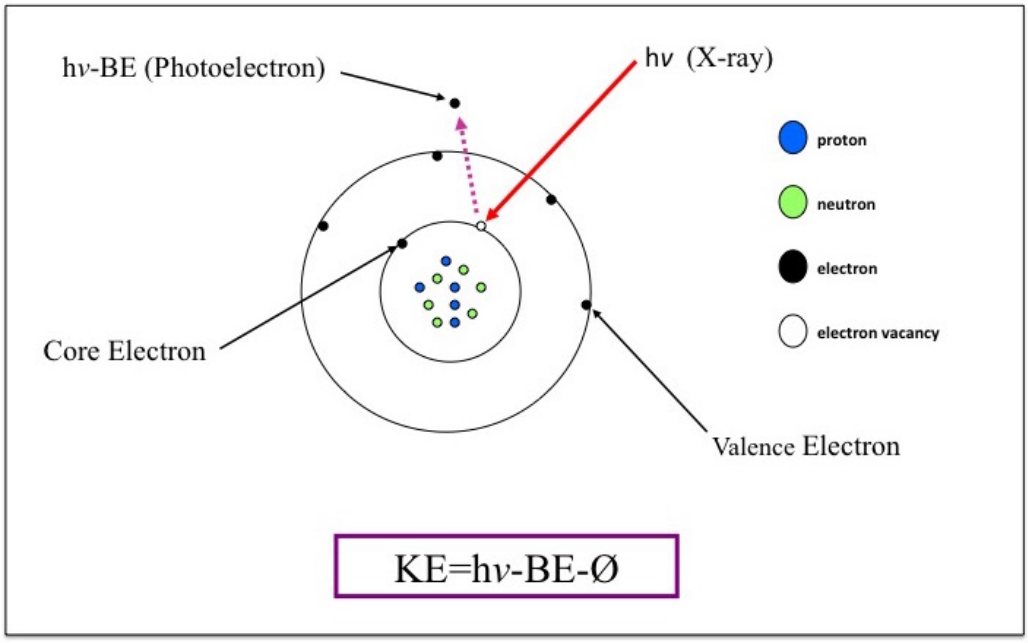


Figure 2.7: Xray photo electron spectroscopy: schematic of photoelectric effect.

as the photoelectron as shown in Fig. 2.7. The binding energy of the core electron is give by the Einstein relationship:

$$h\nu = KE + \phi + BE \tag{2.1}$$

where $h\nu$ is the X-ray photon energy( for $K_\alpha$ = 1486.6 eV), BE is the binding energy (unkown), KE is the kinetic energy of photoelectron(measured by the energy analyzer), and $\phi$ is the work function induced by the analyzer, about 4-5 eV.

The typical XPS spectrum of pristine and ion irradiated polycarbonate(PC) is shown in Fig 2.8. The details of peak fit analysis are discussed in Chapter 5.

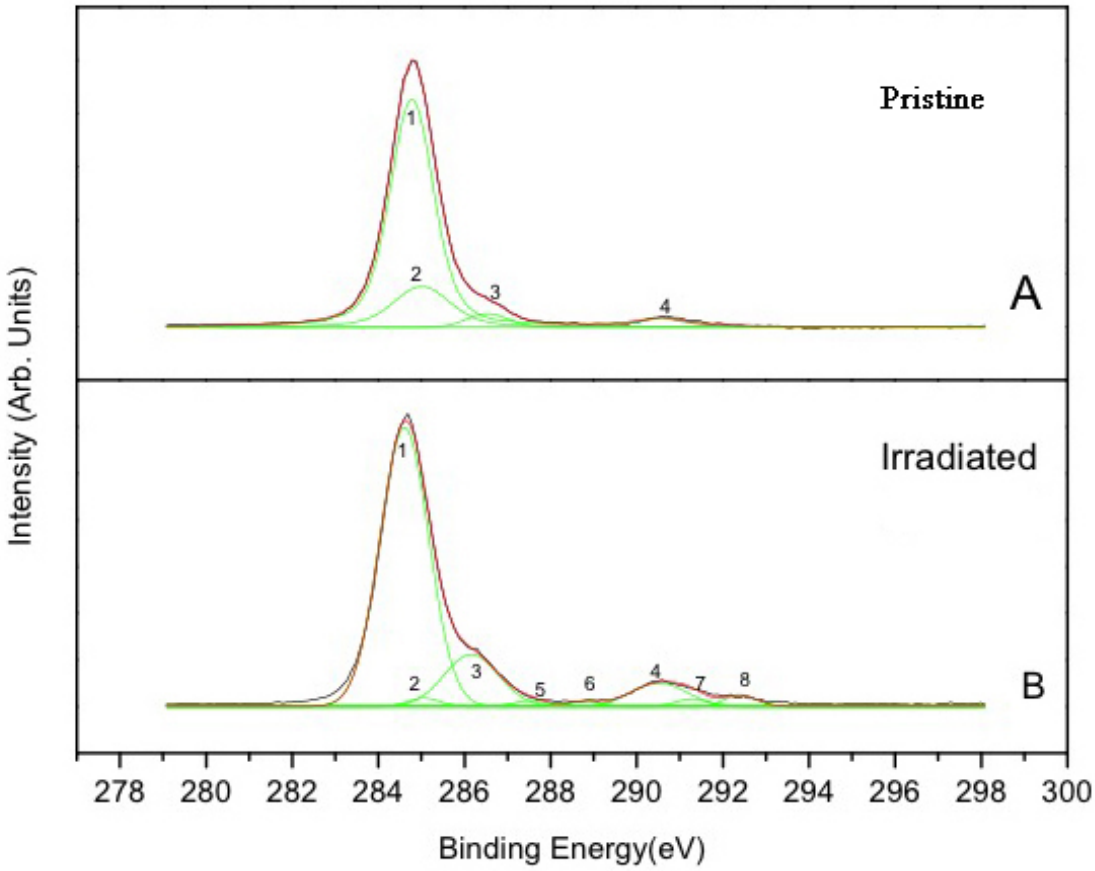


Figure 2.8: XPS high-resolution C 1S spectrum of (A) untreated PC (Lexan) and (B) Irradiated PC (Lexan).

# Chapter 3

# Growth Kinetics of Epitaxial $Cu_3Si$ Nanostructures

## 3.1 Introduction

This chapter investigates self assembled $Cu_3Si$ nanostructures that are attached to the silicon surface, either lying on top of the substrate, in epitaxial configuration, or are partially embedded in the surface, in endotaxial configuration. These nanostructures are grown using e-beam evaporation in UHV on different crystallographic Si substrates, namely p-Si(100), p-Si(111) and n-Si(111).

The major challenges for the controlled growth of metal silicides are complex metal-silicon phases over narrow temperature ranges, diffusion of metals into silicon and formation of defects. Ever since Cu was used to decorate the dislocations in Si, $Cu_3Si$ nanostructures were considered to be a promising substitute for Al and W as low resistance interconnects [56]. One of the major drawbacks of Cu is its fast diffusion into the Si substrate under thermal annealing, which leads to loss of adhesion at the interface or diffusion into active device regions that can deteriorate

device performance. One way to improve the stability of conventional metallization is to interpose a diffusion barrier between copper and silicon. A large number of materials have been adopted as diffusion barriers against Cu, such as Cr, W, Ta, WN, TaFe, TaN, TiN, TaC and $TiO_2$ [57–59].

In modern multilevel metallization structures, $SiO_2$ layers are usually employed as the effective diffusive barrier to isolate the interconnect lines of different levels and also to separate the active devices from the contacted metals. However, the growth mechanism of $Cu_3Si$ nanostructures on silicon substrates in the presence of an ultra thin $SiO_2$ barrier layer has been insufficiently studied [45, 60–62]. Studies of metal-oxide bonding and the thermal properties of such systems are also useful for understanding chemical interaction between the silicon substrate and the deposited metal species.

There has been extensive research interest in $Cu_3Si$ recent years due to its applications in energy storage devices such as batteries, solar cells etc. Recently their use has been studied for possible anodes in energy storage technology. Kim showed that an excellent electrochemical performance was obtained in a Si-$Cu_3Si$-Cu composite electrode. It has also been shown that, $Cu_3Si$ nanowires exhibit superior field-emission properties and serve as highly efficient anti-reflective layers and can also serve as an effective catalyst in reactions [18–21].

The synthesis of copper silicides has been reported using diverse methods involving relatively high temperatures (800-1100°C), which may not be desirable for many practical applications like optoelectronic devices, interconnects and displays etc [14, 45, 61, 63, 64]. In this chapter, we discuss the growth of $Cu_3Si$ nanostructures at much lower temperatures in UHV (450-600°C) on Si substrates in presence of ultra thin $SiO_2$ layer. In particular we probe the growth mechanism of $Cu_3Si$ nanostructures, which is believed to be due to the diffusion of metal and semiconductor

atoms into the regions of defect formation (voids) at the interface.

## 3.2 Fabrication Procedure

Single crystal, 3-inch diameter, silicon wafers of (111) and (100) orientations with the resistivity of 1-10 Ω cm were employed as substrates for the present study. Prior to the oxide growth, these wafers were cleaned following standard RCA clean procedure [65]. Following this cleaning, an ultra thin thermal oxide layer of approximately 1.5 ± 0.05 nm was grown via dry oxidation. Oxide-grown Si wafers were diced into 10 mm × 10 mm squares and mounted on Omicron style sample platen and were load-locked into a deposition chamber. Inside the deposition chamber, the $SiO_2$/Si substrates were resistively heated overnight (10-12 hours) using a HeatWave Labs, Inc. UHV button heater at a temperature of 500°C ± 25 °C. The annealing step led to the decomposition of $SiO_2$ and the creation of voids at defect sites, which act as nucleation centers for the growth of $Cu_3Si$ nanostructures. Thin Cu films were deposited in the temperature range of 450°C - 600°C using a Mcllister ebeam evaporator (EVAP) at a chamber pressure of $5 \times 10^{-6}$ Torr. The deposition was kept at 0.1 mA flux current while the deposition times varied from 1 min to 5 min. The sequence of steps involved in the growth process of $Cu_3Si$ nanostructures are shown in Fig. 3.1. Multiple steps involved in the growth of copper silicides from the selection of substrate to achieving self assembled growth are discussed in detail in the following sections.

### 3.2.1 Substrate Selection

For the present study we used silicon wafers of (111) orientation with p and n type dopants (Si-p(111) and Si-n(111) substrates) and (100) orientation wafers with

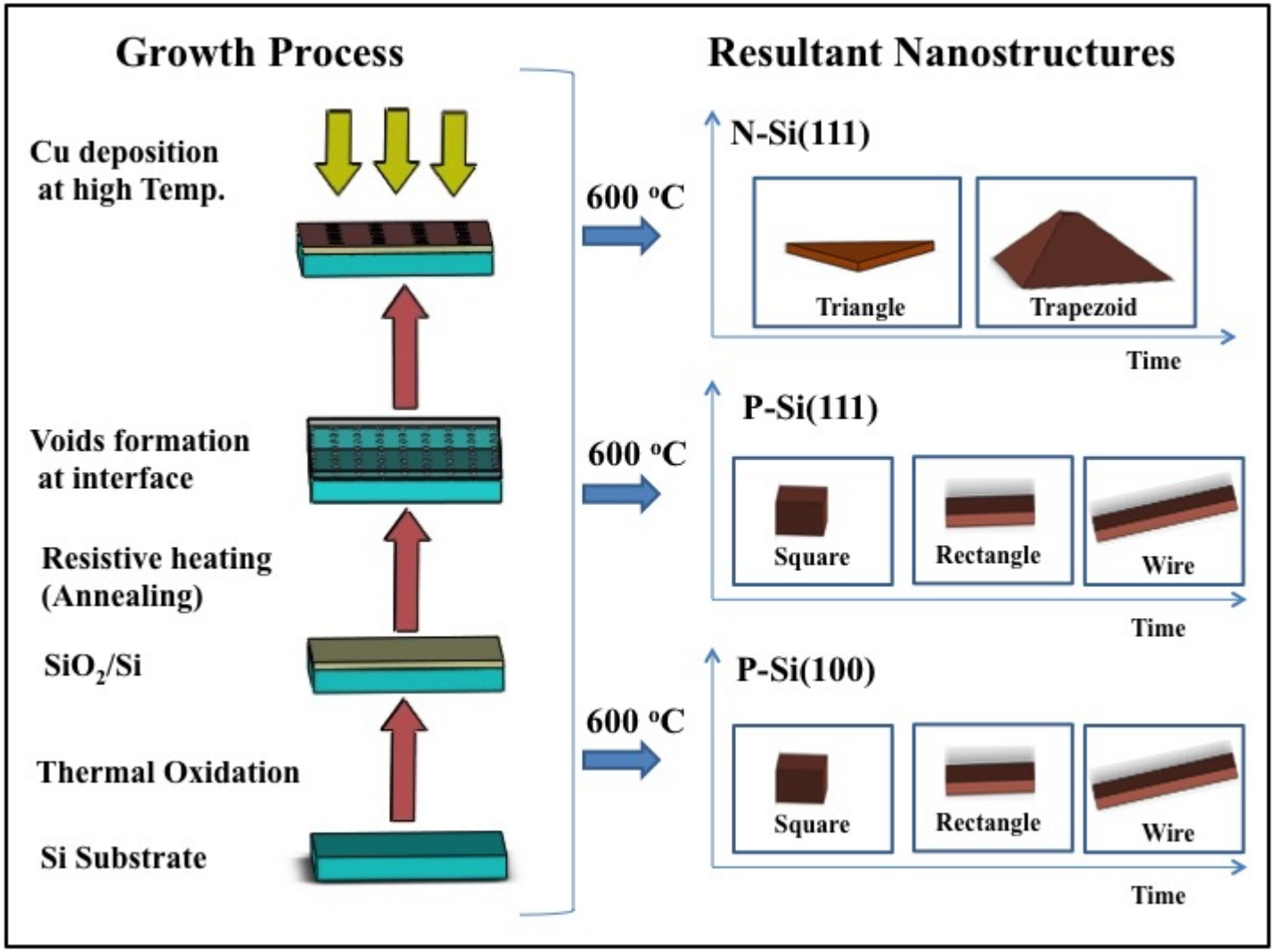


Figure 3.1: Growth process of $Cu_3Si$ islands and resultant nanostructures.

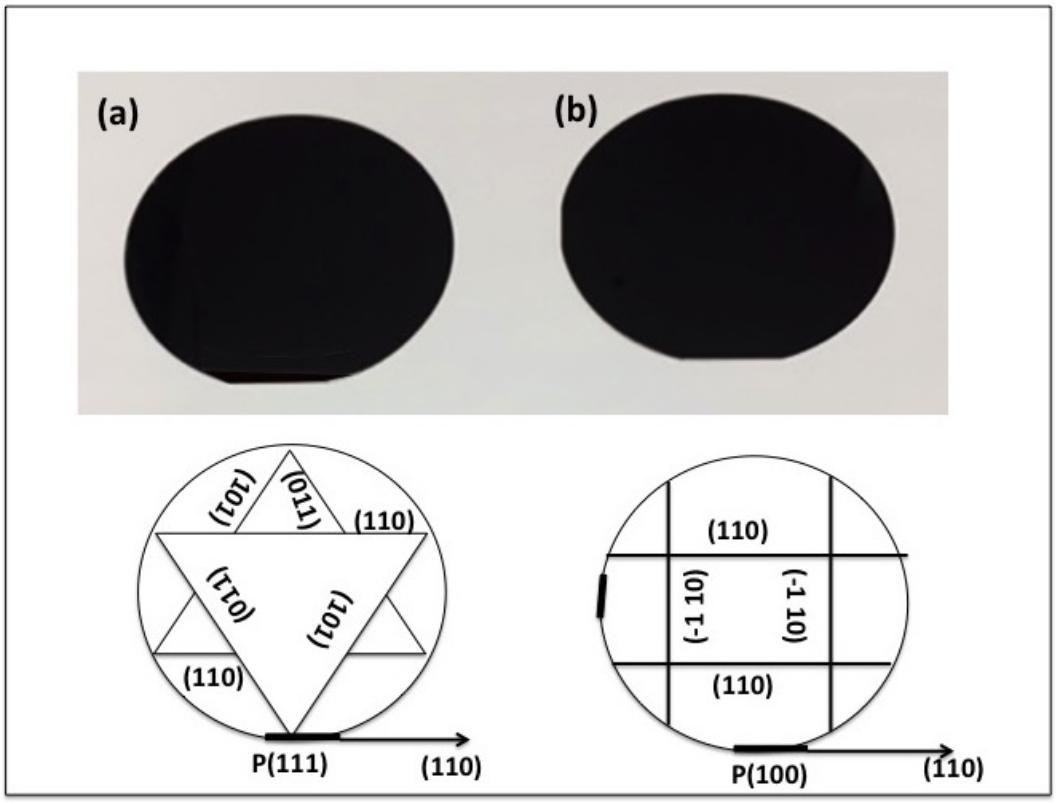


Figure 3.2: (a) Si-p(111) (b) Si-p(100) substrates.

p type dopant, i.e Si-p(100). Typical p(111) and p(100) silicon wafers and crystal growth direction planes are shown in Fig. 3.2.

The detailed procedure for the wafer cleaning and dry oxidation are given in Appendix B.

### 3.2.2 Annealing

The experimental setup used for the growth of $Cu_3Si$ nanostructures is shown in Fig. 3.3. The setup is equipped with a UHV chamber, manipulator, electron beam evaporation gun, resistive heater, water coolant and temperature probe. An Omicron style sample holder is attached to the end of a manipulator which has both translational (x, y, z) and rotational ($\theta$) capabilities. It is used to transfer the sample

in and out of the chamber (loading and unloading). An electron beam gun is used to deposit copper in situ. A HeatWave Labs, Inc. UHV button heater capable of resistively heating a sample up to 1000°C is attached to the manipulator directly underneath a mounted sample.

Prior to Cu depositions,the $SiO_2$/Si wafers were diced into $\sim$ 10 mm x 10 mm squares. Each strip was mounted on an Omicron style sample holder as shown in Fig. 3.6 that could be load locked into the deposition chamber. These $SiO_2$/Si substrates were resistively heated overnight (10-12 hours) using a HeatWave Labs, Inc UHV button heater at temperature of 500°C $\pm$ 25 °C to remove surface carbonaceous impurities and were then cooled down to room temperature. K-type thermocouple spot welded on to the sample platen were used to monitor the temperature with an accuracy of $\pm$ 3 °C.

The annealing step led to the decomposition of the ultrathin $SiO_2$ and the formation of voids at the defect sites as shown in Fig. 3.5. This step would also remove any unwanted hydrocarbons from the surface. The defect sites would serve as nucleation centers for the growth of $Cu_3Si$ nanostructures. It is known from prior studies that an annealing step is required to successfully form $Cu_3Si$ nanostructures on $SiO_2$/Si. To understand the role of this step in the later formation of nanostructures, we prepared a subset of samples for SEM analysis that were annealed at temperatures of 500 - 550°C. The SEM images revealed a variation in the density of voids at the sample surfaces which can be seen from the three representative images shown in Fig. 3.7. The density of voids are on the order of 7.98 $\times$ $10^4 cm^{-2}$ at 500°C. As the annealing temperature increased from 525°C to 550°C, the density of voids increased from 1.60 $\times$ $10^6$ $cm^{-2}$ to 3.31 $\times$ $10^6$ $cm^{-2}$. An examination of these voids with EDX revealed them to be bare Si regions of sizes 2 - 18 $\mu m^2$. Across this narrow temperature range, the data in Fig. 3.5 show that the density of these voids appears

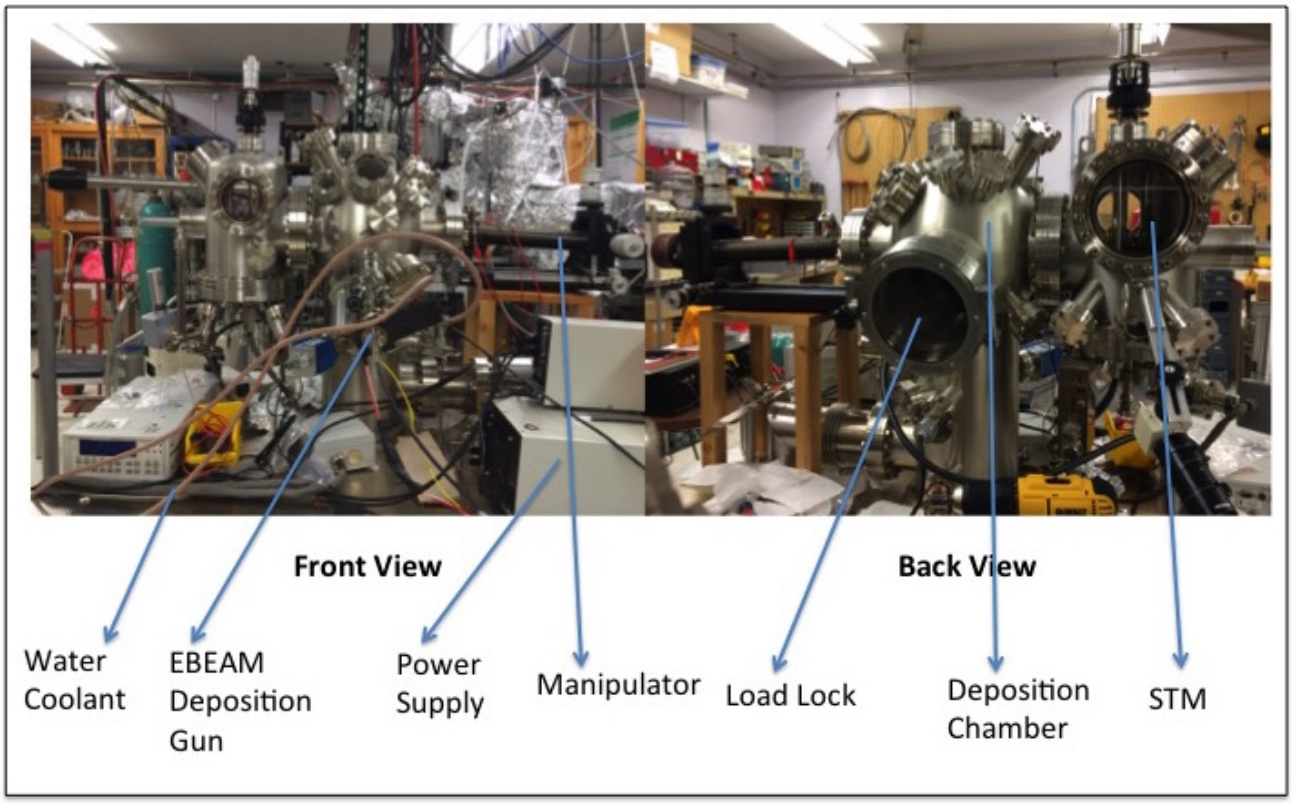


Figure 3.3: Overview picture of $Cu_3Si$ growth system at Clemson University. The system consists of a UHV chamber for fabrication of self assembled Cu-Si nanostructures, resistive heater setup for heating the substrate overnight , EVAP gun for deposition of copper, manipulator with X,Y, Z and theta motion and an STM for characterization.

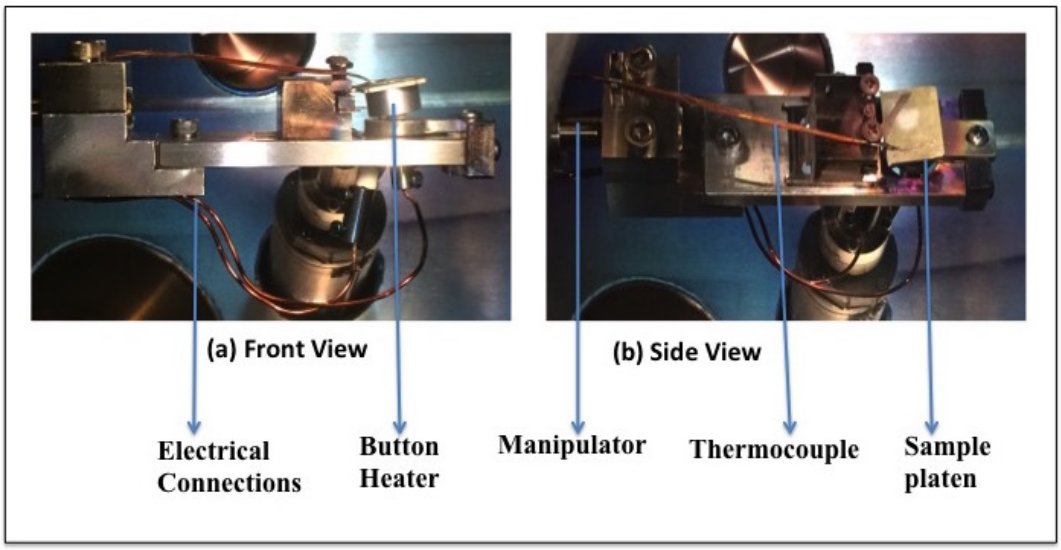


Figure 3.4: Picture of Omicron style sample holder setup to mount the substrate and to resistively heat.

to grow linearly with temperature. Although it is highly likely that much smaller void regions are present on our samples below the resolving limit of our SEM analysis, the presence of voids and their distinct dependence on temperature indicates that they may play an important role in $Cu_3Si$ nanostructure formation within our optimal temperature range.

### 3.2.3 Thin Film Deposition

Copper was deposited on our samples in the temperature range of 450°C-600°C using a 0.1 mA flux current with an Mcallister ebeam evaporator (EVAP) at a pressure of $5 \times 10^{-6}$ Torr. The deposition times varied from 1 min to 5 min yielding a growth rate of 1 ML/min. This method of depositing metal atop a substrate while simultaneously heating the substrate is known as reactive deposition epitaxy (RDE). The detailed procedure for electron beam evaporation is given in Appendix B.

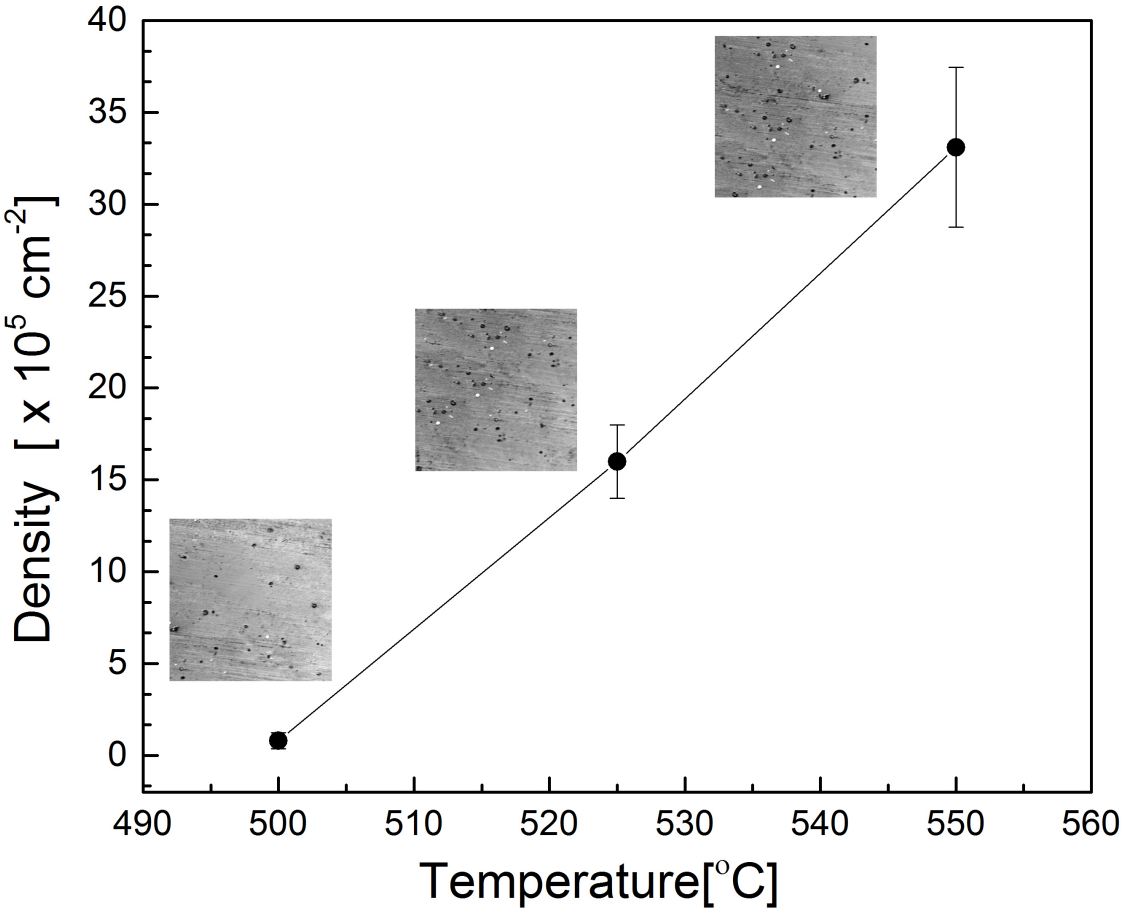


Figure 3.5: Density of void formation on $SiO_2$/Si(111) substrates at defect sites as a function of the annealing temperature.

### 3.2.4 Material Composition with XRD

From XRD data it is confirmed that $Cu_3Si$ possesses hexagonal crystal structure with P$\bar{2}$ml space group. According to Cu-Si phase diagram, $Cu_3Si$ comprises of three polymorphs. These phases transform at different temperature zones and are denoted as $\eta'' - Cu3Si$, $\eta' - Cu3Si$ and $\eta - Cu3Si$. $\eta'' - Cu3Si$ is the equilibrium phase at room temperature, which has been studied by Solberg and Weber *et al.* During the cooling process, a phase transformation of either $\eta\prime$ (above 531°C ) $\rightarrow \eta''$ or $\eta$ (above 600°C )$\rightarrow \eta'$ occurs. The $\eta''$structure is considered to be a periodic two-dimensional stacking fault of the $\eta'$ unit cell that has super lattice structure of $\eta$ phase with a space group of R$\bar{3}$[66, 67].

The lattice parameters of $\eta$ phase of $Cu_3Si$ were determined to be a = 4.06 Åand c = 7.33 Å, where as Si ( (111) and (100) ) condenses in the diamond structure with a cubic lattice constant of a=3.84 Å. The misfit along 'a' direction for 2-D lattice Si and $\eta-$ $Cu_3Si$ is -5.41 % and misfit along 'c' direction is $\sim$ -47.6 %. To minimize the strain energy, the silicide crystals grow preferentially along the low lattice mismatch direction, leading to the formation of nanowires.

In our XRD spectrum shown in Fig. 3.6, except for the Cu(111) and Si(111) peak, no other peaks appeared when the Cu deposition temperature was below 250°C. No $Cu_3Si$ were peaks observed below 250°C,which implies that $SiO_2$ acts as a perfect insulating barrier up to 250°C. It shows that continuous Cu films were formed without forming copper silicides below this temperature. The Cu peak disappeared when the deposition temperature was beyond 250°C, which implies that Cu has acquired enough mobility to diffuse to the interface and react with Si to form the $Cu_3Si$ phase. This suggests that formation of silicides is controlled by the interdifussion of Cu and Si. The Cu atoms in the Cu/$SiO_2$/Si system interact with the Si atoms at the

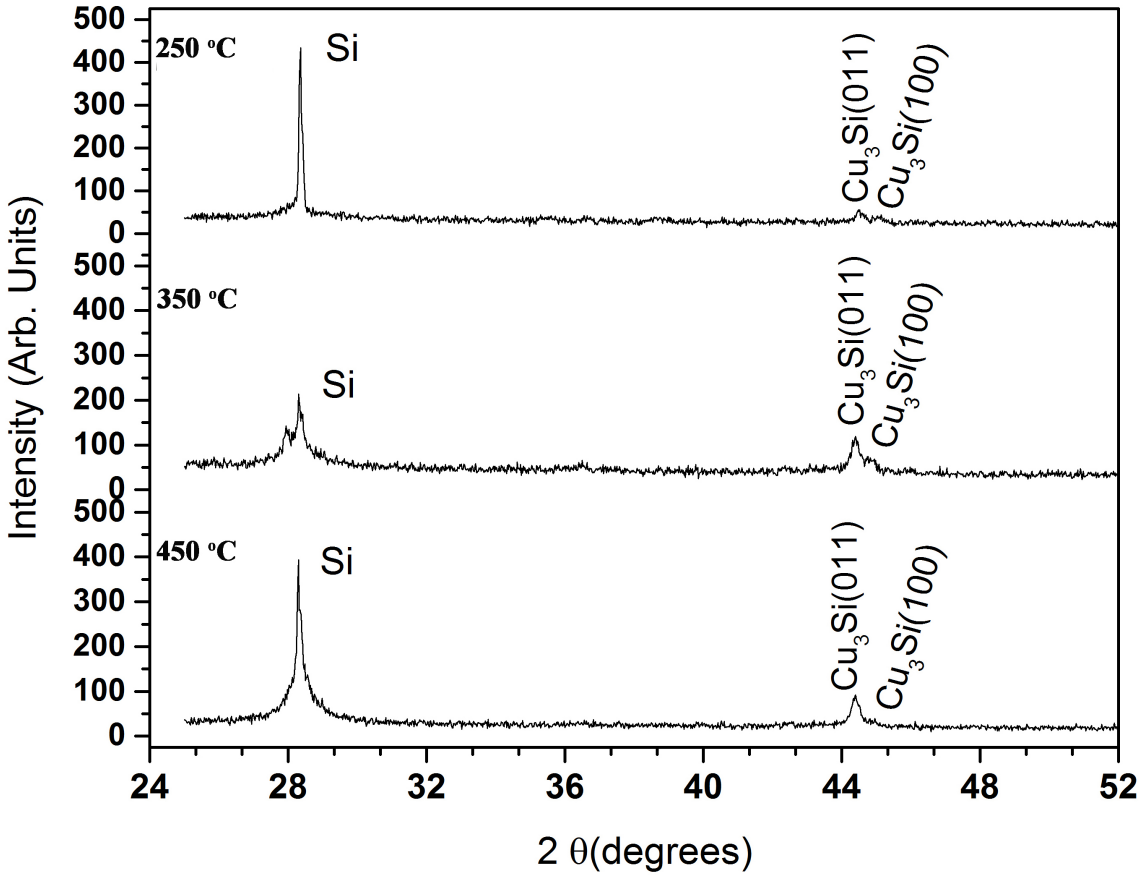


Figure 3.6: X-ray powder diffraction patterns of $Cu_3Si$ nanostructures grown on $SiO_2$/Si(111) in the temperature range from 250-450°C. Peaks in the $Cu_3Si$ diffraction pattern are labeled with Miller indices, (h k l) indicating the set of lattice planes responsible for that diffraction peak.

interface and form the $Cu_3Si$ phase when the deposition temperature is above 250°C. As depicted in the Fig. 3.6, as the deposition temperature increased to 450 °C, three peaks at 28°, 44.6° and at 45.2° are visible. The peak at 28° corresponds to Si(111) and the $Cu_3Si$ phase exhibiting diffraction peaks at 44.6° and at 45.2°, is the main phase present on the surface, based on XRD. XRD peak intensities are weak due to low surface coverage of $Cu_3Si$, but they indicate $Cu_3Si$ islands are crystalline.

### 3.2.5 Material Composition with EDAX

One of the most widely used and least expensive techniques to determine the chemical identity of the sample is EDAX. We performed EDAX analysis on SEM images of Cu deposited on a $SiO_2$/Si(111) substrate at 450°C to identify the chemical composition. EDAX spectrum analysis shown in Fig. 3.7(b) indicates that the island phase is composed of 22.84% Si and 72.26% Cu and 4.90% of oxygen, which is consistent with the $Cu_3Si$ phase determined by XRD. The small percentage of oxygen is due to the ultra thin oxide layer on the Si surface. Ignoring the oxygen reading within the crystalline region, the Cu:Si ratio becomes approximately 3:1, which suggest a $Cu_3Si$ phase.

## 3.3 SEM Results and Discussion

To understand the growth kinetics and the driving force responsible for the growth of $Cu_3Si$ islands on silicon substrates, Cu was deposited on $SiO_2$/Si substrate at low temperatures (T < 450 °C), and in an optimal temperature range (450°C <T< 600°C) for varying deposition time ranging from 1 to 5 min yielding a deposition rate of 1 ML/min. Scanning electron microscopy(SEM) imaging was performed to verify the results of e-beam evaporation of Cu on Si at 600°C. Since, the SEM is not

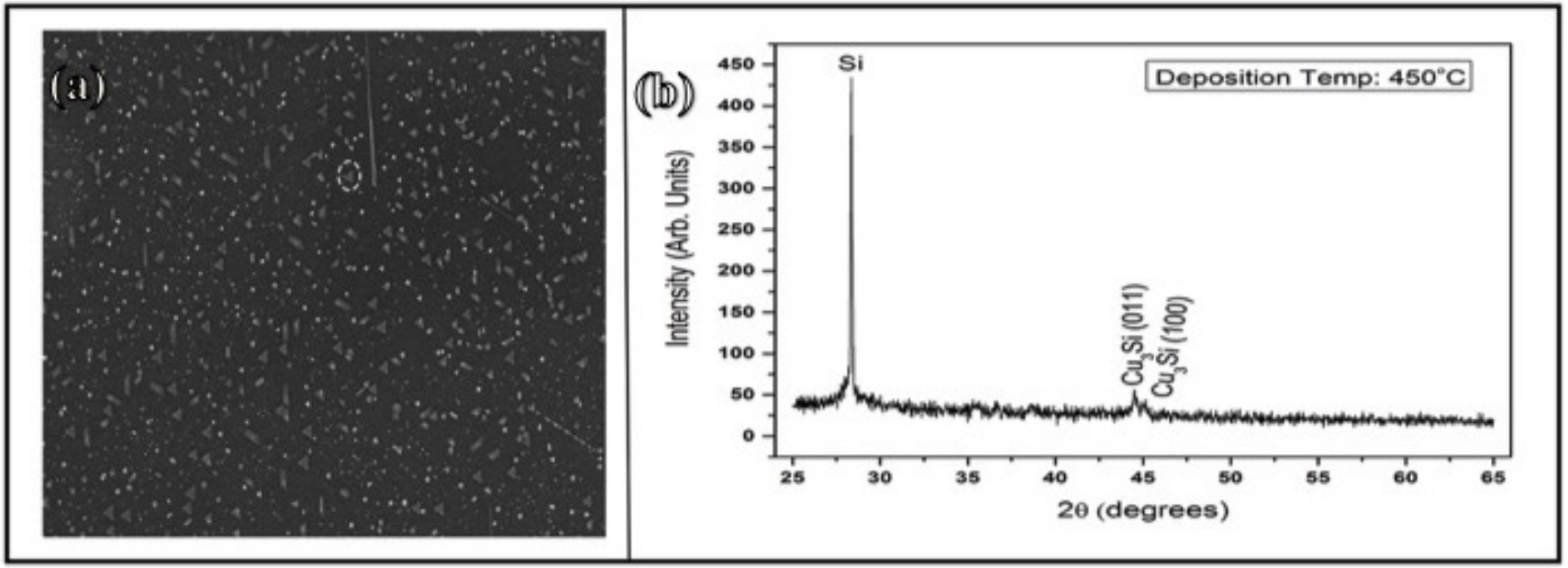


Figure 3.7: (a) SEM image of Cu deposited on $SiO_2$/Si(111) at 450°C. (b) XRD pattern of $Cu_3Si$ islands grown on $SiO_2$/Si(111) at 450°C.

connected to our UHV e-beam evaporator setup, the samples were removed from the chamber for imaging. A Hitachi S4800 model SEM was used to view the specimens with dimensions in the micrometer to nanometer range.

### 3.3.1 Temperature Dependent Growth Kinetics of $Cu_3Si$ nanostructures

In Fig. 3.8 the $Cu_3Si$ island concentration on n-Si(111), p-Si(111) and p-Si(100) substrates with temperature obtained from SEM images are shown. The procedure followed to calculate the densities of $Cu_3Si$ islands is shown in Apendix A. Error bars shown in the Fig. 3.8 represent 1 standard error of at least 100 islands. As the deposition temperature increases the island concentration decreases. The growth kinetics of the $Cu_3Si$ phase investigated by previous researchers has concluded that the formation of $Cu_3Si$ is by interdiffusion of Cu and Si. The activation energies observed by the previous researchers vary from 0.8 to 1.84 eV over a temperature range of 450 to 800K [68].

The density of $Cu_3Si$ islands deposited on the n-Si(111) substrate are represented with filled squares where the average area is shown in the inset. The mean area of these increases from 1.2 x $10^4$ $nm^2$ to 6.7 x $10^4$ $nm^2$ and the density of the islands decreases from 2.7 x $10^{10}$ $cm^{-2}$ to 5.7 x $10^6$ $cm^{-2}$ within the temperature range of 400-600°C.

In Fig. 3.8, the surface density of $Cu_3Si$ islands deposited on p-Si(111) substrate are represented with filled triangle. The mean area of the islands increases from 1.5 x $10^5$ $nm^2$ to 7 x $10^5$ $nm^2$ and the density of the islands decreases from 1.4 x $10^{10}$ $cm^{-2}$ to 1.3 x $10^7$ $cm^{-2}$ within the temperature range of 400-600°C.

The surface concentration of $Cu_3Si$ islands deposited on p-Si(100) substrate

are shown as open squares in Fig. 3.8. The mean area of islands increases from 4.8 x $10^3$ $nm^2$ to 1.2 x $10^5$ $nm^2$ and the density of these islands decreases from $10^8$ $cm^{-2}$ to $10^6$ $cm^{-2}$ within the temperature range of 400-600°C.

The activation energies for the epitaxial growth of $Cu_3Si$ islands on silicon substrates capped with ultra thin oxide layer ($\sim$ 2 nm) was determined using the Arrhenius equation [3.1].

$$k^2 = K_a exp[\frac{-E_a}{K_b T}] \tag{3.1}$$

where $K_b$ is Boltzmann's constant, $E_a$ is the activation energy and $K_a$ is the pre-factor. Activation energies of $Cu_3Si$ islands determined from the slope of a Arrhenius type plot to be 1.17 eV for n-Si(111) and 1.02 eV for p-Si(111) and 0.94 eV for p-Si(100) substrates. Our experimental findings closely match with the activation energies reported by previous researchers[60, 68].

The relationship between the average island area vs temperatures was shown as inset an in Fig. 3.8. Since the key process in island growth is thermally activated surface diffusion of copper atoms, the decrease in island concentration and increase in the island surface area with temperatures is caused by the increases in the diffusion coefficient of copper atoms with growing temperature. Furthermore, the ultra thin oxide layer of $\sim$ 2 nm on the Si surface is not an effective diffusion barrier to Cu at high temperatures, and therefore the metal atoms can diffuse through the voids formed on the thin oxide due to overnight annealing and react with the Si below the oxide to form the silicide.

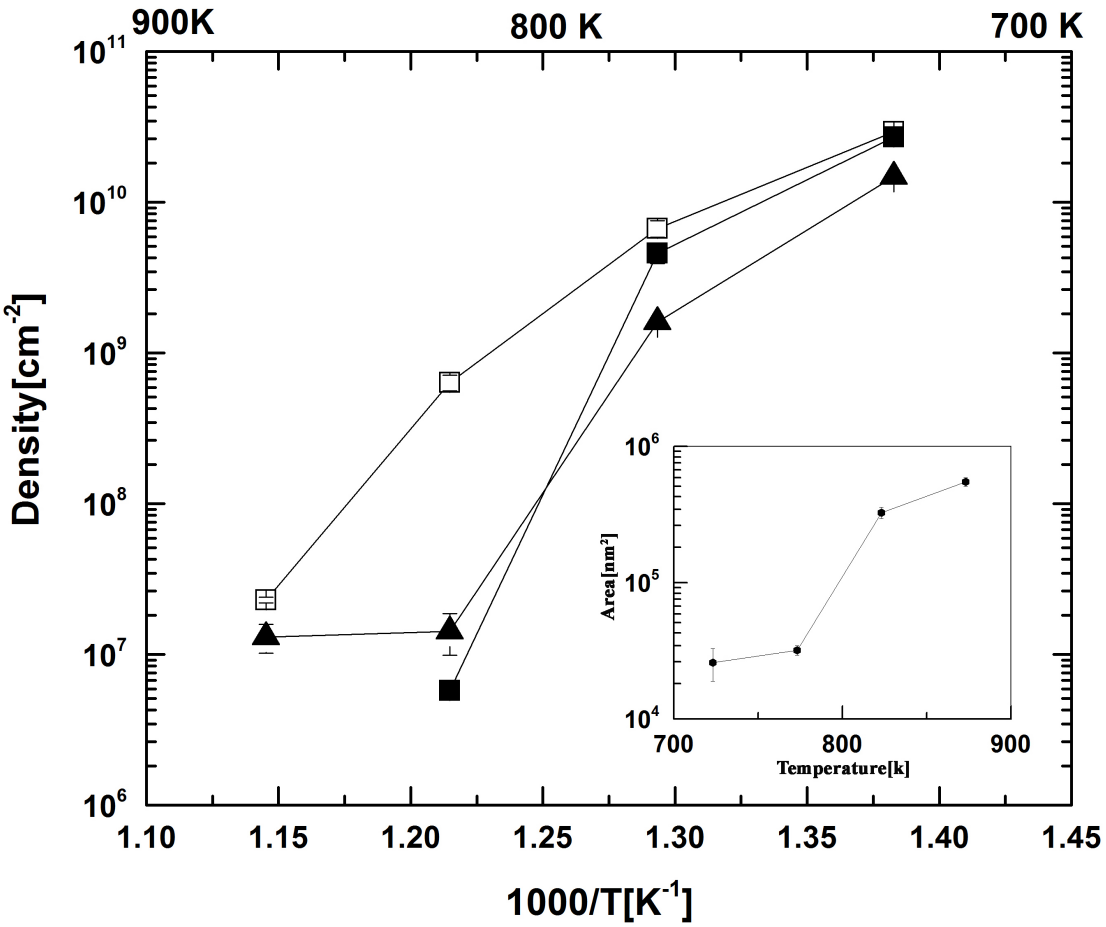


Figure 3.8: Arrhenius plot of $Cu_3Si$ island growth on n-Si(111), p-Si(111) and p-Si(100). Open squares represent the density of $Cu_3Si$ islands growth on p-Si(100) substrate where as filled triangle shows the growth on p-Si(111) and filled squares represent the growth on n-Si(111) substrate. Average area with temperature of $Cu_3Si$ island is shown in the inset.

### 3.3.2 Time Dependent Growth Kinetics of $Cu_3Si$ Nanostructures

The Cu-Si nanoislands grew in different directions and have various shapes. Triangular and trapezoidal were common on n-Si(111) substrate. Squares, rectangles and nanowires were common types on p-Si(111) and p-Si(100) substrates. This could be attributed to the surface properties of the silicon substrate. There was an observed shape transition from triangular to trapezoidal on n-S(111) and from square to nanowire on p-Si(100) and p-Si(111) with deposition time, which will be explained in the light of a strain induced shape transition model proposed by Tersoff and Tromp[48]. This model is explained in detail in the following section.

#### 3.3.2.1 Strain Driven Shape Transition Model

The mechanism for generating a nanowire shape depends on the material system. Several models have been suggested where the mechanisms are ascribed to strain, energetics, and kinetics. Tersoff and Tromp have considered energetics to explain the shape transition and formation of wire structures [48]. This model also requires well-separated islands and continuous deposition at high temperatures, ideally our experimental conditions, to study island elongation. In fact our results are in agreement with the strain driven shape transition model.

According to the model, the shape and the dimensions of an island rely on the interplay between extra surface and interface energy and elastic relaxation energy of the strained islands. The energy $E$ of an island of height $h$, contact angle $\theta$ , and volume $V$ is written as

$$\frac{E}{V} = 2\Gamma(W^{-1} + L^{-1}) + h^{-1}(\gamma_i + \gamma_t - \gamma_s) - 2ch\big[\frac{1}{W}ln(\frac{We^{3/2}}{hcot\theta}) + \frac{1}{L}ln(\frac{Le^{3/2}}{hcot\theta})\big] \quad (3.2)$$

$$\Gamma = \gamma_e csc\theta - (\gamma_t + \gamma_s - \gamma_i)cot\theta,\ c = \sigma_b^2(1-\nu)/2\pi\mu,\ V = LWh$$

where $W, L, h$ and $V$ are the width, length, height and volume of the island, $\gamma_t$ , $\gamma_s$, $\gamma_i$ are the surface energies per unit area of the island top surface, substrate surface and island side facet, $\gamma_e$ is the island- substrate interface energy respectively and $c$ depends on the island bulk stress ($\sigma_b$) and Poision ratio $\nu$. The first term in this equation, gives the change in the surface energy, the second term is due to interface energies, and the third term describes bulk stress in the island due to substrate-island lattice mismatch ($\sim 4 - 40\%$ )[69]. An island under stress exerts a force on the substrate surface, which elastically distorts the substrate. This lowers the energy of the island at the cost of some strain in the substrate.

The optimal trade off between surface energy and strain is obtained by minimization of $E/V$ with respect to $s$ and $t$ treating $h$ as constant. During the deposition process, the probability of an approaching atom sticking to the edges is more probable, compared to diffuse to the top surface of the island. As a result, the height grows slowly compared to length and width, and may be treated approximately constant. When L = W= e$\alpha_0$, the critical size $\alpha_0$ is given by

$$\alpha_0 = e\phi h \quad exp(\Gamma/ch) \tag{3.3}$$

A compact shape ($L = W$) is stable for island sizes $L, W > \alpha_0$. As soon as the island dimensions exceeds the critical value $\alpha_0$ by a factor e(2.718), the compact shape becomes unstable and a transition to elongated shape occurs. As the island grows, the width tends to go back to its critical value $\alpha_0$ whereas island length keeps increasing rapidly ( $L/W > 1$).

#### 3.3.2.2 Self Assembled Cu-Si Nanowires on n-Si(111)

Figures 3.9(a)-(d) show SEM micrographs of e-beam evaporation of Cu onto a $SiO_2$/Si-n(111)substrate at 600°C for 2, 3, 4 and 5 mins yielding a deposition rate of 1 ML/min. The deposition rate of our e-beam evaporation gun was calibrated utilizing the EDX technique. Triangular and trapezoidal shapes were common among islands on $SiO_2$/n-Si(111) substrates from the SEM images. The primary growth mode is considered to be Volmer-Weber (VM) since areas of uncovered substrate coexisted along with 3D nanostructures and also due to the absence of a wetting layer when the deposition thickness is as low as 1 ML [27]. The physical traits of the $Cu_3Si$ islands appear to depend on the type of Si substrate, i.e (111), (100) and dopant type(p or n). Since the (111) plane exhibits three fold symmetry, triangular shape reflects the three fold symmetry of the substrate. Orientations of the self assembled islands were found to be along the [011], [101] and [110] directions as shown in Fig. 3.11(b) with 60° angle between the two nearest vectors.

The growth kinetics of $Cu_3Si$ nanostructures on $SiO_2$/n-Si(111) substrate, i.e island density and area dependence with deposition time from the SEM images are shown in Fig. 3.10. As shown in Table 3.1, the density of the islands decreases from 1.99 x $10^8$ $cm^{-2}$ to 1.69 x $10^6$ $cm^{-2}$ and mean area of the islands increases from 20.2 x $10^4$ $nm^2$ to 79.2 x $10^4$ $nm^2$ with deposition time at a constant deposition temperature of 600°C.

The kinetics of island nucleation is similar to the diffusion growth process shown in Fig. 1.2. The island nucleation density (N(t)) increases with time, eventually saturating at the value 1.56 x $10^8$ $cm^{-2}$. No perfect shaped island growth was observed for 1 ML deposition. Triangular shaped nanostructures appeared as the deposition thickness increased to 2 ML. So, growth of triangular shaped islands starts between 1

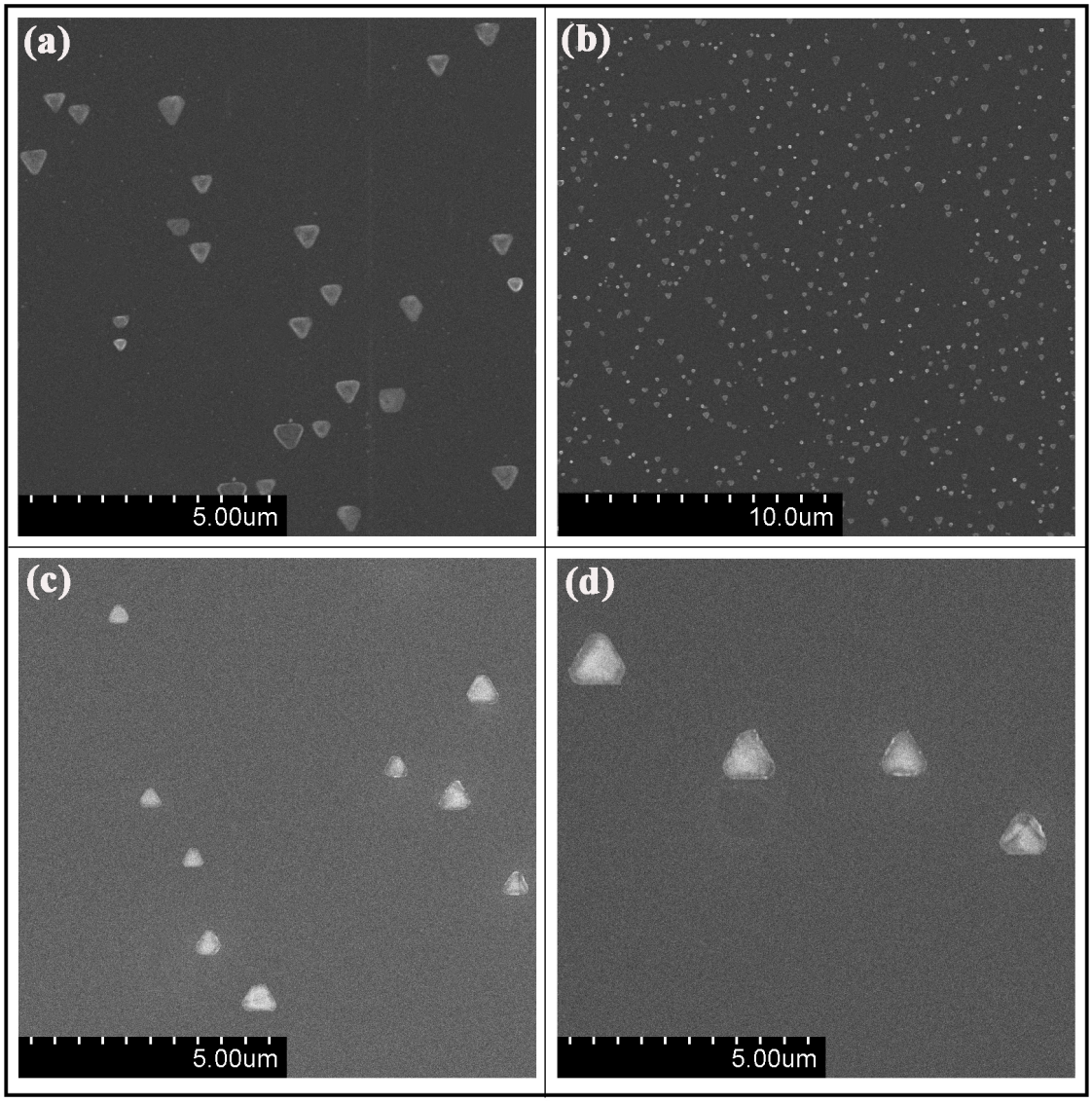


Figure 3.9: Cu deposited on $SiO_2$/Si-n(111) at 600°C for a deposition time of (a)2 min (b) 3 min (c) 4 min (d) 5 min.

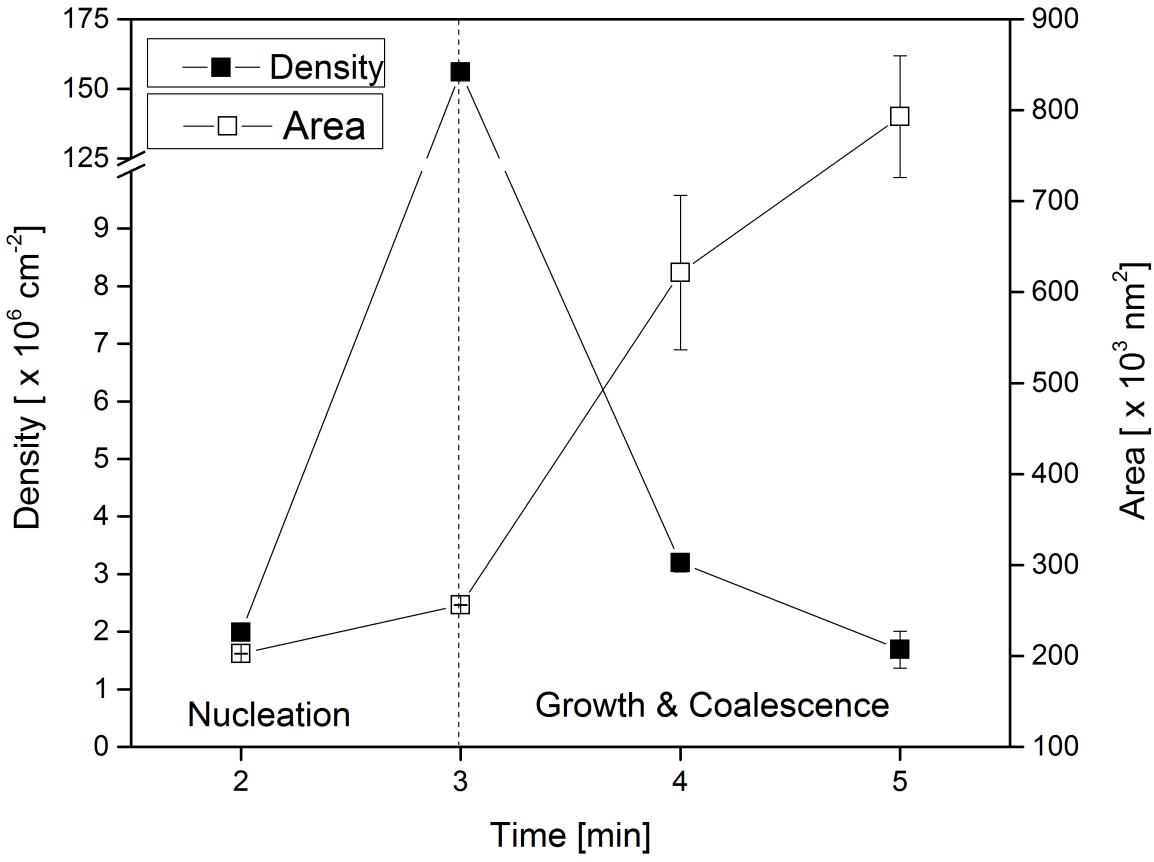


Figure 3.10: Growth Kinetics of $Cu_3Si$ islands grown on SiO2/n-Si(111) substrate at 600°C with deposition time.

and 2 ML deposition thickness. It can be inferred from Fig. 3.10, that the saturation value of N(t) could be between 3 to 4 ML as shown with dotted line. With further deposition, N(t) decreased and the area of the islands increased. Once the N(t) reaches the saturation value, the probability of atoms being captured by the existing islands is much higher compared to nucleation of new islands in order to achieve minimum surface energy. In the growth and coalescence region shown in Fig. 3.10, it can be seen that the area of the islands increases from 25.5 x $10^4$ $nm^2$ to 79.3 x $10^4$ $nm^2$ with deposition time. The increase in the area of the islands is attributed to the growth of islands, i.e existing islands capture the incoming atoms at the expense of new island nucleation and tend to grow larger. The decrease in the density of islands (N(t)) from 156 x $10^6$ $cm^{-2}$ to 1.69 x $10^6$ $cm^{-2}$ is due to coalescence of islands,i.e existing islands grow larger until they touch each other. If the deposition is further continued, coalescence of islands will continue until the voids between the grains are completely filled to form a thin film.

**Shape Transition:**

As shown in Fig. 3.11, a shape transition from triangular to trapezoidal was observed for $Cu_3Si$ islands growth on n-Si(111) substrate. According to the Tersoff model, the islands exhibit compact shape up to a critical size. Since n-S(111) exhibits three fold symmetry, the triangular shape would be the most stable and compact shape. Therefore, the islands up to the critical size are equilateral triangles (L1=L2) beyond which there is a shape transition from triangular to trapezoid (L2>L1) as shown in Fig. 3.14 (a) and (b). In the intial state of the growth the triangular islands are of size 2.02 x $10^5$ $nm^2$. These islands may be called self-assembling quasi-zero dimensional quantum dots [48]. For the largest triangular islands the area is $\sqrt{3}l^2/4$ = 2.56 x $10^5$ $nm^2$. The area of the island where the shape transition takes

| Substrate<br>Dopant(Orientation) | Time<br>min | L1<br>(nm) | L2<br>(nm) | Area<br>( x $10^3$ $nm^2$) | Density<br>(x $10^6$ $cm^{-2}$) |
|---|---|---|---|---|---|
| n(111) | 2 | 682.2 | 682.2 | 202.4 | 1.99 |
| n(111) | 3 | 768.8 | 768.8 | 255.9 | 156 |
| n(111) | 4 | 972.5 | 1019.4 | 621.4 | 3.2 |
| n(111) | 5 | 986 | 1035 | 729.9 | 1.69 |

Table 3.1: Dimensions of $Cu_3Si$ nanostructures grown on n-Si(111) substrates.

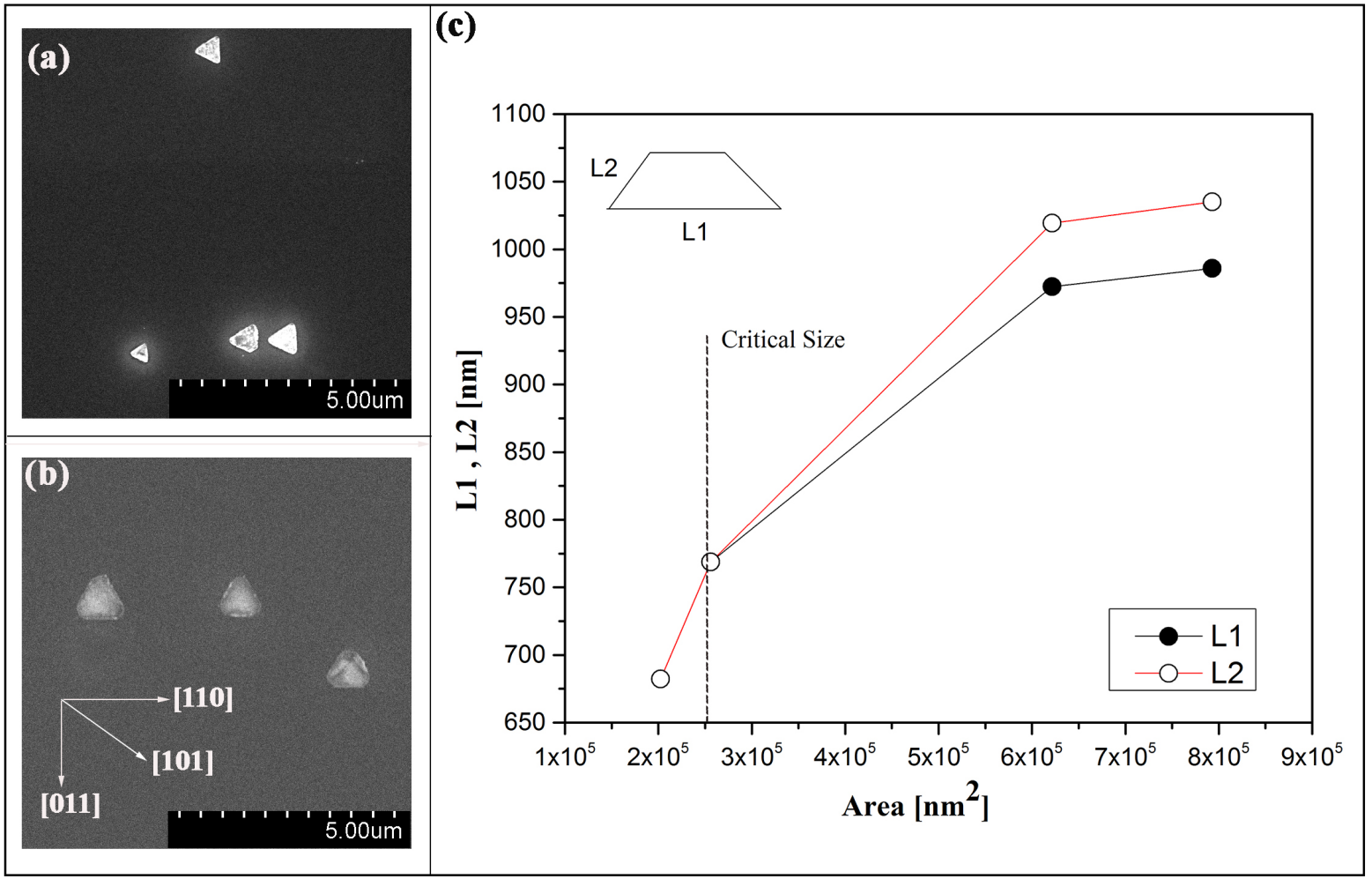


Figure 3.11: Two stages of $Cu_3Si$ island growth on n-Si(111) substrate area shown as imaged using SEM. In (a) Triangular islands (b) Trapezoidal islands (c) Dependence of lengths L1, L2 ( as shown in the inset) of the island vs surface area.

place is $e^2\alpha_0^2$ =2.56 x $10^5$ $nm^2$. This provides the critical size (e$\alpha_0$) = 505 nm, as represented in Fig. 3.11 with dotted line. Above this point, the shape transition to trapezoidal was observed as shown in Fig. 3.14(b). It is also interesting to note that L1 has decreased and L2 increases with area. However the sharp increase in the aspect ratio as predicted by the Tersoff model was not observed. Overall, our results are in reasonable agreement with the general theory of Tersoff and Tromp. It is also important to note that there will be partial strain relief due to dislocations formed during over night annealing and also during the deposition process. This might reduce the bulk stress or increase the critical size of the island but shouldn't impact the shape transition process. Orientations of these islands were found to be along [011], [101] and [110] without any preference as shown in Fig. 3.11(b).

#### 3.3.2.3 Self Assembled Cu-Si Nanowires on p-Si(111)

Figures 3.12(a)-(d) show SEM micrographs of e-beam evaporation of Cu onto a $SiO_2$/Si-p(111) substrate at 600°C for 1,2,4 and 5 mins yielding a deposition rate of 1 ML/min. Square, rectangular and nanowire shapes were common among islands on $SiO_2$/Si/p-Si(111) substrates from the SEM images as with n-Si(111).The primary growth mode is considered to be Volmer-Weber (VM). These self assembled islands are oriented along [011] and [101] directions with 90° as shown in Fig. 3.14(c) angle between the two nearest vectors.

The density and area of the $Cu_3Si$ islands deposited on $SiO_2$/p-Si(111) substrate from the SEM images are shown in closed and open squares in Fig. 3.13. As shown in Table 3.2, the density of the islands increases from 0.87 x $10^6$ $cm^{-2}$ to 7.34 x $10^6$ $cm^{-2}$ and decreases to 1.1 x $10^6$ $cm^{-2}$. The mean area of the islands increases from 4.5 x $10^5$ $nm^2$ to 9.81 x $10^5$ $nm^2$ with deposition time at constant deposition temperature 600°C.

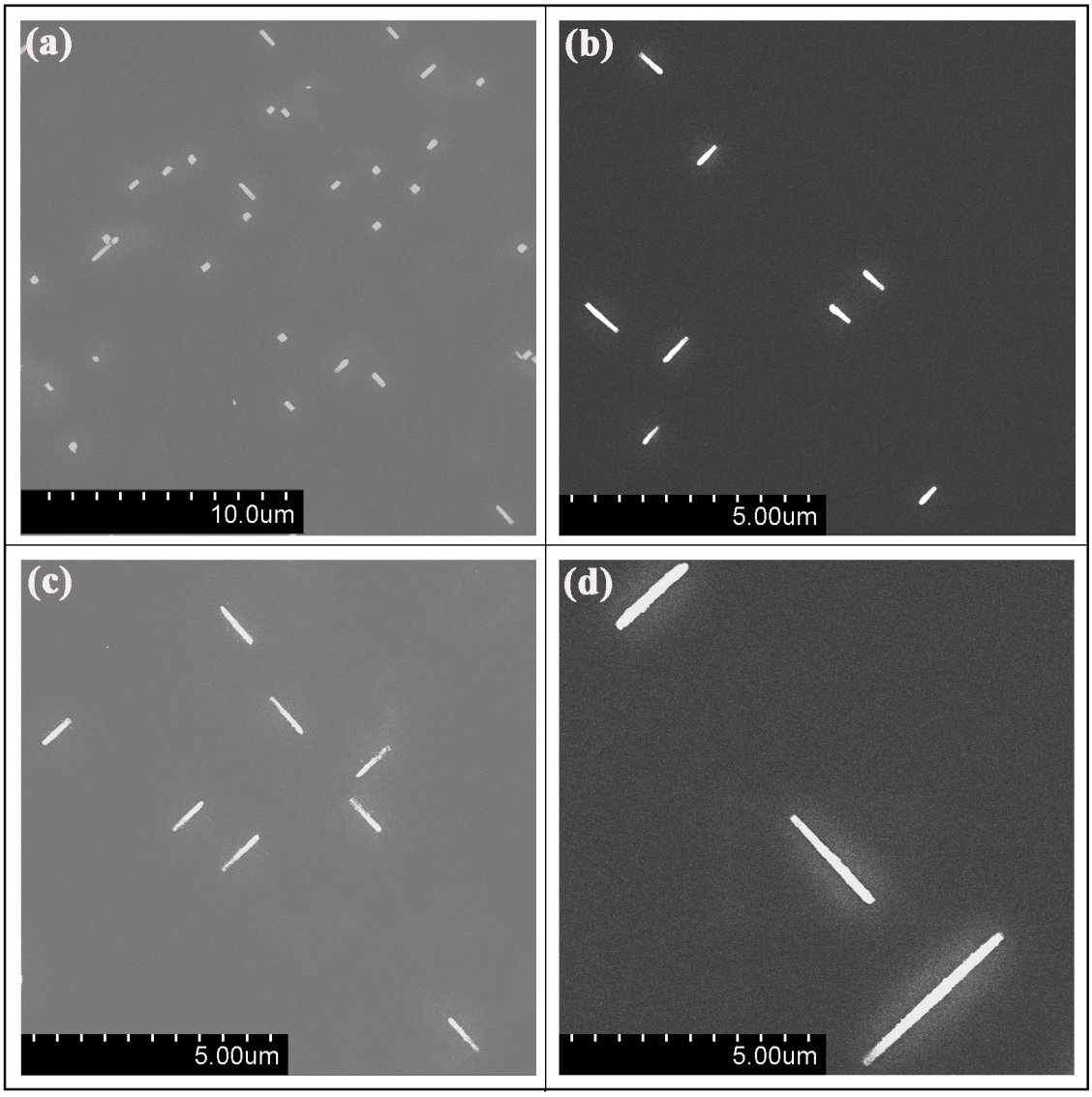


Figure 3.12: Cu deposited on $SiO_2$/Si-p(111) at 600°C for a deposition time of (a)1 min (b) 2 min (c) 4 min (d) 5 min.

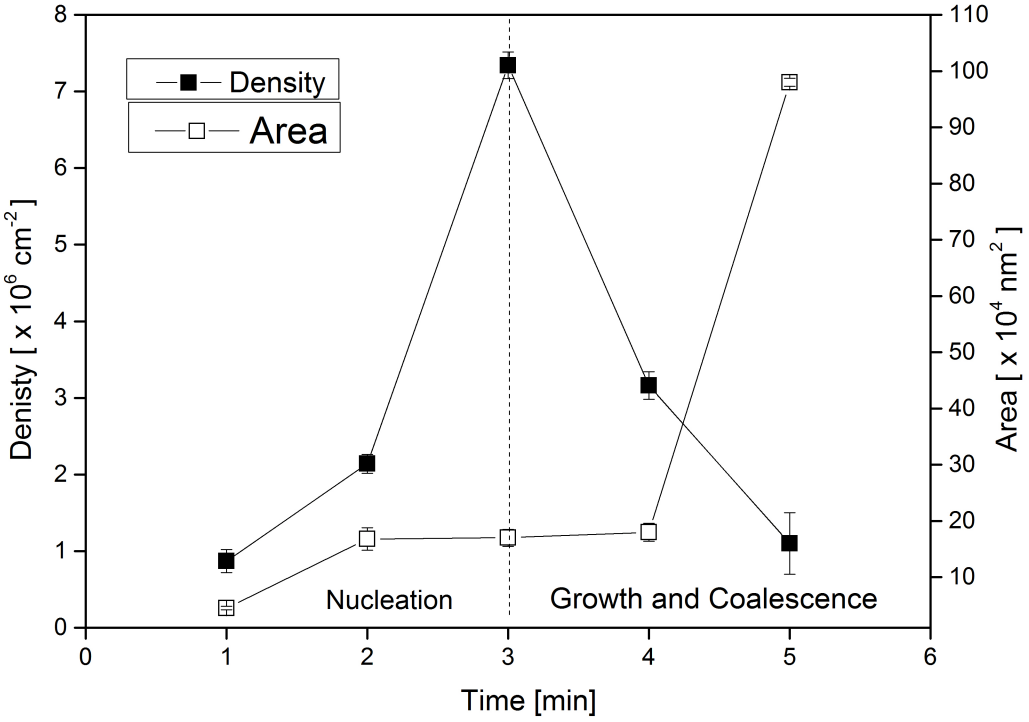


Figure 3.13: Growth kinetics of $Cu_3Si$ islands grown on $SiO_2$/Si-p(111) substrate at 600°C as a function of deposition time.

The kinetic of island nucleation exhibits similar behavior to that of the diffusion growth process shown in Fig. 1.2. The island nucleation density (N(t)) increases with time, eventually saturating at the value 7.34 x $10^6$ $cm^{-2}$. It can be inferred from Fig. 3.13, the N(t) increases with time up to 3 ML deposition before reaching a saturation value. With further deposition, N(t) decreases and the area of the islands increases. Once the N(t) reaches the saturation value, the probability of atoms being captured by the existing islands is much higher compared to nucleation of new islands in order to achieve minimum surface energy. In the growth and coalescence region it can be seen that the area of islands increases from 1.7 x $10^5$ $nm^2$ to 9.81 x $10^5$ $nm^2$ with deposition time. The decrease in the density of islands (N(t)) from 7.34 x $10^6$ $cm^{-2}$ to 1.1 x $10^6$ $cm^{-2}$ is due to coalescence of islands, i.e existing islands grow larger until they touch each other.

**Shape Transition:**

$Cu_3Si$ island growth on p-Si(111) substrates is shown in Fig. 3.14. The epitaxial island growth on n-Si(111) surface has three fold symmetry. The growth on p-Si(111) substrate is not the same as that of the n-Si(111) substrate. Up to a critical size the shape is observed to be square above which the shape transition to rectangular shaped islands. For the largest square island, the area is L X W = 4.5 x $10^4$ $nm^2$. The area of the island where the shape transitions takes place $e^2\alpha_0^2$= 4.5 x $10^4$ $nm^2$ provides the critical size ($e\alpha_0$) = 212 nm, as shown in Fig. 3.17 by the dotted line. It follows that for island length larger than 942 nm, L starts to increase much more rapidly while W decreases. As the area further increases the increase in length and slight decrease in the width lead to the formation of thin wires with sharp increase in aspect ratio ($\sim$ 7:1 ) as predicted by Tersoff model[48]. For the longer islands the width approaches towards the optimum value W $\sim$ 400 nm. We have observed aspect ratios as large as $\sim$ 8.5:1. All islands are oriented along [011] and [101] directions

| Substrate Dopant(Orientation) | Time min | Length (nm) | Width (nm) | Aspect Ratio | Area ( x $10^3$ $nm^2$) | Density (x $10^6$ $cm^{-2}$) |
|---|---|---|---|---|---|---|
| p(111) | 1 | 282.4 | 282.4 | 1:1 | 45 | 0.87 |
| p(111) | 2 | 942.2 | 193.4 | 4.9:1 | 168 | 2.14 |
| p(111) | 3 | 967.7 | 187.0 | 5.2:1 | 170 | 7.34 |
| p(111) | 4 | 1110.3 | 160.7 | 6.9:1 | 180 | 3.16 |
| p(111) | 5 | 2877.3 | 339.4 | 8.5:1 | 980 | 1.1 |

Table 3.2: Dimensions of $Cu_3Si$ nanostructures grown on p-Si(111) substrates.

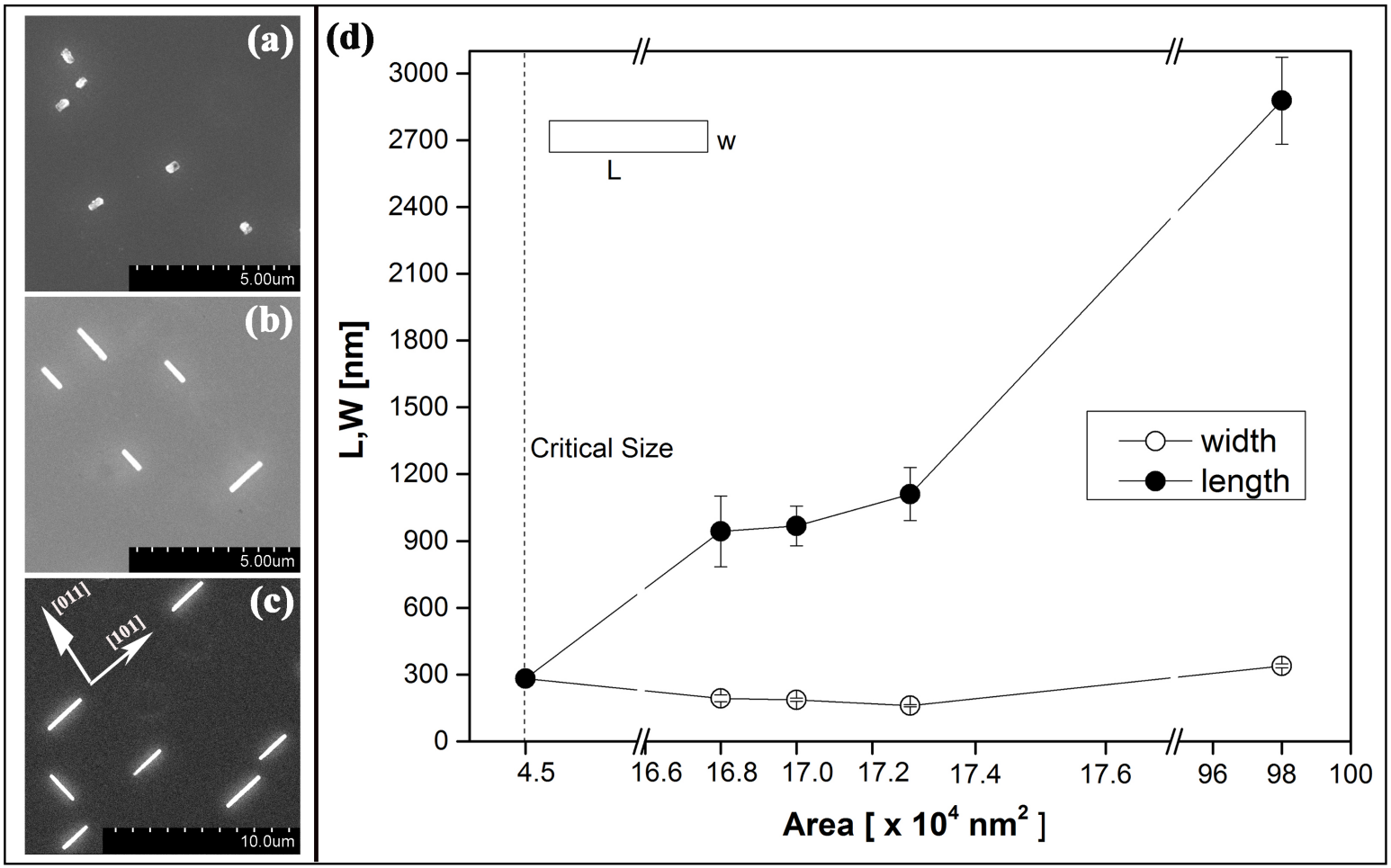


Figure 3.14: Three stages of $Cu_3Si$ island growth on p-Si(111) substrate are shown as imaged using SEM. In (a) Islands are square, until a shape transition to rectangular islands (b) rectangular islands (c) long wire shaped islands (d) Dependence of both island length L( closed circles) and width W(open circles) on the island surface area.

without any preference as shown in Fig. 3.14(c).

Irrespective of substrate orientation nanowires were grown on p-Si substrates and triangle shaped islands on n-Si substrates. This implies that the stress relaxation and shape transition is also dependent on the dopant type. Also, in p-Si copper precipitates are positively charged and repel $Cu^+$, thus suppressing the precipitation in the bulk and making out-diffusion predominant. In n-Si, the precipitation barrier disappears, and copper can easily precipitate in the bulk[68]. It is also known from the activation energy calculations, reaction rates of $Cu_3Si$ islands on all three substrates is not the same. p-Si(111) and p-Si(100) possessing approximately the same activation energies tend to undergo nanowire shape transition where as n-Si(111) with high activation energy undergoes trapezoidal shape transition. And also, the diffusion coefficients of Cu in p type and n type Si substrates is different [70].

#### 3.3.2.4 Self Assembled Cu-Si Nanowires on p-Si(100)

Figures 3.15(a)-(d) show SEM micrographs of e-beam evaporation of Cu onto a $SiO_2$/Si-p(111)substrate at 600°C for 1,2,4 and 5 mins as in the previous case. The square, rectangle and nanowire shapes were the common islands on $SiO_2$/p-Si(100) substrates from the SEM images. Since the (100) plane exhibits four fold symmetry, the square shape reflects the four fold symmetry of the substrate. Orientations of the self assembled islands were found to be along [110] and $[\bar{1}10]$ as shown in Fig. 3.17(c) with 90° angle between the two nearest vectors.

The density and area of the $Cu_3Si$ islands deposited on $SiO_2$/p-Si(100) substrate from the SEM images are shown in closed and open squares in Fig. 3.16. As shown in Table 3.3, the density of the islands increases from 2.12 x $10^6$ $cm^{-2}$ to 25.5 x $10^6$ $cm^{-2}$ and decreases to 8.50x $10^6$ $cm^{-2}$. The mean area of the islands increases from 4.4 x $10^5$ $nm^2$ to 12.4 x $10^5$ $nm^2$ with deposition time at constant deposition

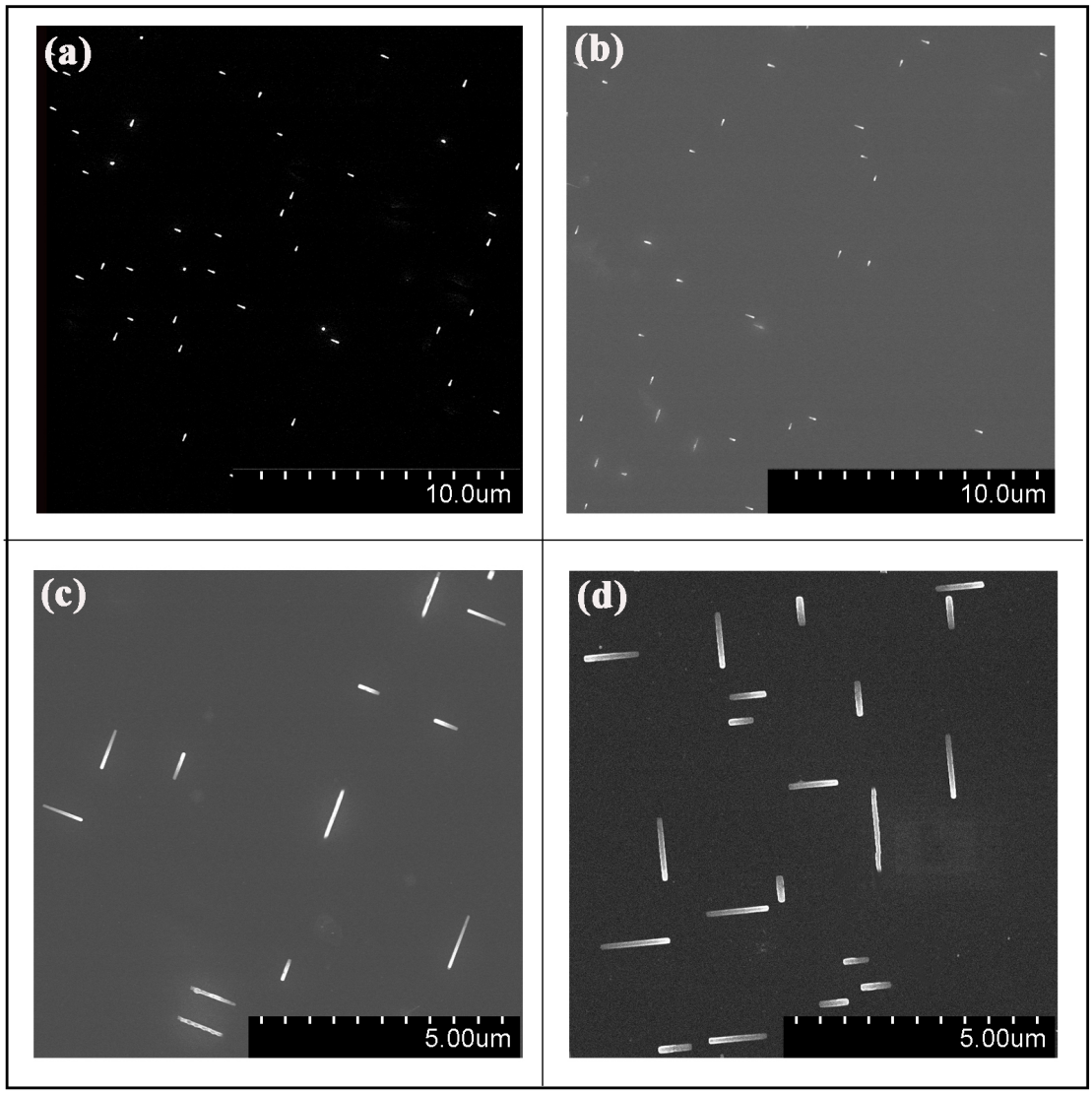


Figure 3.15: Cu deposited on $SiO_2$/Si-p(100) at 600°C for a deposition time of (a)1 min (b) 2 min (c) 4 min (d) 5 min.

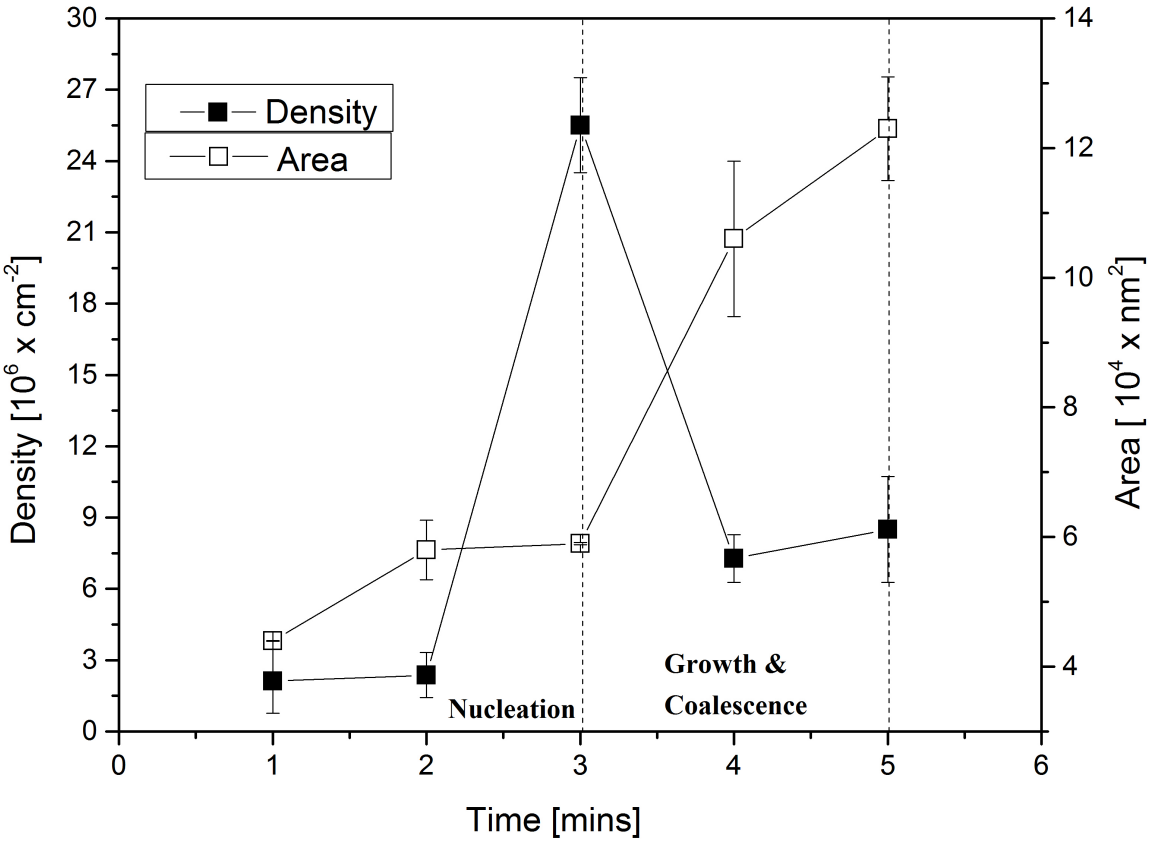


Figure 3.16: Growth kinetics of $Cu_3Si$ islands grown on $SiO_2$/p-Si(100) substrate at 600°C with deposition time.

temperature 600°C.

The kinetics of island nucleation exhibits similar behavior to that of the diffusion growth process shown in Fig. 1.2. The island nucleation density (N(t)) increases with time, eventually saturating at the value 2.55 x $10^7$ $cm^{-2}$. It can be inferred from Fig. 3.16, that N(t) increases with time up to 3 ML deposition before reaching a saturation value. With further deposition, N(t) decreases and the area of the islands increases. Once N(t) reaches the saturation value, the probability of atoms being captured by the existing islands is much higher compared to nucleation of new islands in order to achieve minimum surface energy. In the growth and coalescence

region shown in Fig. 3.16, it can be seen that the area of the islands increases from 5.9 x $10^5$ $nm^2$ to 12.4 x $10^5$ $nm^2$ with deposition time. The decrease in the density of islands (N(t)) from 2.55 x $10^7$ $cm^{-2}$ to 8.50x $10^6$ $cm^{-2}$ is due to coalescence, i.e. existing islands grow larger until they touch each other.

**Shape Transition:**

For the epitaxial island growth on p-Si(100) substrate, up to the critical size islands are of square shape above which the transition to wires occurs as shown in Fig. 3.17. According to the Tersoff model, below a critical size islands tend to posses stable and compact shape. In reality the islands may have complex shapes including squares, rounding and triangles depending on the material system. For the growth on p-Si(100), the observed shapes are squares reflecting the four fold symmetry of the substrate. On the first part of the curve in Fig. 3.17, growth is just beginning, and the shape of the island is square. The island remains a square up to L=W=$e\alpha_0$. At this critical size, shown as a dotted line in the Fig. 3.17(d), a shape transition to rectangular islands occurs. For the largest square island, the area is L x W = 4.4 x $10^4$ $nm^2$. The area of the island, where the shape transition takes place $e^2\alpha_0^2$= 4.4 x $10^4$ $nm^2$. This provides a critical size of e$\alpha_0$ = 210 nm, as shown in Fig. 3.17(d) with a dotted line. It is interesting to note that the critical sizes for the growth of $Cu_3Si$ islands on p-Si(111) and p-Si(100) are approximately the same. As the island area increases further, a transition to a rectangular shape occurs. These islands have been called self-assembling quasi-one-dimensional quantum wires [48].

From Fig. 3.17(d), it follows that for island lengths larger than 692 nm, L starts to increase much more rapidly while W decreases. As the area further increases the increase in length and slight decrease in the width lead to the formation of thin wires with a sharp increase in aspect ratio as predicted by the Tersoff model. We have observed aspect ratio as large as $\sim$ 20:1. Aspect ratios of nanowires grown on p-

| Substrate Dopant(Orientation) | Time min | Length (nm) | Width (nm) | Aspect Ratio | Area ( x $10^3$ $nm^2$) | Density (x $10^6$ $cm^{-2}$) |
|---|---|---|---|---|---|---|
| p(100) | 1 | 285.8 | 281.0 | 1:1 | 44.0 | 2.12 |
| p(100) | 2 | 692.5 | 90.5 | 7.7:1 | 58.5 | 2.37 |
| p(100) | 3 | 1214.6 | 60.6 | 20:1 | 68.2 | 25.5 |
| p(100) | 4 | 1324.8 | 88.5 | 15:1 | 106.2 | 7.28 |
| p(100) | 5 | 1401.9 | 94.7 | 15:1 | 123.7 | 8.5 |

Table 3.3: Dimensions of $Cu_3Si$ nanostructures grown on p-Si(100) substrates.

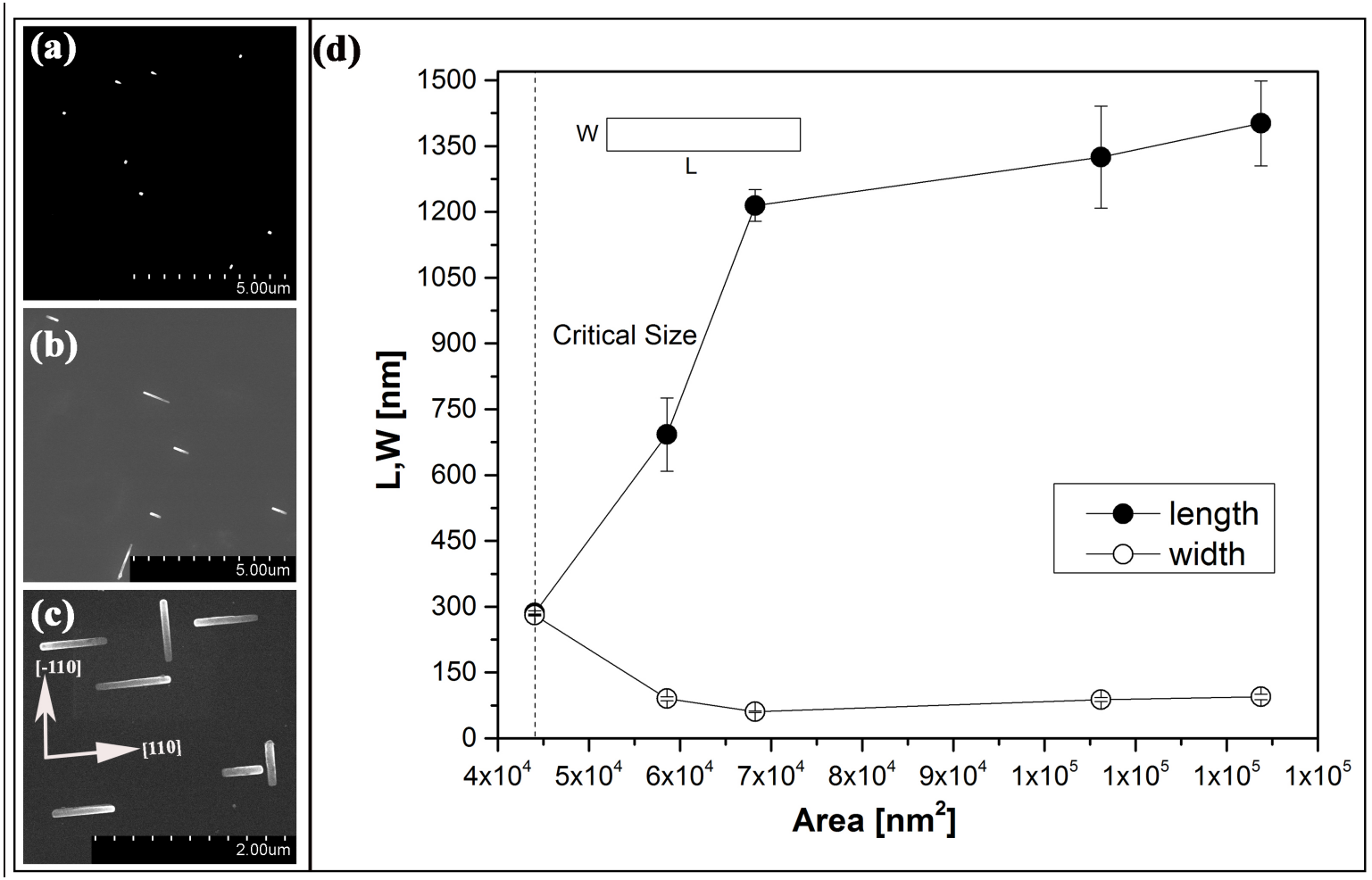


Figure 3.17: Three stages of $Cu_3Si$ island growth on p-Si(100) are shown as imaged using SEM. In (a) islands are square, until a shape transition to rectangular islands (b) rectangular islands (c) long wire shaped islands (d) dependence of both island length L( closed circles) and width W(open circles) on the island surface area.

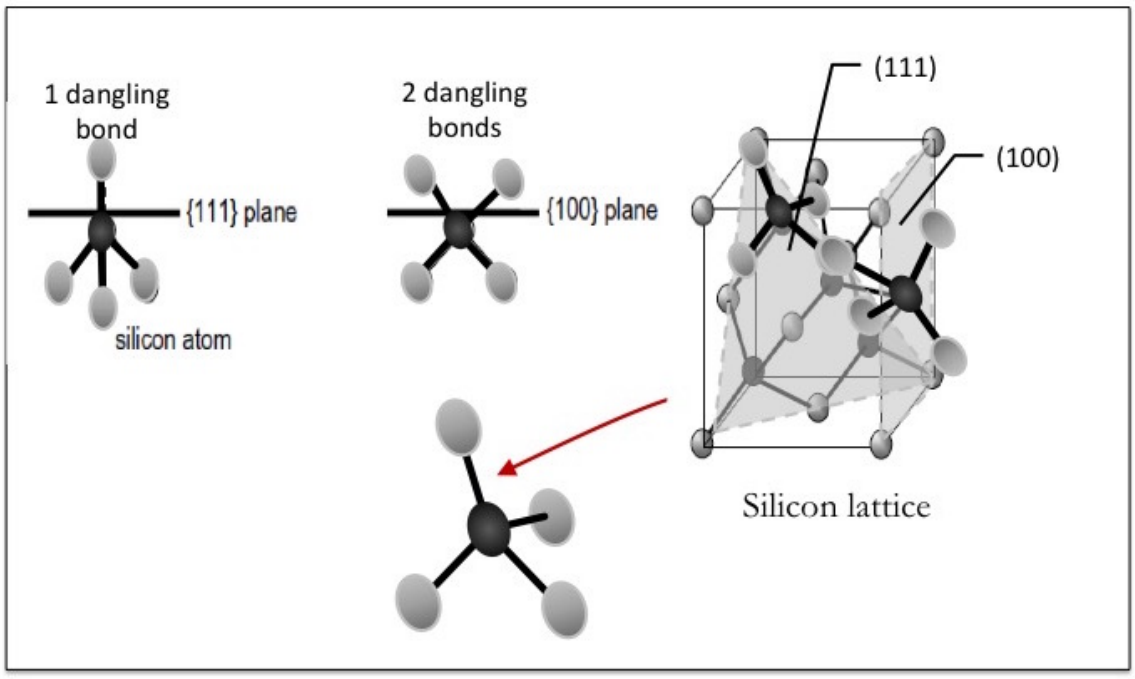


Figure 3.18: Dangling bonds on Si{111} and Si{100} planes. Figure adapted from[71].

Si(100) are $\sim$ 2.5 times that of the wires grown on p-Si(111) but they tend to exhibit similar growth morphology. The increase in length and decrease in W indicates the island is trying to minimize its energy. For the longer islands the width approaches towards the optimum value W $\simeq$ 94 nm. With further increase in the area, a linear increase in the length is predicted but the slight increase in the width is unexpected. This could be due to dislocations formed on the substrates at high deposition times. All these islands are oriented either along or perpendicular to the secondary flat, i.e along [110] and [$\bar{1}$10] directions without any preference as shown in Fig. 3.17(c).

**Lengths of $Cu_3Si$ nanowires : p-Si(111) vs p-Si(100)**

As shown in Table 3.4, the maximum lengths of the $Cu_3Si$ nanowires grown on p-Si(111) substrate is $\sim$ 2 times that of the $Cu_3Si$ nanowires grown on the p-Si(100) substrate. The possible factors that could have contributed to the observed differences in the lengths of nanowires are discussed here. One of the crucial steps in the growth

process of $Cu_3Si$ islands is the creation of voids at the interface and in the later stages these voids can act as nucleation sites and facilitate the growth of $Cu_3Si$ islands. The process of void formation at the $SiO_2$/Si interface is achieved by breaking the Si-O bonds present at the interface. As shown in Fig. 3.18, the Si{111}plane has only one dangling bond at the interface whereas the Si{100} plane has 2 dangling bonds at the interface [72–74]. In order to facilitate the void growth at the $SiO_2$/Si interface only one Si dangling bond needs to be broken on {111} plane whereas 2 dangling bonds needs to be broken on Si{100} plane. Also the activation energy needed for the void growth on the ultra thin oxide is $\sim$ 4 eV through thermal annealing process, which is considered to be a relatively slow process[75]. So, it is reasonable to assume the area of the voids created on both the Si planes, i.e,{111} and {100}, would not be the same because of the difference in the number of dangling bonds present at the interface. The time taken for the desorption of two Si-O bonds at the interface should be almost double that of time taken to break one bond under constant annealing conditions. Since the ratios of dangling bonds present at the interface of silicon {111} and {100} is 1:2, the maximum lengths of $Cu_3Si$ nanowires obtained are in the ratio of 2:1.

| Substrate Dopant(Orientation) | Length(L) Min - Max (nm) | Width(W) Min - Max (nm) | Aspect Ratio Max.(L/W:1) | Area Min - Max ( x $10^3$ $nm^2$) | Density Min - Max (x $10^6$ $cm^{-2}$) |
|---|---|---|---|---|---|
| n(111) | 682-986 | 682-1035 | — | 202-793 | 1.69-156 |
| p(111) | 282-2878 | 161-340 | 8.5:1 | 45-980 | 0.87-7.3 |
| p(100) | 286-1402 | 61-281 | 20:1 | 44-124 | 2.12-25.5 |

Table 3.4: Comparison of $Cu_3Si$ nanostructures dimensions grown on n-Si(111), p-Si(111) and p-si(100) substrates.

# Chapter 4

# Nanopatterning of Epitaxial $Cu_3Si$ Nanostructures on Silicon using HCI beams of Ar

## 4.1 Introduction

What are highly charged ions and what is the difference between singly charged and highly charged ions? Even though there is no definite answer, in general an ion possessing a charge of +2 or more is considered to be a highly/multiply charged ion (HCI). One major difference of these HCIs is that they can remove more than one electron when they interact with materials such as metals, insulators or polymers. In contrast to singly charged ions where the kinetic energy of the projectile constitutes the important parameter, potential energy plays a key role in the HCI surface interaction. HCIs posses large potential energies, which is the sum of the ionization energies of the removed electrons. This potential energy is liberated during the impact of the ions with a solid surface and can be deposited into a nanometer sized region on that

surface. For example, in $Xe^{44+}$ the potential energy amounts to about 51 keV and this energy is available for inducing a variety of inelastic processes at the surface.This large potential energy can induce radiation effects such as craters,voids and pits on the surface and can facilitate chemical reactions that require high temperatures [76].

In this chapter, the focus is on slow highly charged ion (SHCIs) interactions with oxides in the low energy regime. In the literature "slow" is defined as projectile velocities less than a Bohr velocity: $v_p < 2.19 \times 10^6$ m/s or kinetic energies less than 25 keV/u. In the present study the kinetic energies of the projectiles are $\leq 1$ keV. In this velocity regime, the timescale for electron motion is short compared to the timescale for ion motion. This provides time for above-surface electron capture and relaxation processes, and means that the ion will neutralize rapidly near the surface. This can result in ion-surface modifications with nanometer dimensions on various surfaces. In summary, the interaction of slow HCIs with surfaces can initiate processes which strongly depend on the kinetic and potential energy of the projectile ion as well as on the properties of the target surface [76]. This makes HCIs a promising tool for surface modification and characterization.

Traditionally, the growth process of $Cu_3Si$ nanostructures involves annealing of silicon substrates in UHV at high temperatures (600°C) for 10-12 hours[77, 78] followed by the deposition of Cu at 600°C. This is a two step growth process. Initial over night annealing facilitates the growth of voids at defect sites(stacking faults, etc.) while the integrity of the oxide layer is not disturbed in the defect-free regions. Secondly, Cu atoms at high temperature possess enough mobility to diffuse to the interface and react with Si to form the $Cu_3Si$ phase at defect sites.

In the present work, we examine an alternative mechanism for the study of and role of HCI induced sputtering yields on ultra thin oxide surfaces. The general procedure for measuring sputter yields involves placing time-of-flight(TOF) detectors

at a fixed angle and measuring yields of sputter atoms assuming the process to be isotropic. Our method involves irradiation of $SiO_2$/Si samples with $Ar^{q+}$ beams of varying charge state and dose and subsequently growing $Cu_3Si$ nanostructures at the defect sites created by the HCI irradiation. Measuring the yields of the thereafter grown $Cu_3S$ nanostructures provide insight into the sputter yields and their trends. This also eliminates the need to measure sputter yields during irradiation. The highly charged ion beams were produced in the CUEBIT laboratory using an EBIT at Clemson University. An overview of the EBIT and generation of multi-to highly charged ion beams are discussed in the next section.

## 4.2 Clemson University Electron Beam Ion Trap (CUEBIT)

The CUEBIT facility is located in the Kinard Laboratory of Physics on the main campus of Clemson University. Details of the CUEBIT experimental setup is mentioned elsewhere[79]. A schematic layout of the ion source (EBIS-SC) and beamline in the CUEBIT facility is shown in Fig. 4.1. Highly charged ions are produced in an electron beam ion souce (EBIS-SC) by successive electron impact ionization in a dense electron beam which is compressed by a high magnetic field. The schematic of the inner source setup is shown in Fig. 4.2. The EBIS source setup consists of a cathode, drift tube, superconducting magnet, electron collector and ion extraction region. The electron beam is formed from a cathode emitter and is directed to a drift tube that is surrounded by a 6 T superconducting magnet which compresses the electron beam. The drift tube consists of three sections with the possibility of biasing each region independently to confine(trap) the ionized species axially and

radially. The neutral gas that needs to be ionized is injected into the drift tube and the compressed electron beam collides with gas atoms in the center region of the drift tubes to ionize them.

Beams of HCIs can be generated either in pulsed more or leaky mode as shown in Fig. 4.3. Leaky mode involves setting the third region of the drift tube to low voltage such that ions can leak over the lower potential barrier continuously. Pulsed mode involves closing and opening the trap for fixed time intervals by lowering the potential in the third region of the drift tube. Since the ions are trapped for longer times in the pulsed mode it is expected to generate higher charge states. The highly charged ions exiting from the drift tube pass through the electron collector where the electrons are separated from the ions. Finally highly charged ions leave the source through the ion extraction system.

The highly charged ions that exit from the ion extraction system enter the CUEBIT beamline. The CUEBIT beamline consists of two vacuum sections (Sections I and II) shown in Fig. 4.1. In Section I are a 4- jaw slit system, quadrupole beam deflector and Faraday cup (FC 1). The HCI ions extracted from the ion source enter the 4- jaw slit system within Section I of beamline through the ion beam guiding components. The 4-jaw slit system allows one to reduce the beam diameter in front of the first Faraday cup (FC I). It is also used to determine the size and position of the beam. The ion beam exits from the 4-jaw slit system and enters pulses through the quadrupole beam deflector. First Faraday cup (FC 1) allows for the measurement of charged particle beam current and charges in real time. Section II of the beamline includes a dipole magnet that bends the beam at an angle of 90°C and provides HCI charge state selection. The second Faraday cup (FC 2) is used to record the selected HCI beam after it exits the magnetic region. An example spectrum from FC 2 is shown in Fig. 4.3 both in leaky and pulsed mode. Finally HCI beam is decelerated

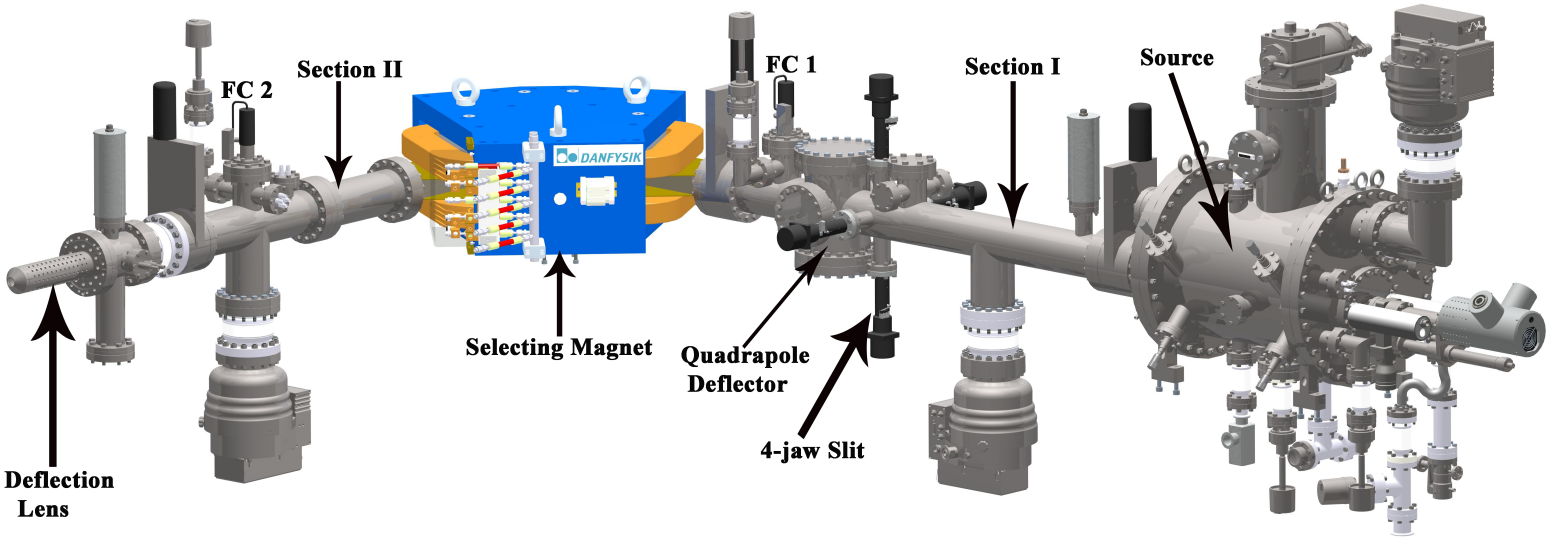


Figure 4.1: Schematic layout of the ion source (EBIS-SC) and beamline in the CUEBIT facility. Figure adapted from [80].

using a deceleration lens before entering the target chamber.

### 4.2.1 Target Chamber

Extracted HCI beams enter the target chamber of CUEBIT which acts as a delivery point as shown in Fig. 4.4. The target chamber consist of a load-lockable chamber, gate valve, magnetic linear translator, sample mount, manipulator or linear translator, and Faraday cup. The target chamber is configured with turbo pumps to maintain UHV. Samples are mounted on an Omicron style sample platen and load-locked into the target chamber. The sample can be translated with the help of a linear translator into the beam path. The final beam current and dose is determined using a Faraday cup(FC 2).

## 4.3 HCI - Surface Interactions

Ion surface interactions play an important role both as fundamental science and in the microelectronics technology. When an ion hits the surface of a material, it can initiate several different processes depending on the charge species, kinetic energy, potential energy, target surface and the geometry. In order to explore applications for ions, it is necessary to understand their underlying physical interaction mechanisms in detail. Ion surface interactions with metals and semiconductors are of particular interest to the microelectronics industry given their applications in ion implant and dry and plasma etching in the fabrication of integrated circuits.

In this thesis, the focus for studying ion-surface interactions is on highly charged ion (HCI) interactions with ultra thin insulators(oxide) and polycarbonate (PC, Lexan) in the low energy regime where the kinetic energies of the projectiles are $\leq$ 1 keV. In the literature "slow" is defined as projectile velocities less than the

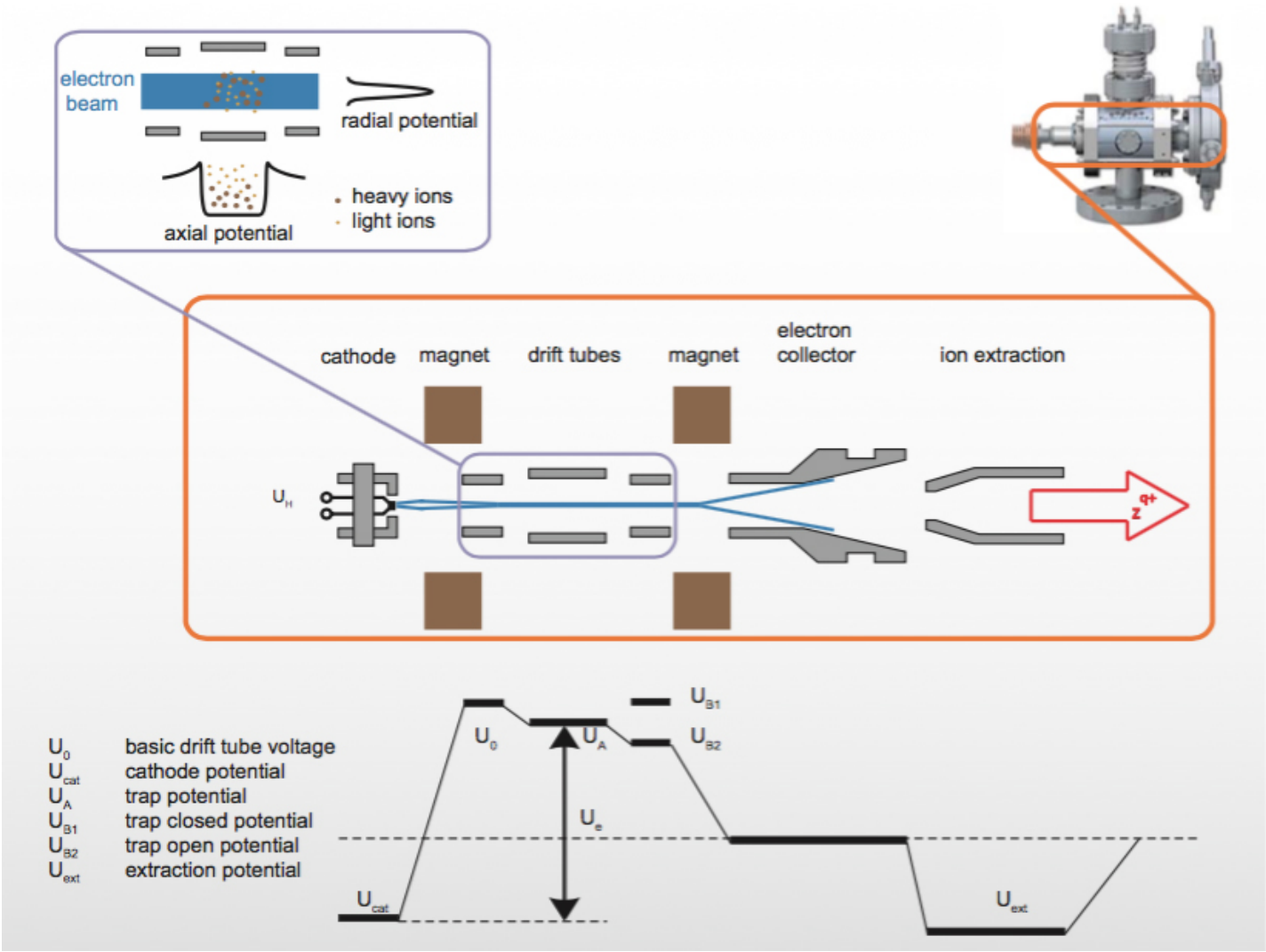


Figure 4.2: The principal scheme of the inner source setup for the ion souce operation. Figure adapted from [80].

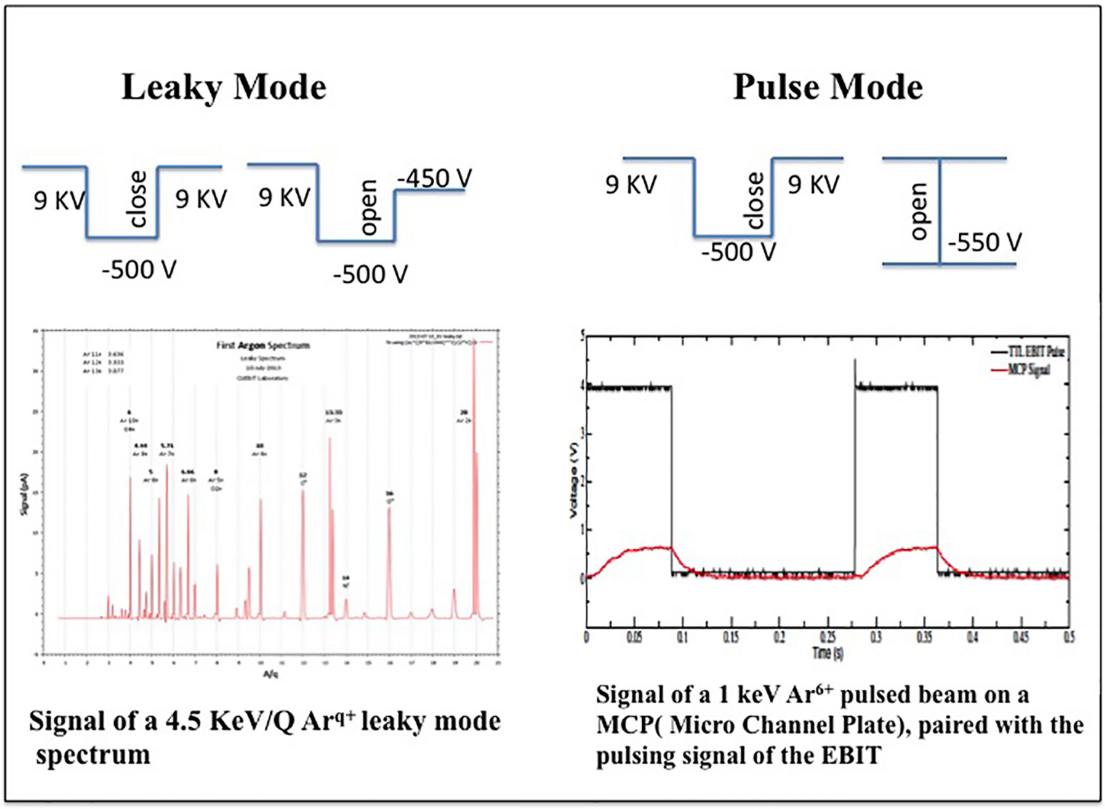


Figure 4.3: Leaky mode and pulsed mode beam generation.

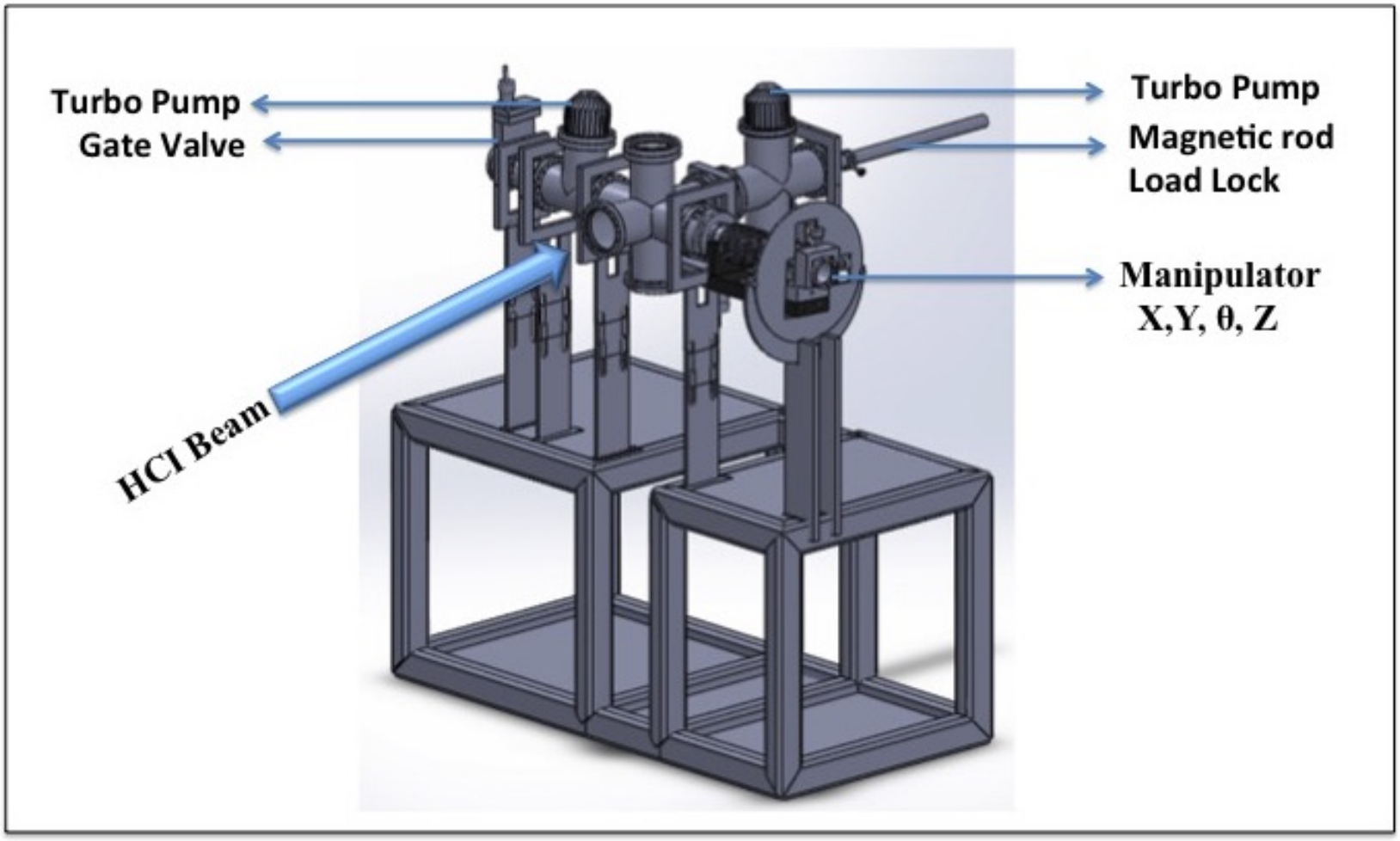


Figure 4.4: Schematic layout of CUEBIT target chamber.

Bohr velocity: $v_p < 2.19 \times 10^6$ m/s or kinetic energies less than 25 keV/u. Such a slow electron interaction with a surface can be distinguished into two phases: the "above-surface" phase is dominated by hollow atom formation and decay and the "below-surface" phase is where the combined effects of potential and kinetic energies takes place. The formation of hollow atoms and ions when an ion approaches a surface is clearly understood from above-surface interaction studies but the neutralization and relaxation mechanisms that govern below-surface effects are less understood because the interaction is complex and depends on the ions potential energy, kinetic energy, charge state and the surface morphology.

HCIs can be characterized by two parameters; the charge state 'q', and the potential energy ($E_q$), which is the energy released when the HCI is neutralized. $E_q$ depends on q and the charged species. A general scenario of the interaction of a slow HCI with a metal is shown in Fig. 4.5. With the approach of the slow HCI the surface is polarized, an "image charge" is formed, and the ion induces a dielectric response in the target. The HCI is accelerated by its own image charge towards the surface and gains additional kinetic energy(Stage A). At a distance $R_c$ above the surface, where the potential barrier between the HCI and the surface drops below the Fermi level of the solid, the ion starts to capture electrons from the surface into ion higher levels (Rydberg states). This capture process continues until the ion is fully neutralized and so a "hollow atom " of first generation (HA1) is formed (Stage B). A hollow atom is defined as one with many electrons in the higher orbitals and empty intermediate shells. The critical distance $R_c$, where the first electron transfer takes place via the classical over barrier (COB) mechanism is given by

$$R_c \approx \frac{\sqrt{2q}}{W} \tag{4.1}$$

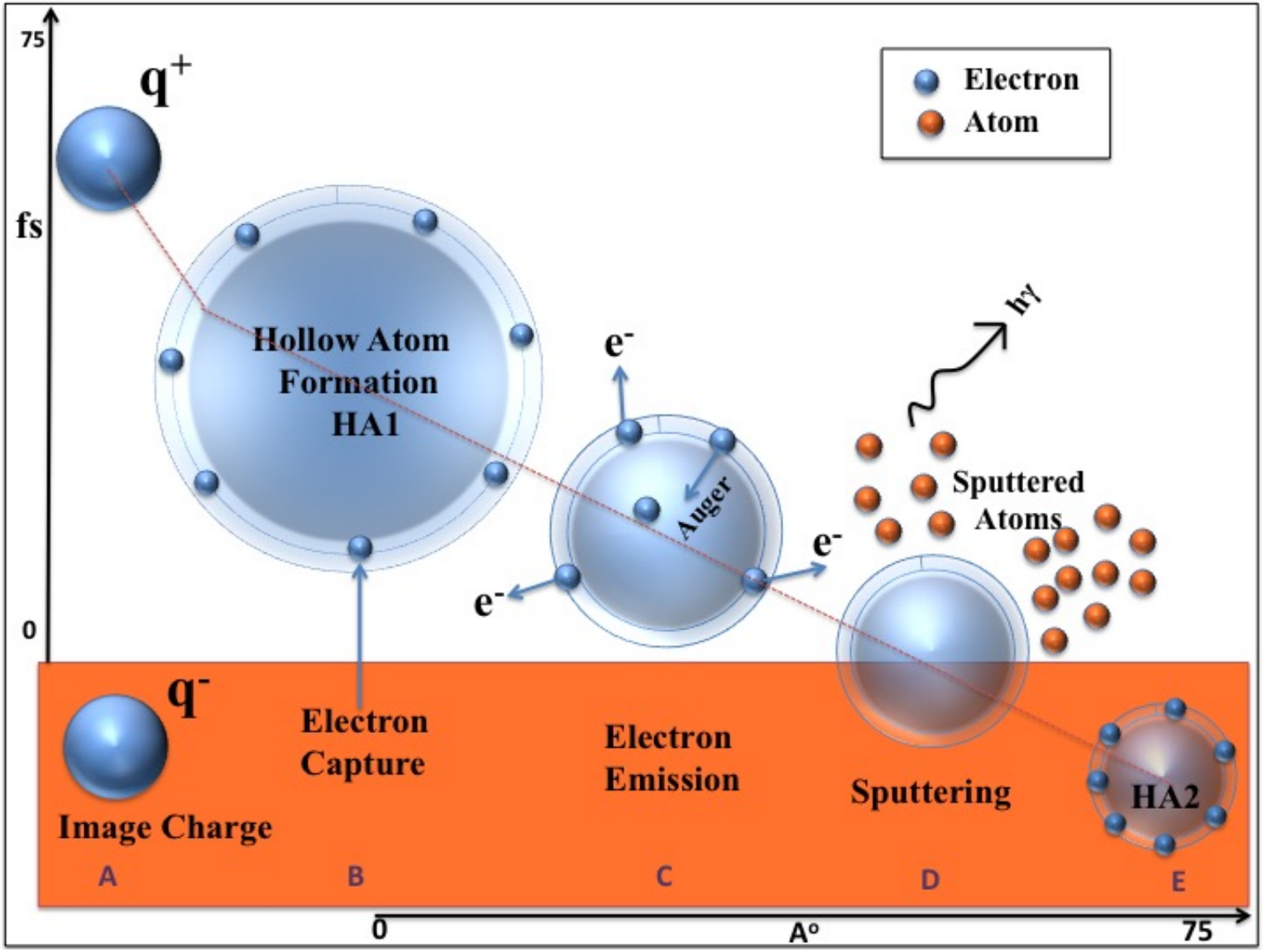


Figure 4.5: Schematic representation of slow HCI impact on a surface.

Where $q$ is the charge state of the ion and $W$ is the work function of the surface.

The hollow atom electrons in the Rydberg states are not stable. Hollow atoms will reduce in size by dielectronic processes such as autoinoization(AI), inter-atomic Auger electron emission and also Rydberg electrons will relax to fill lower states by resonant electron transfers to the solid (Stage C). Upon impact of the hollow atom onto the surface the electrons in the high states (Rydberg electrons) are stripped off(Stage D). Simultaneously, the ion passes into the surface releasing all its potential energy ($E_q$) through emission of Auger electrons and X-rays. Below the surface, the HCI strongly attracts several electrons from the conduction band (in metals) into higher orbits. This gives rise to a hollow atom of the second generation (HA 2) whose dimensions are much smaller than the one formed outside the surface (Stage E).

**Insulators and Poor Conductors:**

For insulators and poor conductors, the charge neutralization cannot be reestablished on the timescale of lattice vibrations. The target particles are exploded due to mutual electrostatic Coulomb repulsion that can be equivalent to the potential energy carried by the ion. This process leads to potential energy induced sputtering and the formation of permanent material defects.

### 4.3.1 Classical Over Barrier Mechanism (COB)

When the potential barrier between the HCI and the surface drops below the Fermi level of the solid, the ion captures electrons classically over the barrier from the surface into electronic levels of the ions. This is known as classical over barrier (COB) condition. The transition rate in COB is much higher than tunneling or resonant capture processes. The COB model is used to estimate at what distance an ions first electron capture happens and from where in the solid it is being captured from. The

"active electron" to be transferred from the surface to the ion is subjected to several well-defined interactions. The interaction potential V(z) of the active electron in the region between the ion and surface is the sum of the three potentials $V_{p,e}$, $V_e^{im}$ and $V_{p,e}^{im}$ and is given by [81–83]

$$V(z) = V_e^{im}(\mathbf{r}) + V_{p,e}(\mathbf{r}, \mathbf{R}) + V_{p,e}^{im}(\mathbf{r}, \mathbf{R}) \tag{4.2}$$

where $V_{p,e}$ is the attraction between the electron and the ion, $V_e^{im}$ is the attraction between the electron and its self-image, $V_{p,e}^{im}$ is the repulsion between the electron and the target dielectric response (image charge) induced by the ion. Expressions for these three are given by

$$V_{p,e}(\mathbf{r}, \mathbf{R}) = -\frac{q}{|\mathbf{r} - \mathbf{R}|} \tag{4.3}$$

$$V_{p,e}^{im}(\mathbf{r}, \mathbf{R}) = \frac{\beta q}{|\mathbf{r} + \mathbf{R}|} \tag{4.4}$$

$$V_e^{im}(\mathbf{r}) = -\frac{\beta}{4z}. \tag{4.5}$$

Where $\mathbf{r}$ and $\mathbf{R}$ are the position vectors for the test charge and ion, respectively and $\beta$ is the permitivity of the surface or target material.

From Equations 4.2 - 4.5 the critical distance $R_C$, where the first electron transfer takes place via the COB mechanism is given by

$$R_C \approx \frac{\sqrt{2q\epsilon(\epsilon - 1)}}{W(\epsilon + 1)} + \frac{\epsilon - 1}{4W(\epsilon + 1)\epsilon}. \tag{4.6}$$

$R_C$ has an approximate square root dependence on charge state and an inverse dependence on $W$ where $W$ is the workfunction of the target. This $R_C$ in the limiting case of a metal ($\beta \to 1$) can be expressed in the classical over the barrier model(in atomic units) as

$$R_C \approx \frac{\sqrt{2q}}{W} \tag{4.7}$$

The HCI ion-surface interaction volume can be modeled by a sphere centered around the HCI with radius $R_C$. While $R_C$ is dependent on the dielectric permittivity (Eq. 4.6) of the target material, it is instructive to investigate the effect of the volume of interaction of the HCI with the target approximating the target as a metal for a first order calculation. As the HCI approaches the surface, the interaction effectively begins when the ion is at the distance of $R_C$. In this case, the region of the surface interacting with the ion is only a single point. The area of interaction at a time $t$ after the ion-surface distance is smaller than $R_c$ is then given by

$$A_{eff} = \pi(2R_c vt - v^2t^2) \tag{4.8}$$

As the sphere passes the plane of the target, the area of interaction with the surface increases until it reaches a maximum, when the HCI has reached the surface, and then decreases again as the HCI passes into the surface. The maximum area of interaction, when the HCI has reached the surface, occurs $\sim$ 10fs from the beginning of its interaction with the surface for the parameters used here. As can be seen, for a fixed kinetic energy, the maximum area of interaction is a circle with radius $R_c$, and $R_c$ depends on $\sqrt{q}$, leading to a linear dependence of the maximum area of interaction with the charge state $q$.

## 4.4 Fabrication of Epitaxial $Cu_3Si$ Nanostructures using HCI beams

In the previous chapter, the growth kinetics of epitaxial $Cu_3Si$ nanostructures using reactive deposition epitaxy (RDE) method was discussed. Traditionally, the RDE growth process of $Cu_3Si$ nanostructures involves annealing of the silicon sub-

strate in UHV at a high temperature of 600°C for 10-12 hours[77, 78] followed by deposition of Cu thin film at ∼600°C. This growth is an inherently two step process that can take approximately 20-24 hrs to complete, which may not be desirable for practical applications.

In the present work, we have taken a different route to enhance the throughput (density) and also reduce the time scale of the $Cu_3Si$ nanostructure growth process to less than 10 hours. Both of these objectives were met by pre-irradiating our $SiO_2$/Si substrates with highly charged ion beams of $Ar^{q+}$ (q=1,4,8) of varying fluences and kinetic energies, followed by the subsequent deposition of Cu at 600°C.

### 4.4.1 Fabrication Procedure

Single crystal, 3-inch diameter, boron doped p type silicon wafers of (111) and (100) orientations with resistivities of 1-10 Ω cm were employed as substrates for this study. Prior to the oxide growth, the wafers were cleaned following standard RCA clean, which involves cleaning of the substrates in a chemical bath (1:1:5 solution of $NH_4OH$ + $H_2O_2$+$H_2O$) for five minutes under ultrasonic agitation. This is followed by etching of cleaned surface with 1% dilute HF for two minutes and triple rinse in deionized water for six minutes to remove any native oxide. Following this cleaning, an ultra thin thermal oxide layer of approximately 1.5 ± 0.05 nm was grown via dry oxidation of Si at 200°C for 2 hours in a hot furnace. Oxide thickness measurements were performed at five different locations on each wafer (center and 4 corners) using a Sopra model GES-5E spectroscopic ellipsometer. The oxide grown Si wafers were diced into 10 mm × 10 mm squares and mounted on Omicron style samples platen and loaded into the target chamber of the EBIT. These samples were exposed to the focused highly charged ion beams produced in the CUEBIT laboratory. Details of

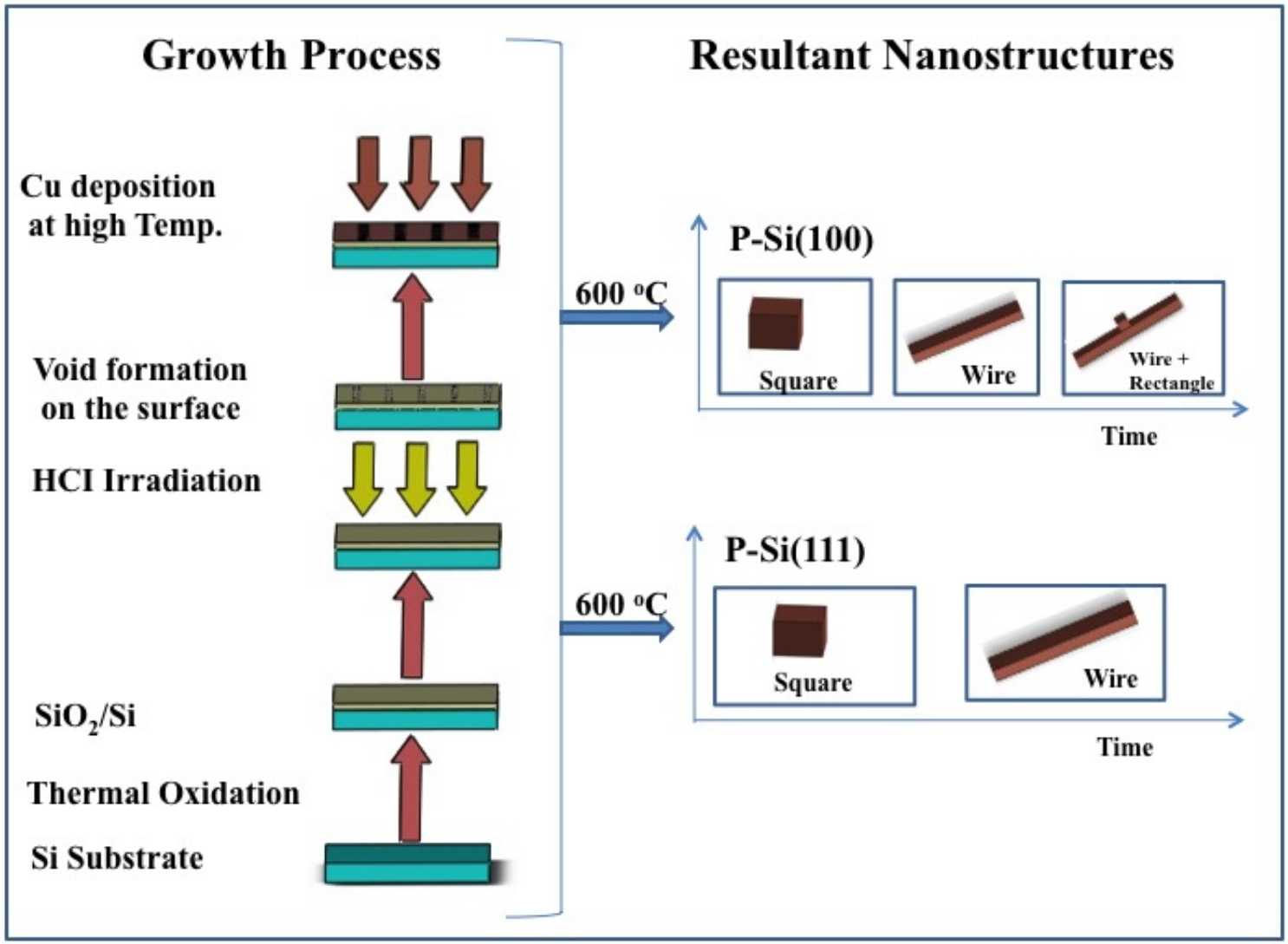


Figure 4.6: Growth Process of HCI assisted $Cu_3Si$ islands and resultant nanostructures.

the CUEBIT experimental setup are discussed in Section 4.2 and elsewhere[79]. The pressure inside the target chamber during the irradiations was on the order of $10^{-8}$ mbar and the ion doses were in the range of $10^{11}$ -$10^{12}$ per $cm^2$. The ion species used for the irradiations were $Ar^{1+}$, $Ar^{4+}$ and $Ar^{8+}$ with potential energies of 15.8 eV, 143.9 eV and 577.7 eV respectively. The kinetic energies of all the ion beams was 1 keV. After irradiation the samples were unloaded from the target chamber and transferred to a deposition chamber. Thin Cu films were deposited on these irradiated samples at temperature of 600°C using a Mcallister Ebeam Evaporator (EVAP) at a pressure of $5 \times 10^{-6}$ Torr. The deposition was kept to a 0.1 mA flux current and a deposition time of 5 min. The deposition rate was estimated to be 1 ML/min. The sequence of steps involved in the growth process of the resulting $Cu_3Si$ nanostructures are shown in Fig. 4.6.

### 4.4.2 HCI fluences and specifications

As noted above, prior to the copper deposition our $SiO_2$/Si substrates of (111) and (100) orientations were irradiated with HCI beams of Ar. This step was intended to create defect sites (voids) on the surface of the oxide which could act as nucleation centers for the growth of $Cu_3Si$ nanostructures. The charge species, beam current, irradiation fluence and time of irradiations are shown in Table 4.1.

## 4.5 SEM Results and Discussion

As shown in Fig. 4.6, the $SiO_2$/Si substrates were irradiated with varying charge states and doses of slow HCI Ar beams prior to the deposition of Cu. When such an HCI approaches a surface, the potential energy will be deposited into a nanometer sized region on the surface and will be responsible for the formation of

| Substrate (Si) | Charge Species (Ar) | Potential Energy (eV) | Current (pA) | Fluences ($cm^{-2}$) | Time (min) | Shape |
|---|---|---|---|---|---|---|
| p(100) | $Ar^{1+}$ | 15.8 | 178 | 5 x $10^{12}$ | 75 | wire |
| p(100) | $Ar^{4+}$ | 143.9 | 1870 | 1 x $10^{11}$ | 0.57 | square |
| | $Ar^{4+}$ | 143.9 | 1870 | 1 x $10^{12}$ | 5.7 | square |
| | $Ar^{4+}$ | 143.9 | 1870 | 2.5 x $10^{12}$ | 14.27 | square |
| | $Ar^{4+}$ | 143.9 | 1870 | 5 x $10^{12}$ | 65 | wire+square |
| p(100) | $Ar^{8+}$ | 577.7 | 950 | 1 x $10^{11}$ | 2.25 | wire |
| | $Ar^{8+}$ | 577.7 | 950 | 1 x $10^{12}$ | 22.5 | wire |
| | $Ar^{8+}$ | 577.7 | 950 | 2.5 x $10^{12}$ | 56 | wire+square |
| | $Ar^{8+}$ | 577.7 | 838 | 5 x $10^{12}$ | 127.3 | wire+square |
| p(111) | $Ar^{1+}$ | 15.8 | 211 | 5 x $10^{12}$ | 64 | square |
| | $Ar^{4+}$ | 143.9 | 2322 | 2.5 x $10^{12}$ | 11.5 | square |
| | $Ar^{4+}$ | 143.9 | 2322 | 5 x $10^{12}$ | 23 | wire |
| | $Ar^{8+}$ | 577.7 | 546 | 5 x $10^{12}$ | 195.17 | square |

Table 4.1: HCI irradiation specifications of $SiO_2$/Si substrates.

nanofeatures such as voids, craters etc. This process of removing material from the surface without producing radiation effects in the deeper layers is known as soft sputtering. From previous studies, it is evident that "potential sputtering" is responsible for the formation of charge-depleted regions(voids,pits etc) on surfaces due to multiple electron transfers from a target to an approaching HCI [84]. The general approach to probe HCI-induced surface effects is to irradiate the substrate with HCIs and subsequently probe the surface topography with imaging tools such as transmission electron microscope(TEM), atomic force microscope(AFM) or quartz crystal monitor(QCM). However, analysis of HCI induced defects has been quite difficult, primarily due to limitations associated with the resolving power of the imaging tools. In the present work we can probe HCI-induced sputtering and possibly overcome such imaging challenges, as we deposit Cu on HCI irradiated and measured the yields of the subsequently formed $Cu_3Si$ nanostructures.

### 4.5.1 Self Assembled Cu-Si Nanowires Growth on p-Si(100)

From our previous work, it is known that the optimum temperature required to facilitate the reaction between Cu and Si and form $Cu_3Si$ nanostructures is about 600 °C. A Cu thin film was deposited using the electron beam evaporation technique for 5 mins at 600°C maintaining a constant growth rate of 1 ML/min. The SEM images revealed a variation in the density and shape of $Cu_3Si$ nanostructures at the sample surfaces (p-Si(100)) which can be seen from the SEM images shown in Fig.4.7. The primary growth mode is considered to be Volmer-Weber (VM) since areas of uncovered substrate coexisted along with 3D nanostructures and also the absence of a wetting layer when the deposition thickness is as low as 1 ML [27].

The observed shapes of $Cu_3Si$ nanostructures grown on the p(100) substrate

with $Ar^{q+}$-HCI irradiation (1 < q < 4) and for low doses ( 1 x $10^{11}$ $cm^{-2}$ < Dose < 2.5 x $10^{11}$ $cm^{-2}$ ) are squares reflecting the four fold symmetry of the substrate. With higher dose (> 2.5 x $10^{12}$ $cm^{-2}$ )HCI irradiation for the charge state q=1, 4, a change in the shape from square to nanowire was observed. No square shaped nanostructures were observed with $Ar^{8+}$-HCI irradiation even with the dose as low as 1 x $10^{11}$ $cm^{-2}$. The observed shapes were either nanowire or combination of nanowire and rectangular islands. In the latter case the rectangular islands are observed to be present on the top of nanowires and positioned approximately at the center. Orientations of the nanowires were found to be along [-110] and [110] without any preference. From Fig. 4.7, it is evident that the shape of the nanostructures depends on both the charge state (potential energy) and dose. Cross sectional HRTEM will be required to determine whether these nanowires exhibit endotaxy. Phase investigations from previous researchers has concluded that $Cu_3Si$ exhibits endotaxy both on Si(111) and Si(100) substrates [69, 85, 86]. It is interesting to note that self-assembled gaps with nanometer dimensions are formed, as show in Fig. 4.7. The probable mechanism responsible for the observed shape transition will be discussed later in the light of the strain driven shape transition model proposed by Tersoff and Tromp[48].

Fig. 4.8 shows the density dependence on the fluence for different $Ar^{q+}$ charge states. The linear dependence indicates that the density of $Cu_3Si$ nanostructures grown on the $SiO_2$/p-Si(100) substrate is linear within the given fluence range. For the $SiO_2$/Si(100) substrate irradiated with $Ar^{4+}$, the density of $Cu_3Si$ islands increases from 1 x $10^6$ $cm^{-2}$ to 8 x $10^6$ $cm^{-2}$ within an dose range of 1 x $10^{11}$ $cm^{-2}$ - 2.5 x $10^{12}$ $cm^{-2}$. However, for the higher q-HCI irradiation $Ar^{8+}$, the density increased from 1 x $10^6$ $cm^{-2}$ to 13.5 x $10^6$ $cm^{-2}$ within the same dose range. We also performed an irradiation with a singly charged ion $Ar^{1+}$ at an ion dose of 2.5 x $10^{12}$ $cm^{-2}$, where any ion effects should be due to kinetic sputtering only. The remarkable feature is

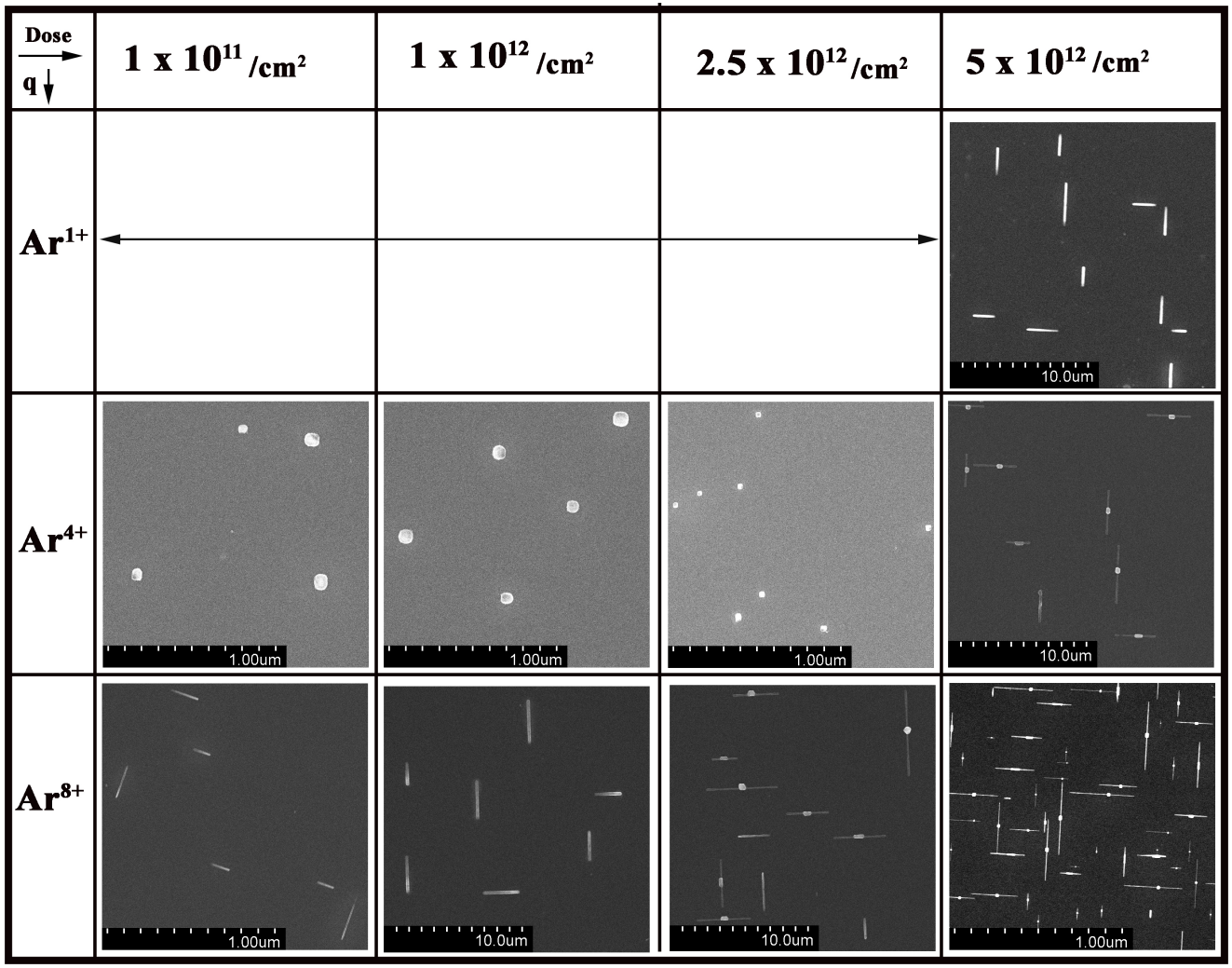


Figure 4.7: Cu deposited at 600°C on HCI irradiated $SiO_2$/Si(100) substrates of varying dose and charge state.

the strong q-HCI dependent $Cu_3Si$ growth, showing that q and density dependence are in the ratio of 1:4:8 to 1:2.5:4. The significant increase in the density of $Cu_3Si$ island formation by a high q HCI impact could be due to the formation of charged-up regions on the surface by removal of multiple electrons from the target and their transfer to the approaching ion. It is known that an HCI is neutralized very fast ($<$ 10 fs) in a solid. Therefore the potential energy of an HCI is released very near to the surface. The higher the charge state of an ion, the larger the effect it induces on the surface during interaction. The enhancement of the density at higher potential energies and charge states, suggests a process resulting from a Coulomb explosion [87, 88]. Masahide Tona et.al also observed a high increase in the sputtered yield of $O^+$ ions with $I^{q+}$ (q=15,40) ions impact on a native $SiO_2$/Si(111) target. They observed presence of $O^{2+}$ and $Si^+$ ion sputter yields at high charge state irradiations. There the high efficiency of positive ion emission by a high q HCI impact was discussed in the context of a Coulomb explosion model [89].

The slope of the lines from Fig. 4.8 can be used to calculate the feature density per ion. The density per ion graph demonstrates that for $Ar^{q+}$ the charge state dependence is linear as shown in Fig. 4.9. The density per ion of $Cu_3Si$ nanostructures due to $Ar^{1+}$ ions can be considered a kinetic effect and also serves as reference for comparison. By fitting we obtained a power law relationship (density $\sim q^{\gamma}$) for the density of $Cu_3Si$ nanostructures due to $Ar^{q+}$-HCI irradiation. As expected, $\gamma \sim 0.95 \pm 0.04$ for $Ar^{q+}$ irradiations on $SiO_2$/Si(100) target. According to the Coulomb explosion model [87, 89] proposed by Masahide Tona et.al, the relation between the sputter yield of positive ions ($Y_p$) and potential energy of HCI ($E_p$) was determined to be $Y_p \propto E_p^{\gamma}$, where $\gamma$ was found to be 0.6 for the sputter yields of $O^+$ ions for $I^{q+}$ HCI ion impacts on native $SiO_2$/Si(111) targets. The higher $\gamma$ obtained in our result could be attributed to the better quality of the oxide, as a thermally grown

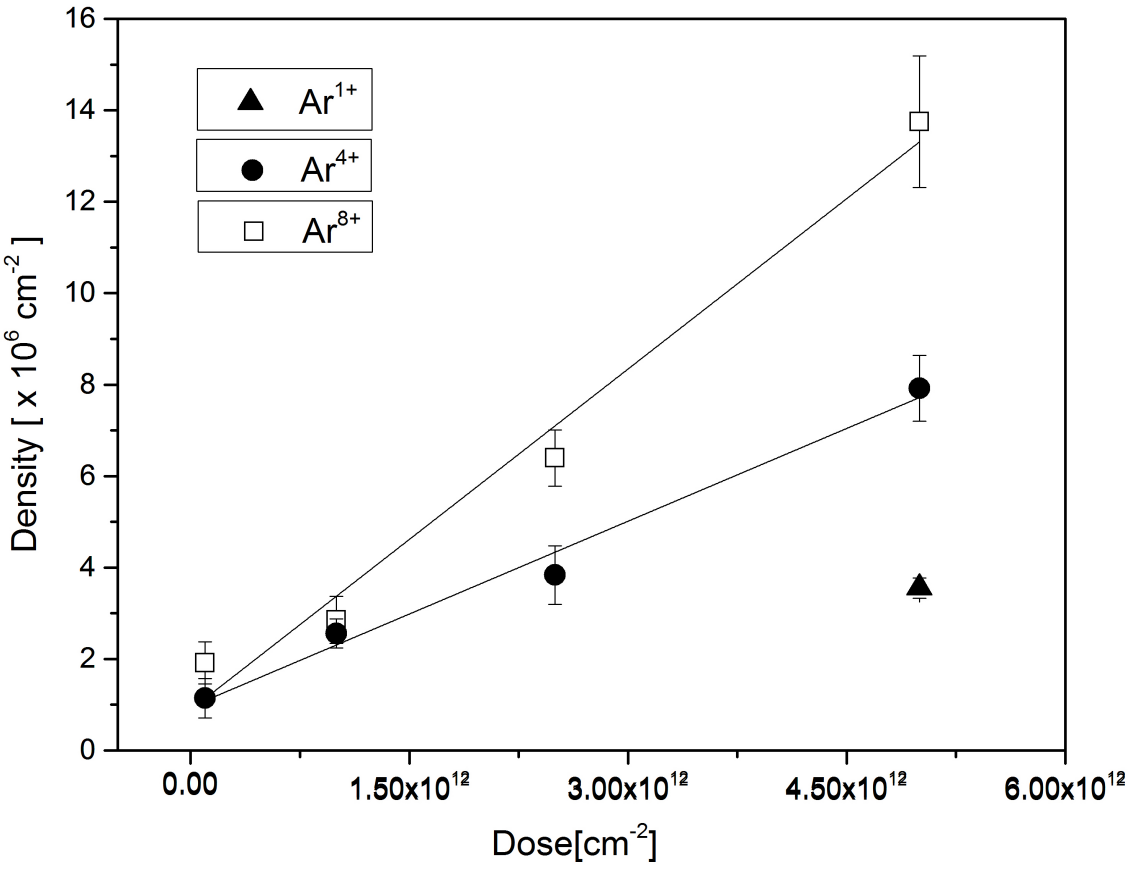


Figure 4.8: Average density of $Cu_3Si$ nanostructures versus dose on Si-p(100) substrates irradiated with $Ar^{q+}$ ions for charge state q=1,4,8.

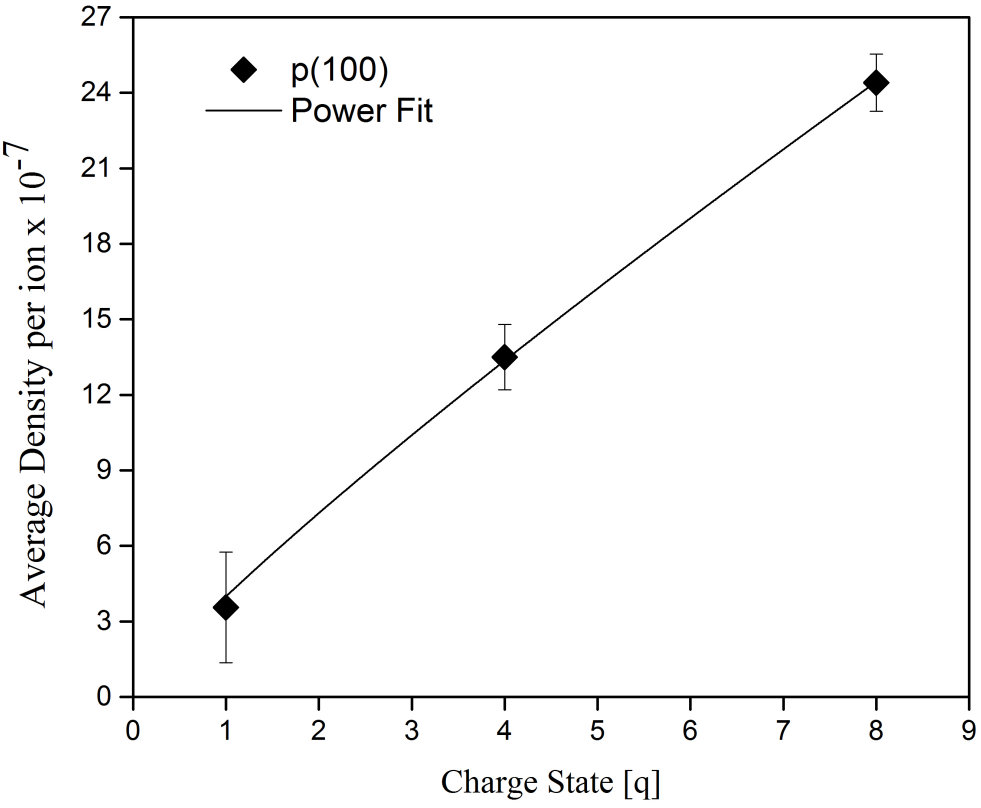


Figure 4.9: Normalized density per ion of $Cu_3Si$ nanostructures on Si-p(100) substrate obtained from dose dependent graph shown in Fig. 4.8 for $Ar^{q+}$ charge state (q=1,4,8).

$SiO_2$ oxide layer with thickness of 1.5 ± 0.05 nm was used. The comparison between the HCI induced defects on $SiO_2$/Si and $\gamma$ determined from thereafter grown $Cu_3Si$ nanostructures may not be in proportion but it may provide a path to understand HCI induced radiation effects, which is not possible otherwise.

**Shape Transition:**

For the epitaxial island growth on the Si-p(100) substrate irradiated with $Ar^{q+}$ ($1 < q < 4$) ions, we find that up to a critical size islands are square in shape above which they transition to wires as shown in Fig. 4.10. According to the Tersoff model,

below a critical size islands tend to posses a stable and compact shape. In reality the islands may have a complex shape including squares, rounding or triangles depending on the material system. For the growth on Si(100), the observed shapes are squares which reflects the four- fold symmetry of the substrate. On the first part of the curve in Fig. 4.10, growth is just beginning, and the shape of the island is square. The island remains a square up to L=W= $e\alpha_0$. At this critical size, shown as dotted line in Fig. 4.10(d), the shape transition to rectangular islands occurs. A sharp increase in length and a reduction in the width of the island occurs to minimize the energy of the island. For the largest square island, the area is L x W = 2.06 x $10^5$ $nm^2$. This provides a critical size ($e\alpha_0$) = 453.6 nm, as shown in Fig. 4.10(d) with a dotted line. As the island area increases further, a transition to a rectangular shape occurs.These islands have been called self-assembling quasi-one-dimensional quantum wires [48]. From Fig. 3(d), it follows that for island lengths larger than 492 nm, L starts to increase much more rapidly while W decreases. As the area further increases the increase in length and decrease in the width lead to the formation of thin wires with a sharp increase in aspect ratio as predicted by the Tersoff model. We have observed aspect ratio as large as $\sim$ 23:1. The increase in length and decrease in W indicates the island is trying to minimize its energy. For the longer islands the width approaches the optimum value W $\simeq$ 166.9 nm. For further increases in the area, a linear increase in length and a decrease in the width is predicted by the model. All islands are oriented either along or perpendicular to the secondary flat, i.e along [110] and [$\bar{1}$10] directions without any preference as shown in Fig. 4.10(c).

**RDE vs HCI assisted Growth Mode:**

The dimensions of $Cu_3Si$ islands grown on our p-Si(100) substrates via RDE vs. HCI assisted growth modes are shown in Table 4.2. The maximum lengths

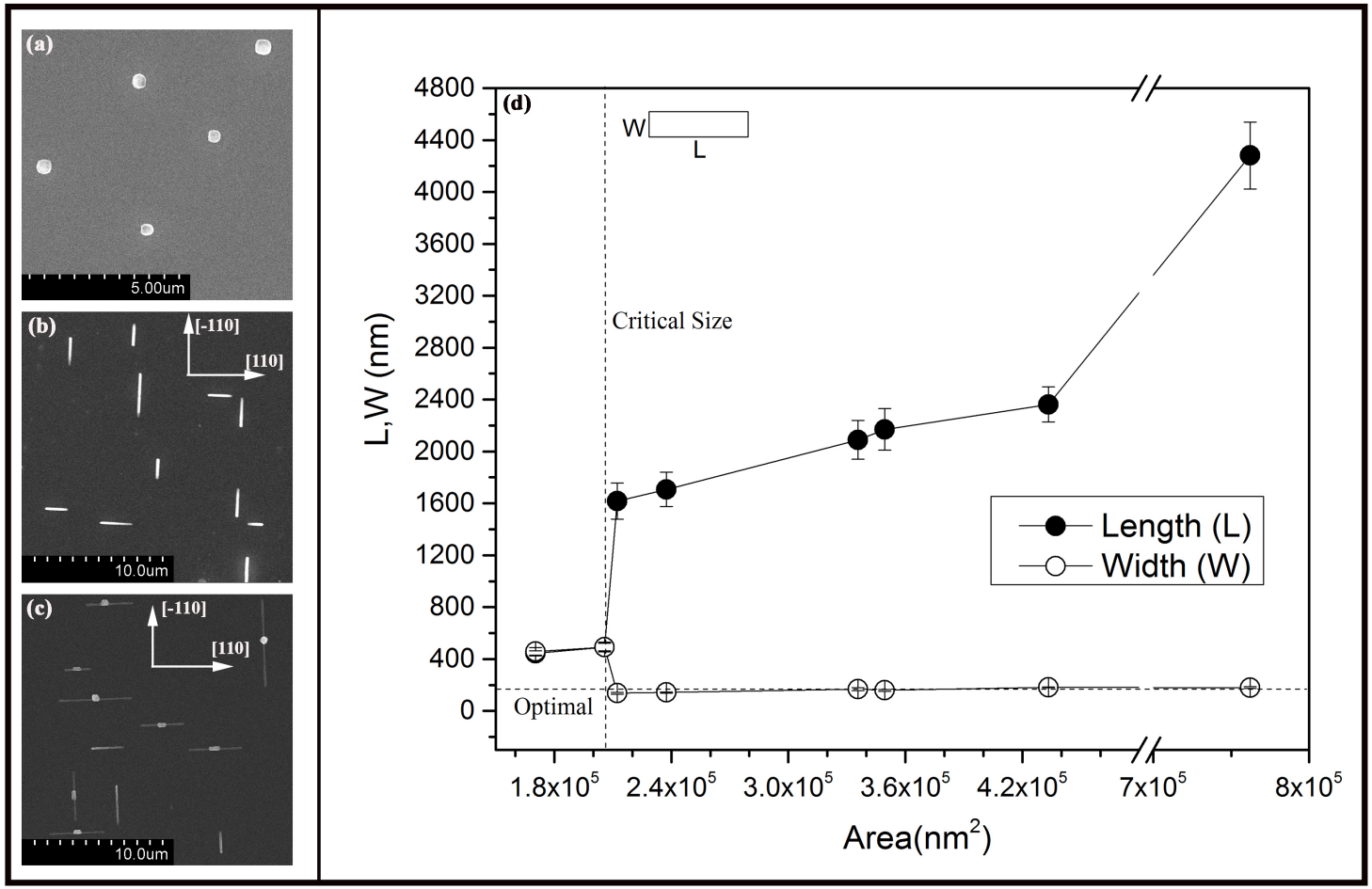


Figure 4.10: Three stages of $Cu_3Si$ island growth on HCI irradiated p-Si(100) substrate are shown as imaged using SEM. In (a) islands are square, until a shape transition to rectangular islands (b) long wire shaped islands (c) rectangular islands on the center of long wire (d) dependence of both island length L( closed circles) and width W(open circles) on the island surface area.

| Growth Mode Method: Substrate | Length (Min-Max) (nm) | Width (Min-Max) (nm) | Density (Min-Max) x $10^6$ [$cm^{-2}$] | Area (Min-Max) x $10^3$ [$nm^2$] | Deposition Time min | Void Nucleation Method |
|---|---|---|---|---|---|---|
| RDE: p(100) | 286 - 1402 | 88 - 281 | 2.12 - 25.5 | 44 - 123.7 | 1-5 | Thermal Annealing |
| HCI: p(100) | 388 - 2614 | 137 - 493 | 1.1 - 13.7 | 170.3 - 762.0 | 5 | HCI Irradiation |
| RDE: p(111) | 282 - 2877 | 160 - 400 | 0.87-7.3 | 44.9 - 980 | 1 - 5 | Thermal Annealing |
| HCI:p(111) | 444 - 4281 | 291 - 818 | 1.2 - 8.9 | 120.6 - 758.2 | 5 | HCI Irradiation |

Table 4.2: Dimensions of $Cu_3Si$ nanostructures of two growth modes ( RDE vs HCI assisted growth).

of the $Cu_3Si$ islands grown by HCI assisted growth process are $\sim$ 2 times that of RDE process. Since the deposition parameters (time, flux, pressure) were not altered throughout the experiment, it can be concluded that the nucleation rate of the HCI assisted $Cu_3Si$ islands is almost 2 times that of the RDE process and the density of these islands decreases by $\sim$ 50%.

The two typical processes that need to occur in the HCI assisted $Cu_3Si$ island growth process are generation of nucleation sites and the growth of $Cu_3Si$ islands at the nucleation sites. We can assume that a certain percentage of the HCI potential energy during neutralization is utilized to induce nucleation sites on the oxide surface. The size of these nucleation sites will depend on potential energy and fluence. However, the imaging of nucleation sites is not possible due to limitations in standard imaging tool resolving power. The observed increase in the length of the $Cu_3Si$ islands could be attributed to the size of the defect sites created by HCIs during interaction with the oxide surface. As shown in Fig. 3.21, HCIs need to break two Si dangling bonds present at the interface to created voids. To check the role of the ions in this, SRIM/TRIM model can be used to obtain an estimate of stopping ranges and energy loss rates [90]. For $Ar^{1+}$ at 1 keV, the expected average stopping range is approximately 3.5 nm. This is almost twice the depth of our oxide layer. From the SRIM calculations, therefore it is evident that HCIs can easily reach the interface and initiate Si bond breaking. Also the high etch yields would lead to larger size defect sites as explained in the context of Coulomb potential explosion model[84].

It is also reasonable to assume that the nucleation of defects is proportional to the irradiation time with a dependence on charge state that would effect the grown $Cu_3Si$ islands through the defect size. The nucleation of the $Cu_3Si$ island starts at the defect site/ nucleation sites induced by HCI and continues to grow until strain is completely relieved in agreement with the Tromp theory [48]. So, larger defect sites

could lead to larger island lengths which is consistent with the data in Table 4.2. Another possible explanation could be coalescence of nearest neighboring nanowires to form a single large nanowire. By this argument if two neighboring nanowires coalescence to form one the length of the nanowires would be almost twice that of RDE grown wires and the density would decrease by half in agreement with the data shown in Table 4.2. Within the SEM imaging, the coalescence of nanowires is not clearly evident. A combination of coalescence and charge state dependent potential sputtering processes can therefore not be ruled out.

### 4.5.2 Self Assembled Cu-Si Nanowires Growth on p-Si(111)

To understand the effect of substrate orientation, we repeated our experiments with $SiO_2$/Si(111) substrates. The HCI irradiation conditions, i.e charge species and fluence were chosen to be same. The observed shapes of the $Cu_3Si$ nanostructures grown on p(111) substrates with $Ar^{q+}$-HCI irradiation ($1<q<8$) and for low doses ( 1 x $10^{11}$ $cm^{-2}$ < Dose < 2.5 x $10^{11}$ $cm^{-2}$ ) are squares. With higher dose (> 2.5 x $10^{12}$ $cm^{-2}$) HCI irradiation for the charge state q=4, a change in the shape from square to nanowire was observed. No wire shaped nanostructures were observed with $Ar^{1+}$ and $Ar^{8+}$-HCI irradiation even for the dose as high as 5 x $10^{12}$ $cm^{-2}$. Orientations of the nanowires were found to be along [011] and [101] without any preference. From Fig. 4.11, it is evident that the shape of the nanostructures depends on both the charge state (potential energy) and dose.

For the $SiO_2$/p-Si(111) substrate irradiated with $Ar^{4+}$, the density of $Cu_3Si$ islands increases from 9 x $10^5$ $cm^{-2}$ to 3.5 x $10^6$ $cm^{-2}$ within a dose range of 2.5 x $10^{12}$ $cm^{-2}$ - 5 x $10^{12}$ $cm^{-2}$. However, higher q-HCI irradiation $Ar^{8+}$ at high dose of 5 x $10^{12}$ $cm^{-2}$, yielded a density of 9 x $10^6$ $cm^{-2}$. We also performed an irradiation

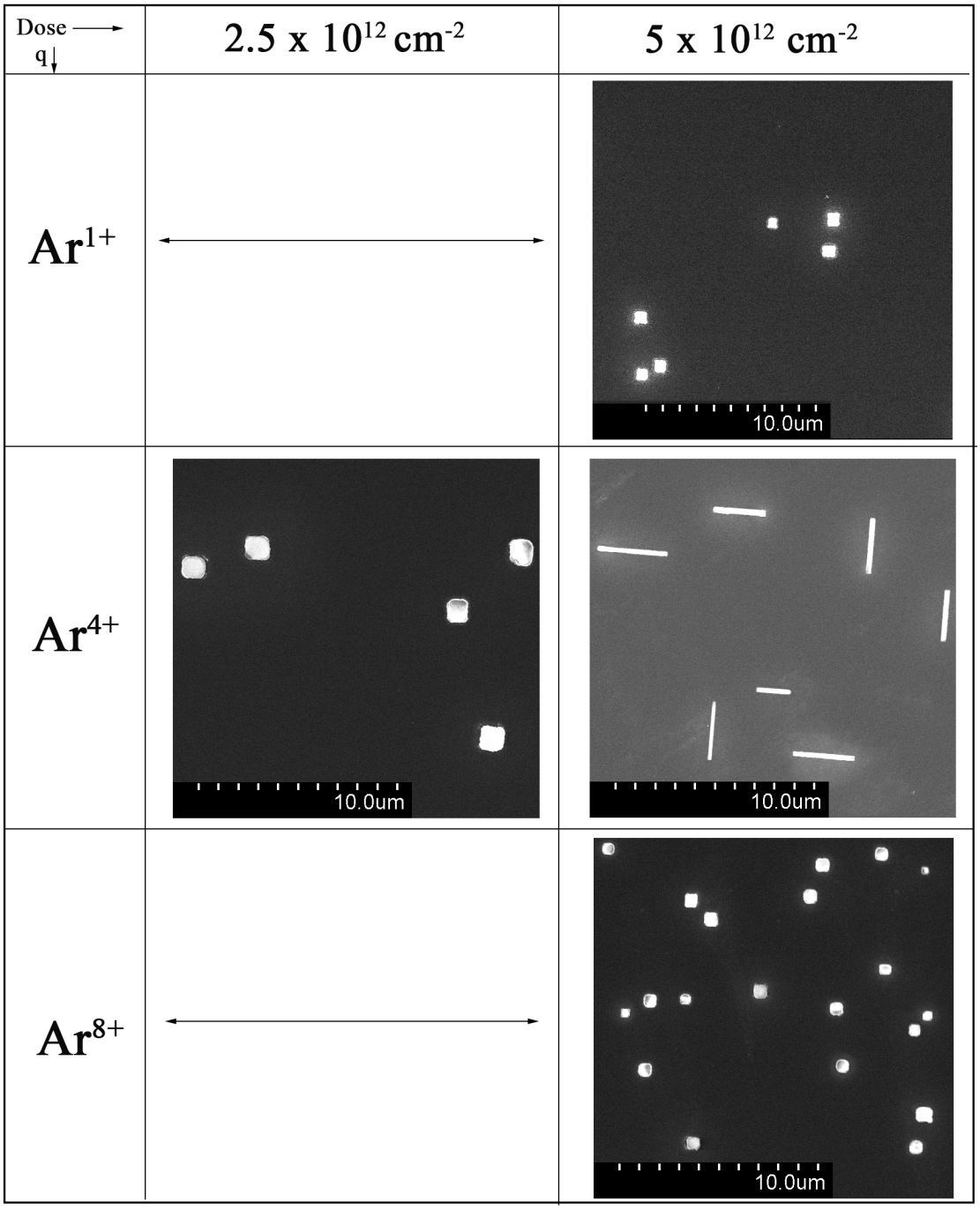


Figure 4.11: Cu deposited at 600°C on HCI irradiated $SiO_2$/p-Si(111) substrates of varying dose and charge state.

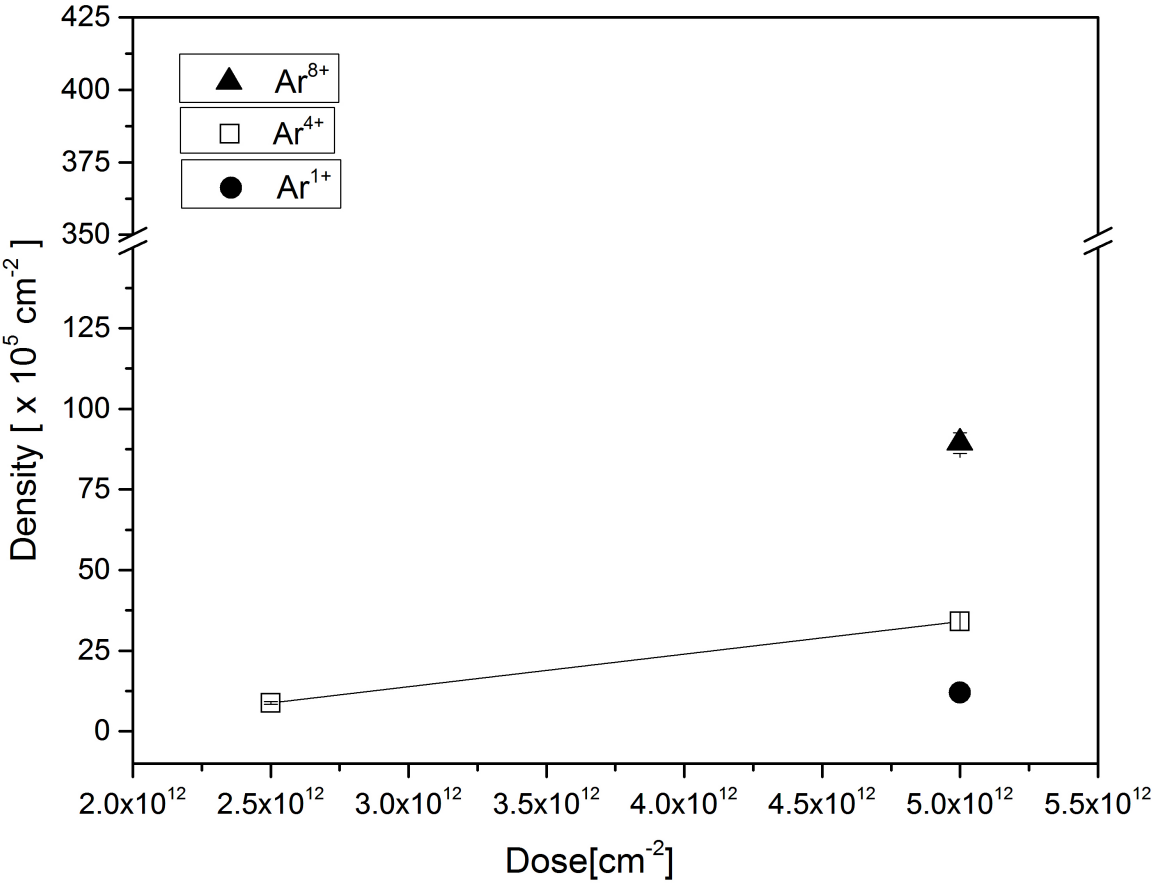


Figure 4.12: Average density of $Cu_3Si$ nanostructures versus dose on Si-p(111) substrate irradiated with $Ar^{q+}$ ions for charge state (q=1, 4, 8).

with a singly charged ion $Ar^{1+}$ at an ion dose of 2.5 x $10^{12}$ $cm^{-2}$, where any effects are assumed to be kinetic only. The remarkable feature is the strong q-HCI dependent $Cu_3Si$ growth, showing that q and density dependence are in the ratio of 1:4:8 to 1:2.8:3.5, and these trends are similar to those of $Cu_3Si$ islands grown on $SiO_2$/Si(100) substrates. The enhancement of the density at higher potential energies and charge states suggests a process resulting from the Coulomb explosion [87, 88].

As before the slope of the lines of Fig. 4.12 can be used to calculate a density per ion. These data(Fig. 4.13) demonstrate that $Ar^{q+}$ charge state dependence is linear. A power law relationship (density $\sim$ $q^{\gamma}$) for the density of the $Cu_3Si$ nanos-

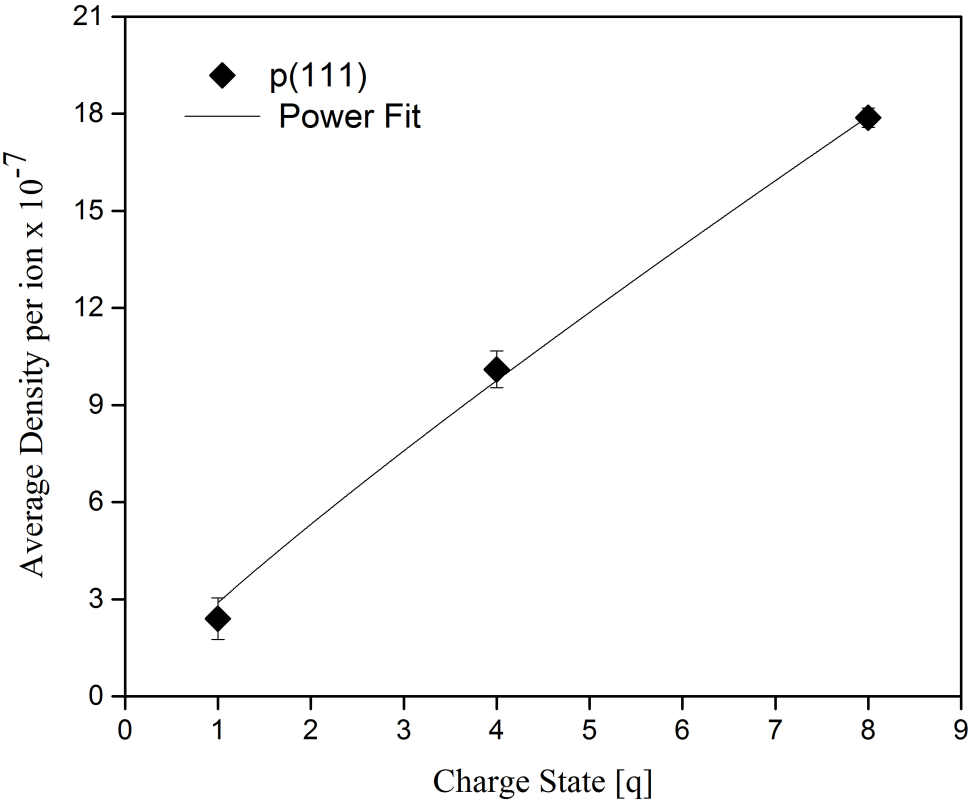


Figure 4.13: Normalized density per ion of $Cu_3Si$ nanostructures on Si-P(111) substrate obtained from dose dependent graph shown in Fig. 4.12 for $Ar^{q+}$ charge states q=1,4,8.

tructures gives, $\gamma \sim 0.9 \pm 0.04$ for $Ar^{q+}$ which is similar to the $SiO_2$/Si(100) result.

**Shape Transition:**

Representative $Cu_3Si$ islands growth on Si-p(111) substrates irradiated with $Ar^{q+}$ (1<q<4) are shown in Fig. 4.10. The growth on these substrates is similar to that of seen on p-Si(100) substrates. Up to a critical size the shape is observed to be square above which the shape transitions to rectangular. For the largest square island, the area is L x W = 5.5 x $10^5$ $nm^2$. The area of the island, where the shape transition takes place is $e^2\alpha_0^2$= 5.5 x $10^5$ $nm^2$. This provides the critical size ($e\alpha_0$) =

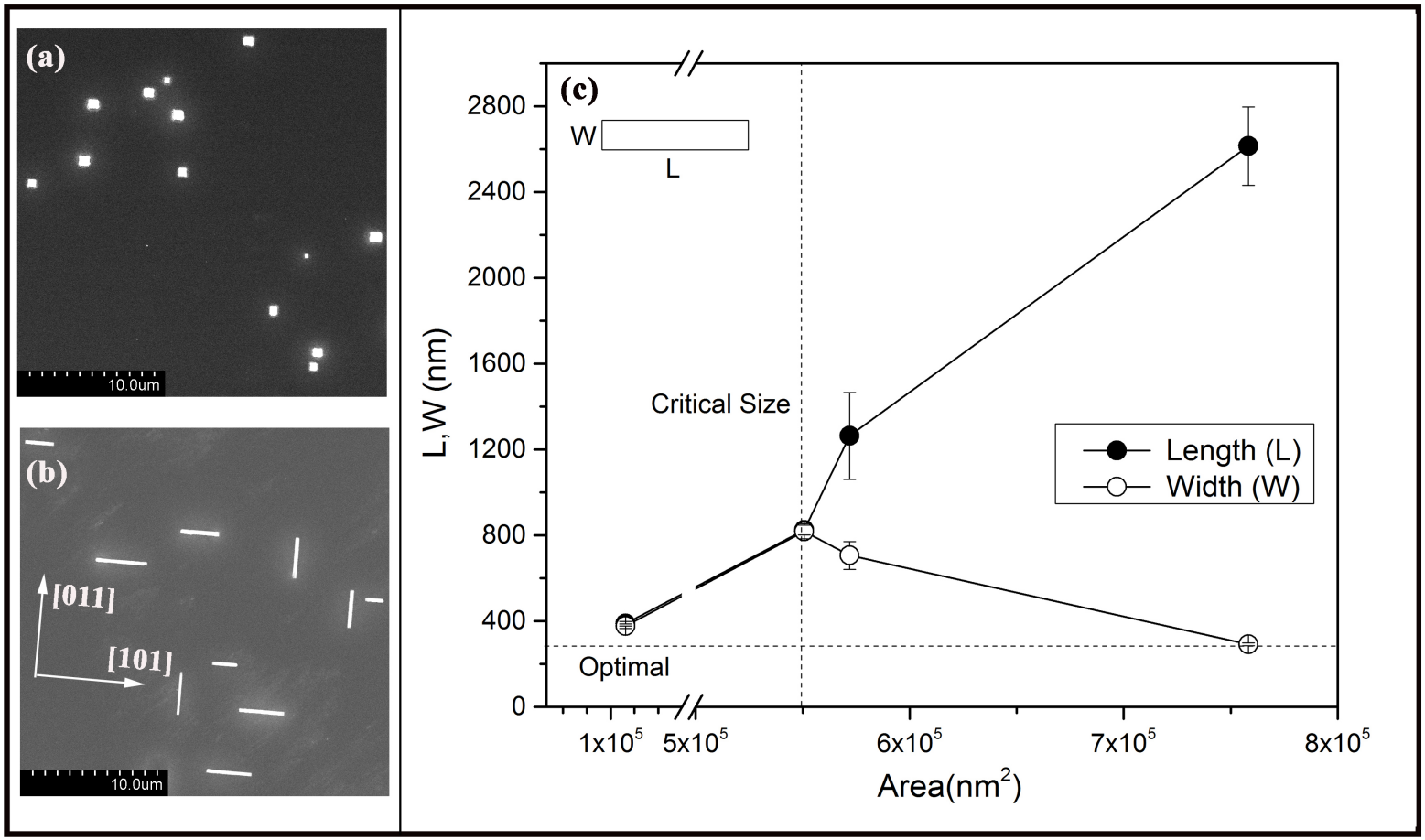


Figure 4.14: Two stages of $Cu_3Si$ island growth on HCI irradiated p-Si(111) substrate are shown as imaged using SEM. In (a) islands are square, until a shape transition to rectangular islands (b) long wire shaped islands (c) dependence of both island length L( closed circles) and width W(open circles) on the island surface area.

742 nm, as shown in Fig. 4.10 by the dotted line. It follows that for island length larger than 825 nm, L starts to increase much more rapidly while W decreases. As the area further increases the increase in length and slight decrease in the width lead to the formation of thin wires with a sharp increase in aspect ratio ($\sim$ 9:1 ) as predicted by the Tersoff model. For the longer islands the width approaches towards the optimum value W $\simeq$ 273 nm. The aspect ratios of nanowires grown on p-Si(100) are almost three times that of the wires grown on p-Si(111) but they tend to exhibit similar growth morphology. The islands orientation is observed along [011] and [101] directions without any preference as shown in Fig. 4.10(b). Also, no changes in the heights of the $Cu_3Si$ islands were observed in contrary to the strain relief mechanism exhibited by the islands grown on p(100) substrates. Irrespective of substrate orientation nanowires were grown on Si substrates. This implies that the stress relaxation and shape transition are also dependent on the the type of dopant. Also, in P-Si copper precipitates are positively charged and repel $Cu^+$, thus suppressing the precipitation in the bulk and making out-diffusion predominant [68]. It is known from our previous work that the activation energies and reaction rates of $Cu_3Si$ islands on p-Si(111), p-Si(100) and n-Si(111) are not same. p-Si(111) and p-Si(100) possessing approximately the same activation energies tend to undergo nanowire shape transition whereas n-Si(111) with high activation energy undergoes a trapezoidal shape transition.

**RDE vs HCI assisted Growth Mode :**

The dimensions of $Cu_3Si$ islands grown on p-Si(111) substrate via RDE vs HCI assisted growth modes are shown in Table 4.2. The maximum lengths of the $Cu_3Si$ islands grown by HCI assisted growth process are $\sim$ 1.5 times that of RDE process. Since, the deposition parameters (time, flux, pressure) were not altered throughout

the experiment, it can be concluded that the nucleation rate of the HCI assisted $Cu_3Si$ islands is almost 1.5 times that of the RDE process.

**$Cu_3Si$ nanowires lengths on p-Si(100) vs p-Si(111) substrates:**

The maximum lengths of the $Cu_3Si$ nanowires grown on p-Si(111) substrate is $\sim$ 1.7 times that of the $Cu_3Si$ nanowires grown on the p-Si(100) substrate. The possible factors that could have contributed to the observed differences in the lengths of nanowires are discussed here. One of the crucial steps in the growth process of $Cu_3Si$ islands is creation of voids at the interface and in the later stages these voids act as nucleation sites and facilitate the growth of $Cu_3Si$ islands. The process of void formation at the $SiO_2$/Si interface is achieved by breaking the Si-O bonds present at the interface using HCI irradiation. As we noted earlier in Fig. 3.21, the Si{111}plane has only one dangling bond at the interface whereas Si{100} plane has two dangling bonds at the interface [72–74]. In order to facilitate the void growth at the $SiO_2$/Si interface only one Si dangling bond needs to be broken on Si{111} plane whereas two dangling bonds needs to be broken on the Si{100} plane. Since the HCI irradiation parameters were not altered and the Si{100} plane possesses twice the number of dangling bonds at the interface compared to the Si{111} planes, it is reasonable to assume that the area of the voids created on both the Si planes, i.e. {111} and {100}, would not be same. An HCI could etch more area and create bigger voids on a Si{111} plane compared to that of Si{100} plane due to the lower number of dangling bonds that needed to be broken at this interface. The maximum lengths of $Cu_3Si$ nanowires observed on Si{111} and Si{100} substrates in the ratio of 1.7:1 could be attributed to the 1:2 ratio of dangling bonds present at the interface of silicon {111} and {100} planes.

# Chapter 5

# Surface Modification of Polycarbonate with HCI beams of Argon and Oxygen

This chapter investigates the surface properties of polycarbonate(PC,Lexan) prior to and after HCI treatment using X-ray photoelectron spectroscopy (XPS). The primary objective of this experiment is to understand how the surface properties of polycarbonate irradiated with HCI beams of argon and oxygen are modified.

## 5.1 Introduction

Polycarbonate (PC, Lexan) is a promising polymeric material, characterized by excellent electronic, thermal, physical and optical properties. It has attracted significant interest in a variety of engineering applications such as electrical, telecommunications, optics, automotive lighting, bio sensors, solar cells and nuclear track detectors etc. because of its light weight, durability, high optical transmittance, high

deformation temperature, design flexibility and cost effectiveness [23–25]. As a result, there is also increased interest in methods of surface modification of polycarbonate that might improve its structural, chemical, optical and mechanical properties.

Many techniques such as wet chemical etching, electrical, plasma, UV, gamma-ray, X-ray, electron beams and swift heavy ions are being evaluated as possible ways to modify PC properties [91–100]. Ion beams have a high potential and provide a unique way to make the chemical, optical, mechanical and structural changes in the macromolecular structure. Ion beams are already a proven technology to modify the surface properties of metals, semiconductors and ceramics. In fact, ion beams can more effectively modify the surface properties of polymers because the polymer bond strength is much lower than metals, semiconductor and ceramics. Since the interaction between ions and a substrate involves a dense deposition of energy and an interaction time scale that is shorter than an elementary chemical event, it is expected that ions will initiate non-conventional chemistry in polymers [101]. For example, the interaction of ion beams with polymers leads to complex chemical reactions like chain scission, cross-linking and formation of reactive atoms and free radicals [97, 99, 100, 102–104]. Already it has been observed that ion beam irradiation enhances the adhesion, conductivity, wettability and solubility of polymers [105–109].

In contrast to singly charged ions where the kinetic energy of the projectile constitutes the important parameter, potential energy plays a key role in the highly charged ion (HCI) interactions. HCIs posses large potential energies, which are the sum of the ionization energies of the removed electrons. This potential energy can be liberated during the impact of the ions with the solid surface and can be deposited into nanometer sized region on the surface. The deposited potential energy can induce radiation effects such as craters, hillocks and pits and can facilitate chemical reactions that require high temperatures [76, 101]. This makes HCIs a promising tool

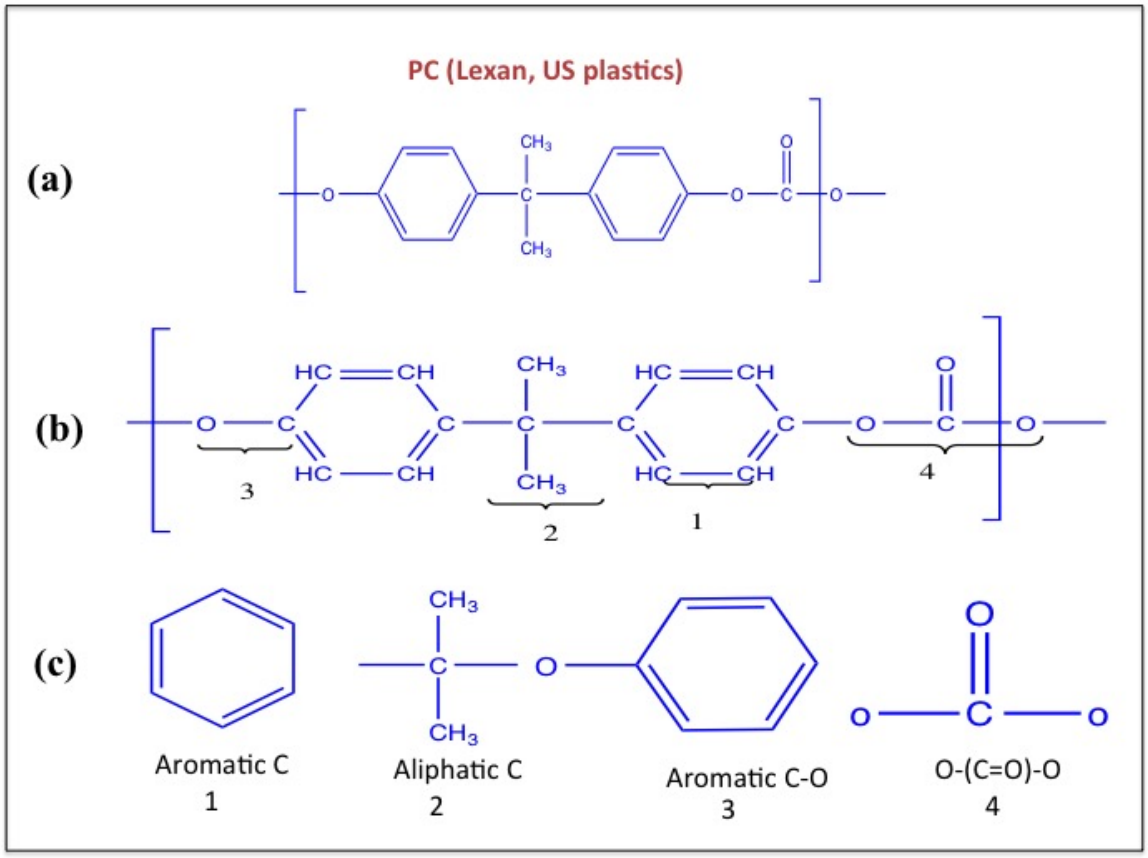


Figure 5.1: (a) Polycarbonate (PC, Lexan) Molecular structure. (b), (c) Different types of carbon bonds present in the polycarbonate structure.

for surface modification and characterization. HCI effects on polymers have not been well explored. They could prove useful for the fabrication of multilayer devices on polycarbonate substrates, for example, as it is necessary to modify such surfaces to improve their adhesion for the long durability of coatings. This improved wettability is commonly achieved by oxidizing polymer surfaces.

In the present study, the modification of the physical and chemical properties of polycarbonate substrates using HCIs has been investigated. Specifically, we have irradiated PC surfaces with HCI beams of $Ar^{8+}$, $O^{3+}$ and $O^{5+}$ of varying ion fluences to probe the physical, chemical and structural effects induced by HCIs. Poly-

carbonate could undergo various surface chemical reactions when it is subjected to HCI beams. As some groups report, the C-O bond adjacent to the carbonyl group in PC is the weakest bond of the polymer chain, lacking resonance stabilization of the phenyl groups [96, 110]. According to Hama and Shinohara, CO and $CO_2$ are produced as volatile by-products of phenoxy and phenyl radical production with relative concentrations of CO/ $CO_2$ $\approx$ 2 and phenoxy / phenyl $\approx$ 5 [34]. Irradiation makes the polymeric molecule scission in four different positions as shown in Fig. 5.1: positions 1 and 2, in the carbonyl group, position 3 between the carbonate group and the benzene ring and position 4 between the isopropylidene and the benzene ring. The phenoxy and the phenyl radicals are formed as consequence of the irradiation with the polymer. The phenoxy-type and phenyl-type free radicals are not stable and thereafter cross linking of the free radicals may happen by rearrangement of oxygen atoms or reacting with hydroxyl groups. Therefore, chain scission and cross-linking occurs simultaneously when polycarbonate is subjected to irradiation.

## 5.2 Experiment

A sheet of commercially available polycarbonate (Lexan, US Plastics) sheet was diced into squares($\sim$ 10 mm x 10mm; 100 $mm^2$). Prior to irradiation, these diced samples were cleaned using DI water, isopropyl alcohol and ethanol. The cleaned and diced PC samples were then mounted on a standard Omicron style platen and positioned directly in front of the deceleration lens inside the CUEBIT target chamber. Details of the experimental setup were given in Chapter 4 and can be found in the literature [79, 80, 111]. A schematic of the experiment is shown in Fig. 5.2. The fluences used for irradiation were in the range of $10^{12}$ to $10^{13}$ $cm^{-2}$. The species used for the irradiation were $O^{3+}$, $O^{5+}$ and $Ar^{8+}$ with potential energies 102 eV, 290 eV and

567 eV respectively. To avoid neutralization of the beam due to charge exchange with background gases, the pressure in the beamline was kept in the low $10^{-9}$ mbar range. The kinetic energies of the ions were kept low to avoid deep penetration into the target and were set at 1 keV and 0.375 keV for argon and oxygen respectively. Beam currents were measured by a Faraday cup mounted in the same plane as the sample and these varied from $\sim$ 110 nA/cm$^{-2}$ to 1500 nA/cm$^{-2}$ for oxygen beams and beam current varied from $\sim$ 335 nA/cm$^{-2}$ to $\sim$ 560 nA/cm$^{-2}$ for argon beams. Spatial profiles of the beam were obtained by translating the Faraday cup in the plane perpendicular to the incident beam direction. The beams were approximately Gaussian in shape with $\sim$3 mm FWHM as shown in Fig. 5.2. HCI irradiation specifications are shown in Table 5.1.

## 5.3 XPS Results and Analysis

Changes in the chemical composition of the polycarbonate samples were measured using X-ray photoelectron spectroscopy (XPS). The XPS spectra were obtained utilizing Kratos XPS spectrometer using a monochromatic $K_\alpha$ X-ray (h$\nu$=1486.6 eV). The base pressure inside the XPS chamber while acquiring XPS spectra was 5.5 x $10^{-7}$ Torr. The polycarbonate molelcular structure consists of Benzene rings (Aromatic), carbon, oxygen and hydrogen atoms as shown in Fig. 5.1. The PC molecules connect to each other through C-O bonding.

The interaction of singly charged ion beams with polycarbonate is explained by two step model in the literature [91, 97, 98, 104, 112, 113]. In this model, ion irradiation initiates C-C bond breaking and leads to chemically active dangling bonds. These dangling bonds react with oxygen gas flowing across the sample resulting in the formation of C-O bonds. For the above process to occur, the flow of oxygen gas is

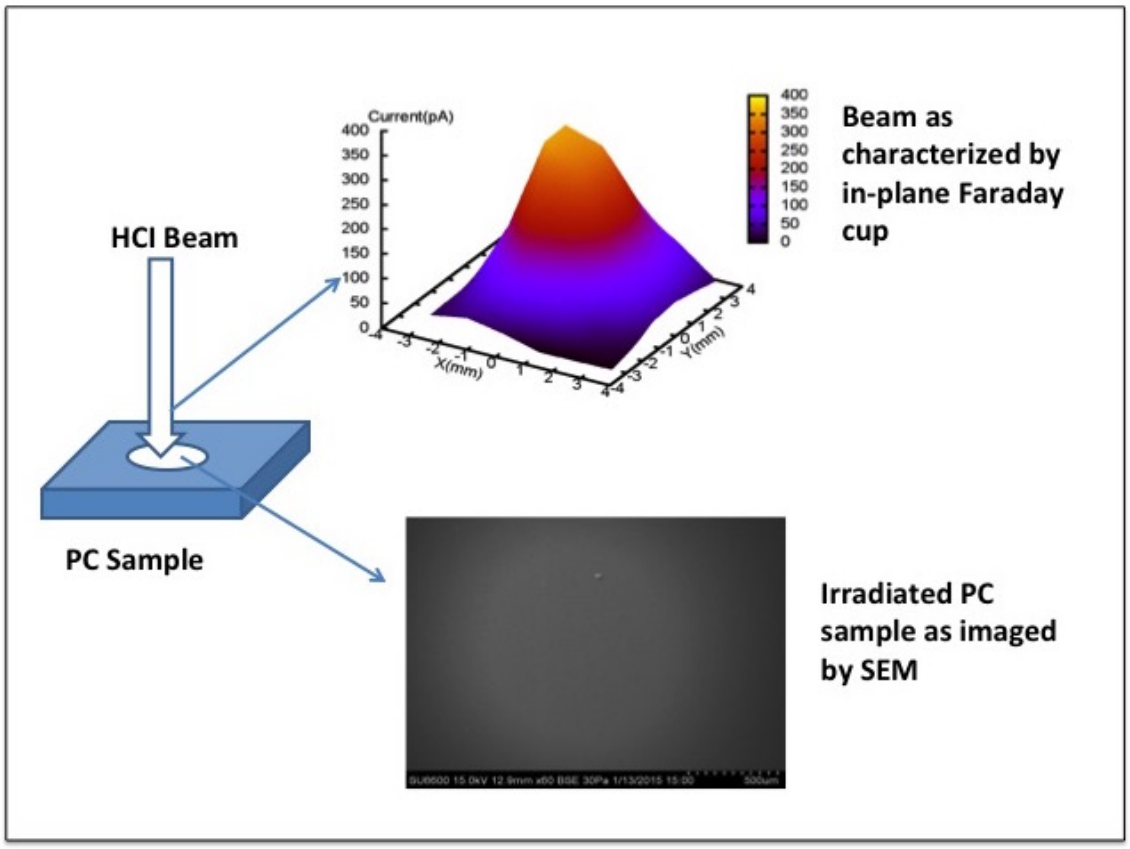


Figure 5.2: Basic schematic of the experiment for PC irradiation and analysis.

| Charge Species | Energy (eV) | Current (nA) | Fluences ($cm^{-2}$) | Pressure (mbar) | Background Oxygen Presence |
|---|---|---|---|---|---|
| $Ar^{8+}$ | 1000 | 335-560 | 1.41 x $10^{12}$ - 4.24 x $10^{12}$ | $10^{-8}$ | No |
| $O^{3+}$ | 375 | 540-1500 | 6.56 x $10^{12}$ - 1.22 x $10^{13}$ | $10^{-8}$ | No |
| $O^{5+}$ | 375 | 110-820 | 1.98 x $10^{12}$ - 4.95 x $10^{12}$ | $10^{-8}$ | No |

Table 5.1: HCI irradiation specifications of PC.

a requirement and no discernible changes in C-O bond intensities are observed in the absence of oxygen gas flow. It can be seen from our data, however, that irradiation with highly charged ions(HCIs) without oxygen gas flow results in formation of C-O bonds quantitatively comparable to those observed for irradiation with $Ar^{1+}$ with oxygen gas flow.

The interaction of HCIs with polymers can lead to complex chemical reactions like chain scission and the formation of unstable reactive atoms and free radicals which result in changes in structure as well as in the properties of the polymers. Free radicals are not stable and thereafter undergo cross-linking by rearrangement of oxygen atoms or by reacting with hydroxyl groups to form stable products. Since the bond scission energies of aromatic C-H/C-C, aliphatic C-H/C-C, aromatic C-O and carbonate group (positions 1,2,3 and 4 in Fig. 5.3)are about a few eV, the main action of a highly charged ion passing through a polymer is to initiate bond scission on the surface. This process should continue until the HCI consumes all of its energy through polymer interactions. There is a very low probability for the highly charged ion to knock out the nucleus of a polymer chain. For the present study, the effects of reactive ($O^{3+}$, $O^{5+}$) and non-reactive ($Ar^{8+}$) ions on the modification of the physical and chemical properties of polycarbonate substrates has been investigated.

XPS is sensitive to chemical shifts of a few eV and is thus used to identify different bonds present at the surface. C-1s and O-1s spectra were recorded for both pristine and irradiated samples. The C-1s spectra were fit by a Gaussian/Lorentzian mixed model after appropriate background subtraction and corrections for charging effects. The XPS spectra were recorded at different positions on each sample and a spatial variation in the XPS spectra across the irradiated samples was observed. The spectrum corresponding to the "peak position" of the beam(high intensity) was considered for all subsequent analysis of dose and charge state effects. A representative

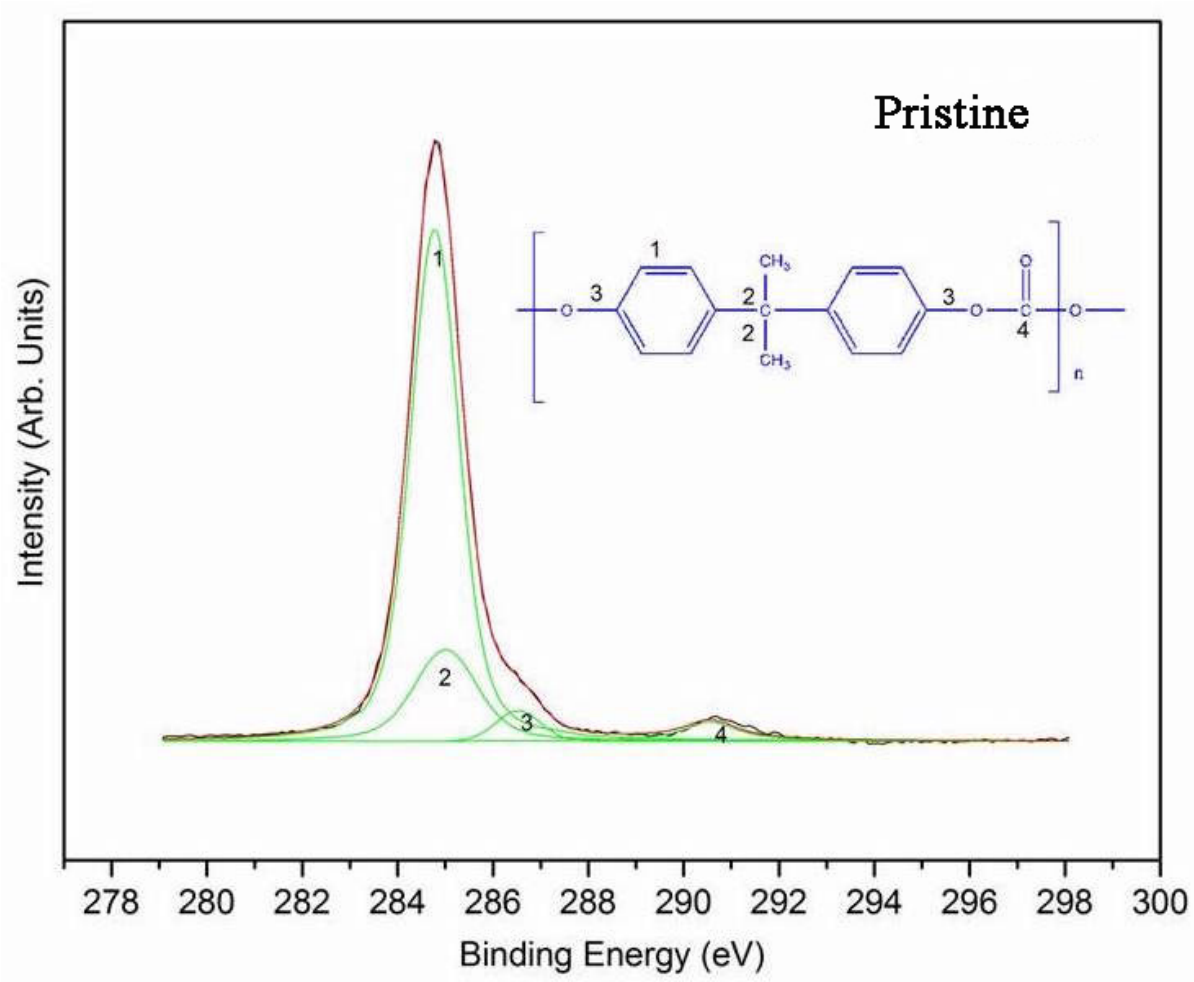


Figure 5.3: XPS high-resolution C-1s spectrum of untreated (pristine) PC.

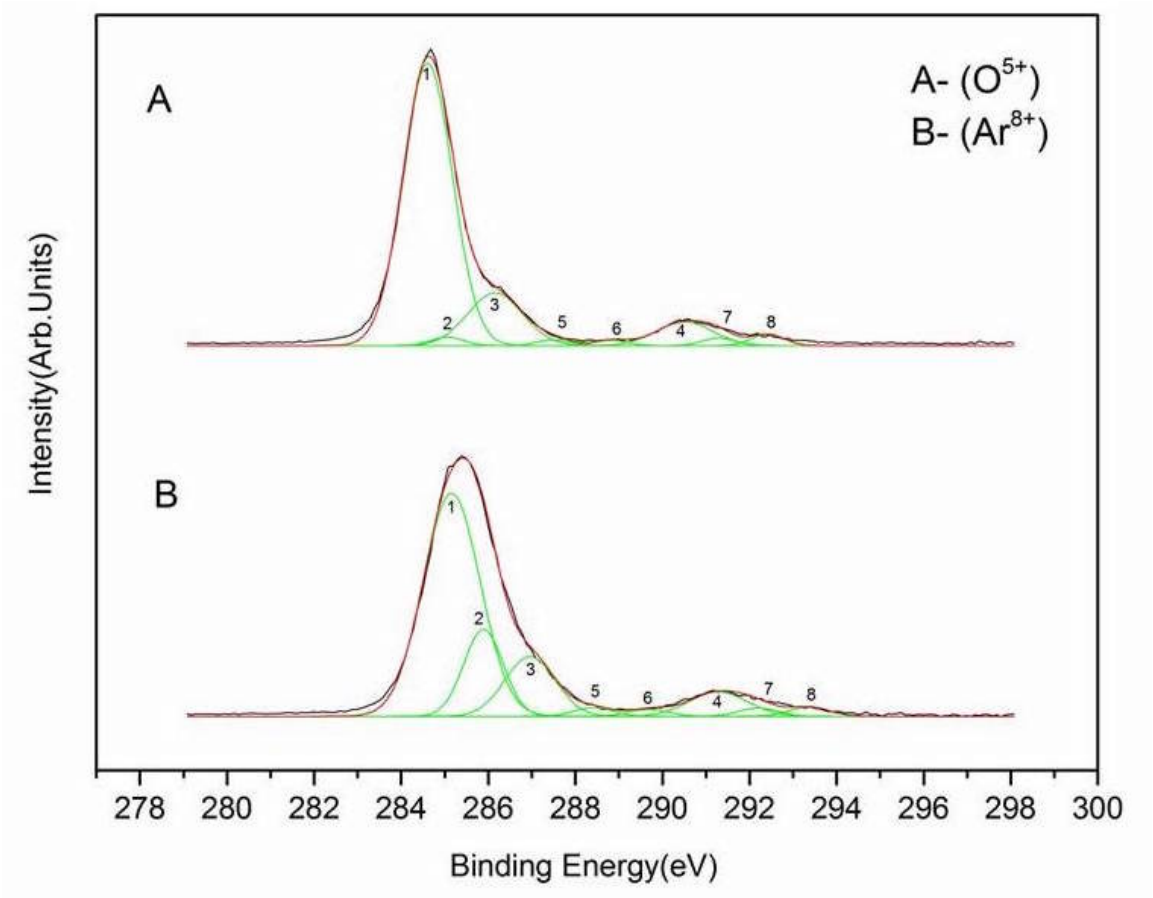


Figure 5.4: Typical XPS spectra of PC irradiated with (A)$O^{5+}$ and (B)$Ar^{8+}$ ion beams.

XPS peak fit of a C-1s spectrum of a pristine PC substrate exhibits four peaks as shown in Fig. 5.3. The binding energy of the C-1s aliphatic C-H (285.0 eV) was used to correct for charging effects of the PC under X-ray irradiation. The spectrum contains a broad peak at 284.5 eV with high intensity and another broad beak at 290.5 eV with much lower intensity. Two smaller and overlapping peaks were observed at 286.2 eV and 290.5 eV.

For the case of irradiated PC substrates the C-1s spectrum can be represented by eight different peaks(see Fig. 5.4) corresponding to aromatic C-H/C-C at 284.5 eV (Peak 1), aliphatic C-H/C-C at 285.0 eV (Peak 2), aromatic C-O at 286.2 eV

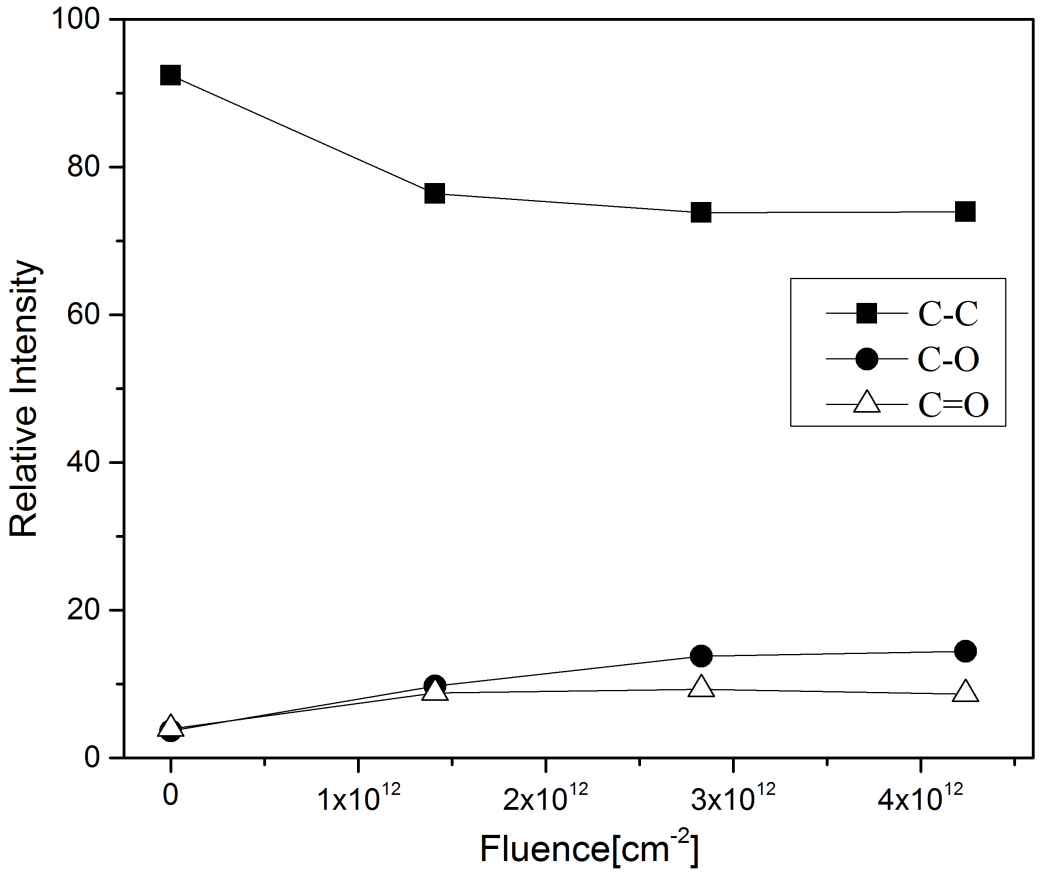


Figure 5.5: Relative intensities of C-C, C-O, C=O bonds of PC irradiated with an $Ar^{8+}$ ion beam.

(Peak 3), carbonate (O-(C=O)-0) at 290.5 eV (Peak 4), aliphatic C=O at 287.5 eV (Peak 5), O-C=O at 288.8 eV (Peak 6) and two $\pi - \pi$ satellite peaks at 291.3 and 292.5 eV (Peaks 7,8). Peaks 5, 6, 7 and 8 are absent in the untreated specimens and only arise following irradiation. A Gaussian/Lorenzian mixed model peak fit analysis with appropriate relative sensitivity factors (RSF) was used to analyze and compute the relative intensities and full width half maximum (FWHM) from the irradiated regions as shown in Table 5.2.

| Dose ($cm^{-2}$) | Charge State | Aromatic C-H 248.5 eV | Aliphatic C-H 285.0 eV | Aromatic C-O 286.2-286.5 eV | -O-(C=O)- 290.3-290.5 eV | C=O 287.5-288.0 eV | O-C=O 288.8-289.0 eV | $(\pi - \pi)$ 291.3-292.5 eV |
|---|---|---|---|---|---|---|---|---|
| 0 | | 74.81 | 17.57 | 3.65 | 3.96 | 0 | 0 | 0 |
| 6.56 x $10^{12}$ | $O^{3+}$ | 69.74 | 10.40 | 12.20 | 7.63 | 0 | 0 | 0 |
| 1.22 x $10^{13}$ | $O^{3+}$ | 62.77 | 10.57 | 14.65 | 0 | 1.55 | 10.47 | 0 |
| 1.98 x $10^{12}$ | $O^{5+}$ | 71.52 | 5.58 | 10.0 | 5.57 | 1.96 | 0.82 | 4.48 |
| 4.95 x $10^{12}$ | $O^{5+}$ | 71.52 | 1.39 | 14.92 | 6.87 | 0.96 | 0.91 | 3.15 |
| 1.41 x $10^{12}$ | $Ar^{8+}$ | 59.56 | 16.82 | 9.73 | 5.49 | 1.83 | 1.49 | 5.04 |
| 2.83 x $10^{12}$ | $Ar^{8+}$ | 58.16 | 15.65 | 13.75 | 6.49 | 1.56 | 1.26 | 3.12 |
| 4.24 x $10^{12}$ | $Ar^{8+}$ | 58.95 | 14.68 | 14.40 | 5.51 | 1.99 | 1.15 | 3.08 |

Table 5.2: C 1s high-resolution spectra curve-fit results of pristine and HCI treated PC. Each entry represents the relative integrated intensity of the given peak in the measured and fit XPS spectrum.

### 5.3.1 Nonreactive Species $Ar^{8+}$

As shown in Fig. 5.3, an XPS spectrum of an untreated PC substrate exhibits four peaks. Upon $Ar^{8+}$ irradiation, the XPS spectrum exhibits eight peaks as shown in Fig. 5.4(B) with the peak intensities as shown in Table 5.2. At an $Ar^{8+}$ ion fluence of 1.41 x $10^{12}$ $cm^{-2}$, the C-C (Aromatic C-H + Aliphatic C-H ) bond intensity decreases to 76.4 % whereas the bond intensities of C-O and C=O increases to 9.73% and 8.81% respectively. It is expected that an HCI will induce chain scission and initiate the formation of unstable and reactive free radicals on PC. These free radicals will undergo a cross linking mechanism to form stable compounds. For example, as a result of cross linking, the new species O-C=O at 288.8 eV is generated on the polymer surface. The discrete shake up ($\pi - \pi$) satellite peaks observed at 291.3 eV and 292.5 eV belongs to aromatic C-H/C-C (benzene ring) and carbonate(C=O group). The presence of the peaks indicates that $Ar^{8+}$ modifies the aromatic C-H/C-C and carbonate groups. As the $Ar^{8+}$ ion fluence is increased to 4.24 x $10^{12}$ $cm^{-2}$, the C-C bond intensity decreases to 74% and the bond intensities of C-O and C=O increase to 14.40% and 8.65%, respectively. The trend suggests that the C-C, C-O and C=O bond intensities saturates at$\approx$ 74%, 14% and 8.65% respectively as shown in Fig. 5.5. In order to convert polycarbonate from hydrophobic to hydrophilic, a decrease in the C-C bond intensity and an increase in the C-O bond intensity is essential. From our data it is evident that the C-O bond intensity saturates at $\approx$ 14% which is similar quantitatively to experiments with singly charged argon ions in presence of oxygen gas[91, 98, 104, 113]. We note that the ion fluences in our experiment are on the order of $10^{12}$ $cm^{-2}$ whereas the singly charged experiments are conducted in the range of $10^{15}$-$10^{16}$ $cm^{-2}$. HCIs tend to produce similar behavior even at much lower doses and a flow of oxygen gas is not needed. This makes HCIs a promising and potential

candidate for the surface modification of polymers.

### 5.3.2 Reactive Species $O^{3+}$ and $O^{5+}$

Oxygen is considered to be vital for free radicals to crosslink and form stable polymer products. As discussed above, the increase in the intensities of C-O and C=O bonds is attributed to cross-linking of free radicals by rearrangement of oxygen atoms. The abundance of these bonds is directly related to the applications like enhanced wettability and adhesion. As a result, there has been increasing interest to understand the role of oxygen. Several groups in the past have irradiated polymers with heavy and light ions in oxygen ambiance [91, 98–100, 112, 114]. When compared to oxygen atoms, oxygen ions are more reactive. Therefore we also irradiated polycarbonate samples with HCI beams of $O^{3+}$ and $O^{5+}$ at varying fluences to investigate the effects of oxygen ions on the structure and chemistry of PC.

**$O^{3+}$ Irradiation:**

As shown in Table 5.2, XPS spectra of a PC substrate irradiated with $O^{3+}$ ions exhibits 4 peaks like untreated PC at low dose of 6.56 x $10^{12}$ $cm^{-2}$ and two additional peaks ($\pi - \pi$) emerge at 287.5 eV and 288.8 eV at high doses of 1.22 x $10^{13}$ $cm^{-2}$ irradiation.

An $O^{3+}$ irradiation with an ion fluence of 6.56 x $10^{12}$ $cm^{-2}$ leads to a C-C (aromatic C-H + aliphatic C-H ) bond intensity decrease to 80 % whereas the bond intensities of C-O and C=O increase to 12.2% and 7.63% respectively. As the $O^{3+}$ ion fluence is increased to 1.22 x $10^{13}$ $cm^{-2}$, the C-C bond intensity decreases to 73 % and the bond intensities of C-O and C=O increase to 14.7 % and 12.02%, respectively. Unlike $Ar^{8+}$ irradiation, the trend suggests that the C-C, C-O and C=O bond intensities haven't reached saturation with $O^{3+}$ ion fluences as high as 1.22 x

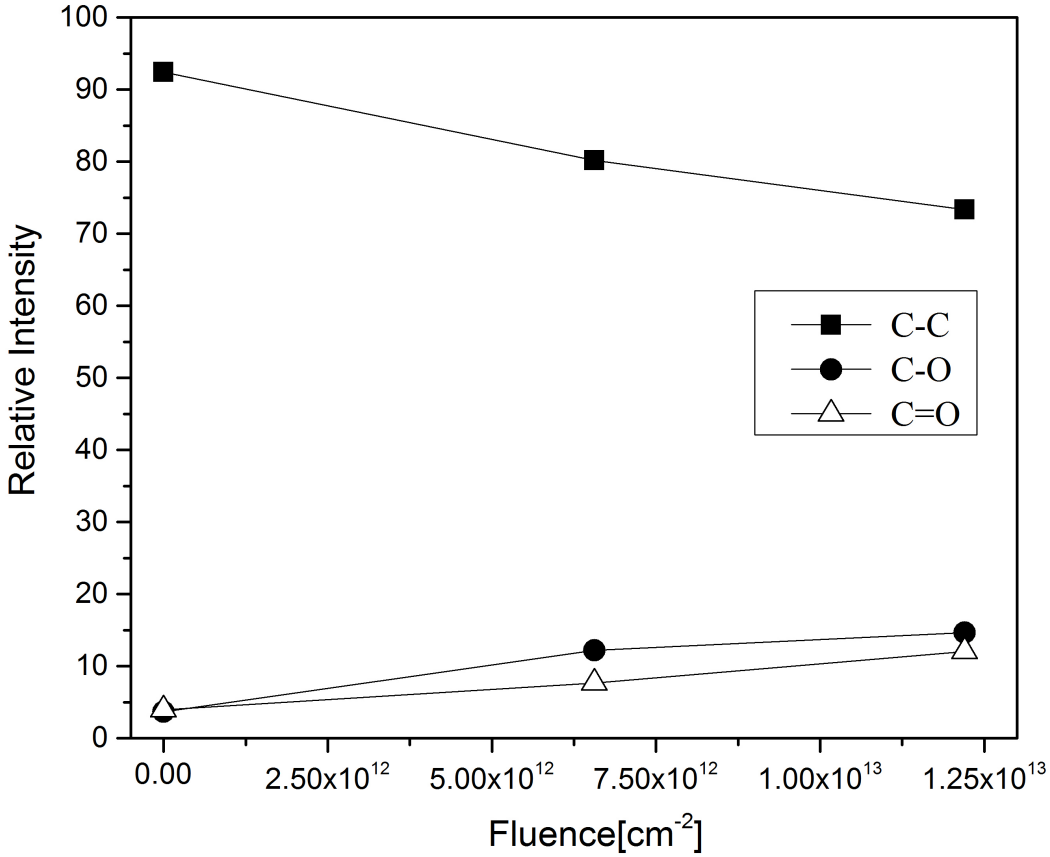


Figure 5.6: Relative intensities of C-C, C-O, C=O bonds of PC irradiated with $O^{3+}$ ion beams.

$10^{13}$ cm$^{-2}$ as shown in Fig. 5.6. The emergence of two new peaks($\pi - \pi$), at 287.5 eV and 288.8 eV with high $O^{3+}$ ion fluences of 1.22 x $10^{13}$ cm$^{-2}$ signifies the attack of $O^{3+}$ ions on the aromatic C-H/C-C and carbonate groups. These new peaks can also be attributed to bond scission and cross-linking by rearrangement. As the $O^{3+}$ ion fluence is varied from 6.56 x $10^{12}$ cm$^{-2}$ to 1.22 x $10^{13}$ cm$^{-2}$, the increase in the C-O bond intensity is $\sim$ 14%. The C-O bond intensity is approximately the same for both $Ar^{8+}$ and $O^{3+}$ irradiations, indicating that the presence of oxygen has only a minor effect on the C-O bond formation unlike other singly charged ion experiments where no considerable increase in the C-O bond intensity is observed in the absence of oxygen gas flow across the sample [98, 103].

**$O^{5+}$ Irradiation:**

As shown in Table 5.2, XPS spectra of PC substrates irradiated with $O^{5+}$ ions exhibit 8 peaks. All eight peaks were observed in XPS spectra for PC samples irradiated with $O^{5+}$ ions even at a low fluence of 1.98 x $10^{12}$ cm$^{-2}$ unlike the $O^{3+}$ irradiated samples. The eight peaks shown in Fig. 5.4(a) correspond to aromatic C-H/C-C at 284.5 eV (Peak 1), aliphatic C-H/C-C at 285.0 eV (Peak 2), aromatic C-O at 286.2 eV (Peak 3), carbonate (O-(C=O)-0) at 290.5 eV (Peak 4), aliphatic C=O at 287.5 eV (Peak 5), O-C=O at 288.8 eV (Peak 6) and two $\pi - \pi$ satellite peaks at 291.3 and 292.5 eV (Peaks 7,8) respectively.

For an $O^{5+}$ irradiation with an ion fluence of 1.98 x $10^{12}$ cm$^{-2}$ , the C-C (aromatic C-H + aliphatic C-H ) bond intensity decreases to 77 % whereas the bond intensities of C-O and C=O increase to 10% and 8.3%, respectively. As the $O^{5+}$ ion fluence is increased to 4.95 x $10^{12}$ cm$^{-2}$, the C-C bond intensity decreases to 73 % and the bond intensities of C-O and C=O increase to 15 % and 8.7%, respectively. The trend suggests that the C-C, C-O and C=O bond intensities also haven't completely reached saturation with $O^{5+}$ ion fluences as high as 4.95 x $10^{12}$ cm$^{-2}$ as shown in Fig.

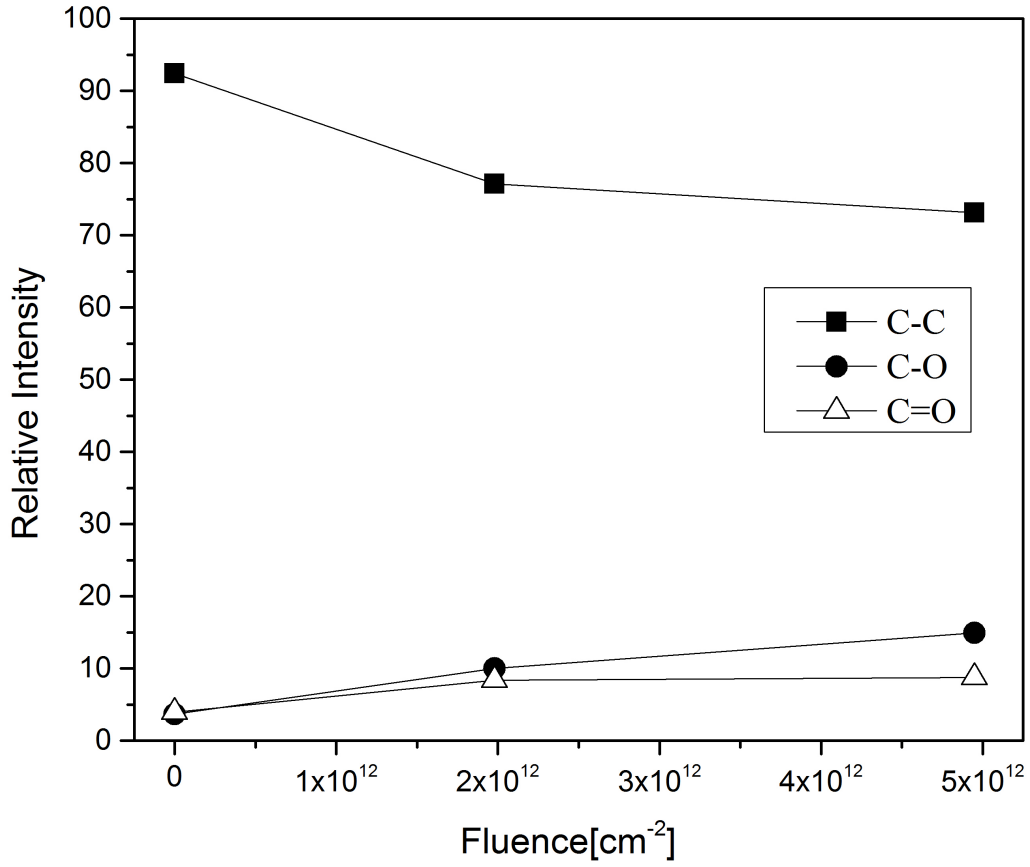


Figure 5.7: Relative intensities of C-C, C-O, C=O bonds of PC irradiated with $O^{5+}$ ion beams.

5.5. The presence of $\pi - \pi$, at 287.5 eV and 288.8 eV even with low $O^{5+}$ ion fluence of 1.98 x $10^{12}$ $cm^{-2}$ suggests an attack of $O^{5+}$ ions on the aromatic C-H/C-C and carbonate groups even at low dose unlike $O^{3+}$ ions.

From the two different species and three different charge state ion irradiations i.e., ($O^{3+}$,$O^{5+}$ and $Ar^{8+}$), it can also be concluded that the C-O bond intensity saturates approximately at 15 % which is in agreement with the results from singly charged ion irradiation in the presence of oxygen gas flow[98, 103]. With the HCI irradiations it can be concluded that the presence of oxygen gas in the chamber is not necessary and that similar irradiation results can be achieved at much lower doses compared to singly charged ion irradiations.

### 5.3.3 Potential Energy Dependent Results

**C-C Bond Intensity:**

The relative intensities of C-C, C-O C=O and ($\pi - \pi$) bonds of a pristine PC sample and of PC samples irradiated with $O^{3+}$,$O^{5+}$ and $Ar^{8+}$ are shown in Table 5.3. From Fig. 5.8, a clear charge state or potential energy dependent bond intensity can be observed. The $O^{3+}$ ion has the lowest potential energy(102 eV) of the three ions, and the decrease in the C-C bond intensity of PC irradiated with $O^{3+}$ is less than that of $O^{5+}$ and $Ar^{8+}$ ion beams for a fluence of $\approx$ 5 x $10^{12}$ $cm^{-2}$. We expect to observe a similar trend to that of $O^{3+}$ ion irradiation if the irradiations were performed at higher doses of $O^{5+}$ and $Ar^{8+}$ ion beams out to a fluence of $\sim$ 1 x $10^{13}$ $cm^{-2}$. It is interesting to note that polycarbonate samples irradiated with $Ar^{8+}$ beams with a fluence of $\approx$ 4.25 x $10^{12}$ $cm^{-2}$ had a higher decrease in the C-C bond intensity compared to that of $O^{3+}$ and $O^{5+}$ beams. The C-C bond intensity decreased to 73.34 %, 73.14 % and 73.91 % for the polycarbonate samples irradiated with $O^{3+}$, $O^{5+}$

| Dose ($cm^{-2}$) | Charge State q | C-C | C-O | C=0 | $(\pi - \pi)$ |
|---|---|---|---|---|---|
| 0 | | 92.38 | 3.65 | 3.96 | 0 |
| 6.56 x $10^{12}$ | $O^{3+}$ | 80.14 | 12.20 | 7.63 | 0 |
| 1.22 x $10^{13}$ | $O^{3+}$ | 73.34 | 14.65 | 12.20 | 0 |
| 1.98 x $10^{12}$ | $O^{5+}$ | 77.1 | 10.0 | 8.35 | 4.48 |
| 4.95 x $10^{12}$ | $O^{5+}$ | 72.91 | 14.92 | 8.74 | 3.15 |
| 1.41 x $10^{12}$ | $Ar^{8+}$ | 76.38 | 9.73 | 8.81 | 5.04 |
| 2.83 x $10^{12}$ | $Ar^{8+}$ | 73.81 | 13.75 | 9.31 | 3.12 |
| 4.24 x $10^{12}$ | $Ar^{8+}$ | 73.63 | 14.40 | 8.65 | 3.08 |

Table 5.3: Relative Intensities of C-C, C-O and C=0 bonds of pristine and HCI treated PC. Each entry represents the relative integrated intensity of the given peak in the measured and fit XPS spectrum.

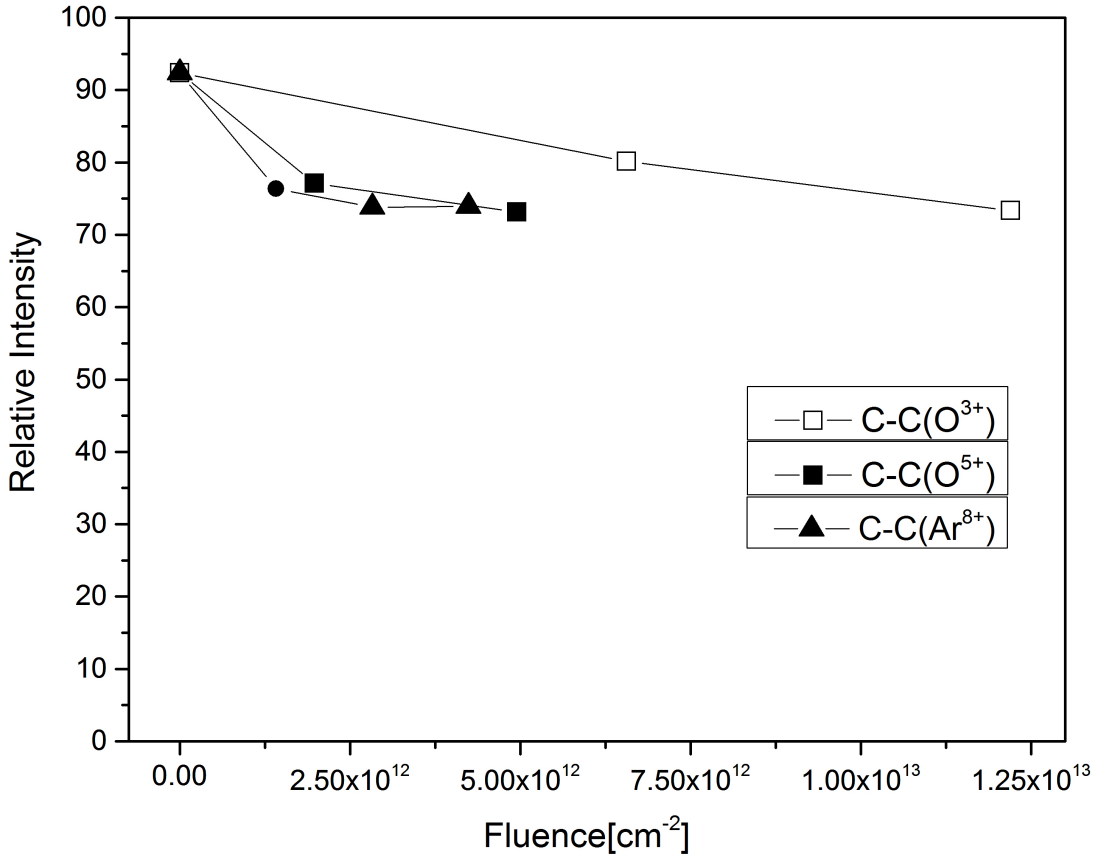


Figure 5.8: Relative intensities of C-C bonds of PC irradiated with $O^{3+}$,$O^{5+}$ and $Ar^{8+}$ ion beams.

and $Ar^{8+}$ ion beams, respectively. The trend suggests that the C-C bond intensity saturates at $\sim 73.0\%$.

This potential energy dependent decrease in the C-C bond intensity clearly indicates that when HCIs approach the surface, the potential energy of the ion is deposited on the surface in a nanometer sized area. Therefore of the various processes that can occur during the neutralization of HCIs, a fraction of the potential energy must be utilized for the initiation of bond breaking.

**C-O Bond Intensity:**

An increase in the C-O bond intensity of polymer surfaces is crucial for many of their potential applications such as wettability, adhesive substrates for thin film growth, etc. There have been several efforts in the past to increase the C-O bond intensity by ion irradiation, UV, X-ray and chemical methods[95–97, 99, 115]. Detailed peak intensities of polycarbonate samples irradiated with $O^{3+}$,$O^{5+}$ and $Ar^{8+}$ ion beams are listed in Table 5.2 and the bond intensities are condensed to C-C, C-O and C=0 bonds in Table 5.3. We can clearly see a charge state or potential energy dependent increase in the C-O bond intensity shown in Fig. 5.8. At an ion dose of $\approx$ 5 x $10^{12}$ $cm^{-2}$ the increase in the C-O bond intensity is higher for the polycarbonate samples irradiated with $Ar^{8+}$ followed by $O^{5+}$ and $O^{3+}$ ion beams. The C-O bond intensity increases to 14.65 %, 14.92 % and 14.40 % for the polycarbonate samples irradiated with $O^{3+}$,$O^{5+}$ and $Ar^{8+}$ ion beams. The trend suggests that the C-O bond intensity saturates at $\sim$ 14.0%

This potential energy dependent increase in the C-O bond intensity indicates clearly that a fraction of the potential energy of HCI ions during the neutralization process is utilized for C-O bond formation. From Fig. 5.8 and Fig. 5.9 it is evident that the potential energy possessed by HCIs is utilized for two activities. A fraction of the potential energy is used to initiate the bond breakage of C-C bonds, and these broken C-C bonds are reactive and tend to achieve stability by bonding with the oxygen atoms present in the chamber. The required energy for the C-O bond formation is supplied by the HCIs. So, it can be concluded that HCIs not only induce the bond breakage of C-C bonds, but also initiate the C-O bond formation even in the absence of oxygen gas flow across the sample.

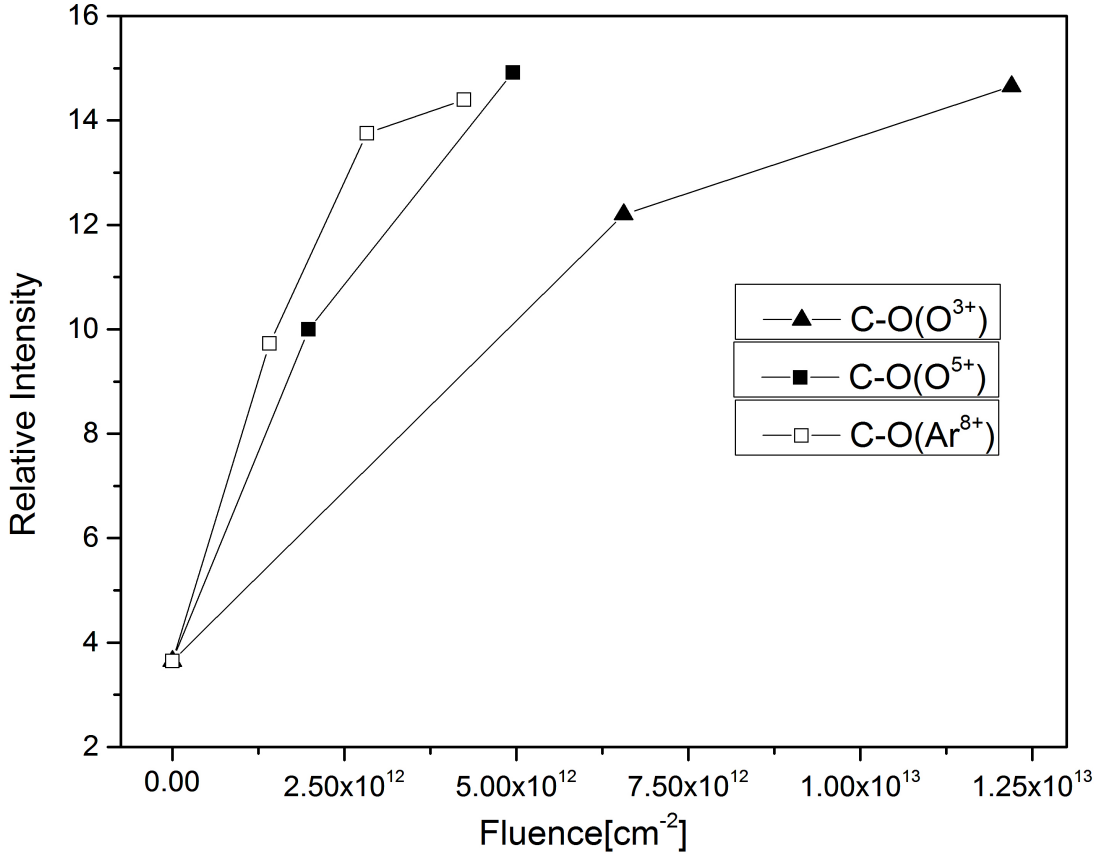


Figure 5.9: Relative intensities of C-O bonds of PC irradiated with $O^{3+}$,$O^{5+}$ and $Ar^{8+}$ ion beams.

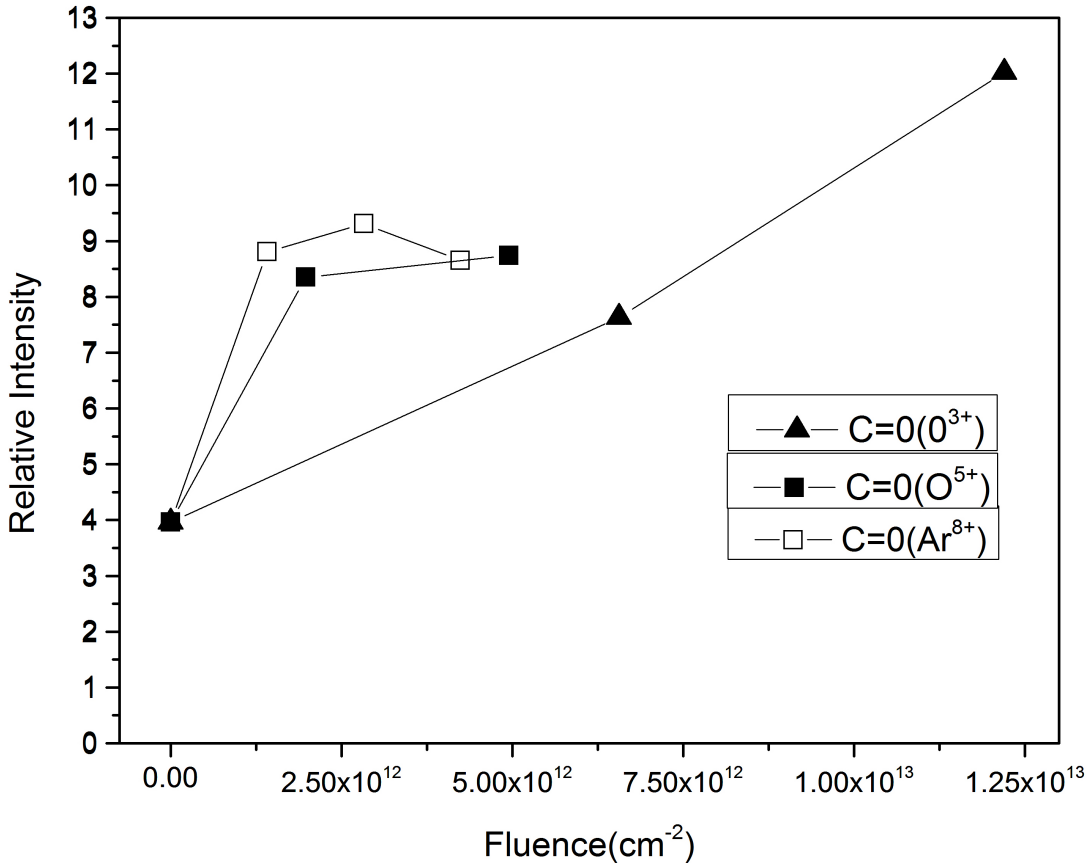


Figure 5.10: Relative intensities of C=O bonds of PC irradiated with $O^{3+}$,$O^{5+}$ and $Ar^{8+}$ ion beams.

**C=O Bond Intensity:**

The C=O bond intensities of pristine and HCI irradiated PC samples with $O^{3+}$,$O^{5+}$ and $Ar^{8+}$ ion beams are listed in Table 5.3. The increase in the C=O bond intensity clearly suggests a charge dependent trend in the formation of the C=O bond. From Fig. 5.10 it is clearly evident that at an ion dose of $\sim$ 5 x $10^{12}$ $cm^{-2}$, the increase in the intensity of the C=O bond is high for polycarbonate samples irradiated with $Ar^{8+}$ ion beams followed by $O^{3+}$ and $O^{5+}$ ion beams.

The C=O bond intensity increases to 12.02 %, 8.74 % and 9.05 % for the polycarbonate samples irradiated with $O^{3+}$,$O^{5+}$ and $Ar^{8+}$ ion beams. The high in-

crease in the C=O bond intensity for polycarbonate samples irradiated with $O^{3+}$ ion beams is attributed to the absence of $\pi - \pi$ satellite peaks. The discrete shake up $(\pi - \pi)$ satellite peaks at 291.3 eV and 292.5 eV arise due to the attack by HCIs on aromatic C-H/C-C (benzene ring) and carbonate(C=O group). The presence of $\pi - \pi$ peaks only for polycarbonate samples irradiated with $O^{5+}$ and $Ar^{8+}$ ion beams and the absence in the case of an $O^{3+}$ ion irradiated samples indicates the absence of an $O^{3+}$ attack on aromatic C-H/C-C and carbonate groups. Since the energy required to attack aromatic C-C (benzene ring) and initiate $\pi - \pi$ bond transition is large, we assume that the $O^{3+}$ ion, possessing only 102 eV potential energy is not able to initiate the reaction.

**Summary**

The average relative intensities of C-C, C-O, C=O bonds with potential energy is shown in Fig. 5.11. Corresponding data is shown in Table 5.3. A clear charge state dependent change in the bond intensity can be seen in Fig. 5.10. The trend suggests that the C-C, C-O bond percentage saturates at $\sim 75\%$ and $\sim 14$ % which is similar quantitatively to the experiments with singly charged ions [91, 98, 100, 104, 113]. The ion fluences used in our experiment are in the range of $10^{12}$ - $10^{13}$ $cm^{-2}$ which are three orders of magnitude ($10^{15}$- $10^{16}$ $cm^{-2}$) lower than the doses used in previous studies with singly charged ions.

### 5.3.4 Q-Dependent Results and Gamma Factor Calculations

In this section the Q-dependence of C-C bond breaking and C-O bond formation is discussed. As seen in Fig. 5.9, the percentage of aromatic C-O bond intensity in an XPS spectrum depends on the irradiated fluence and charge state. For a first order calculation, we can assume the curves to be locally linear with respect to dose

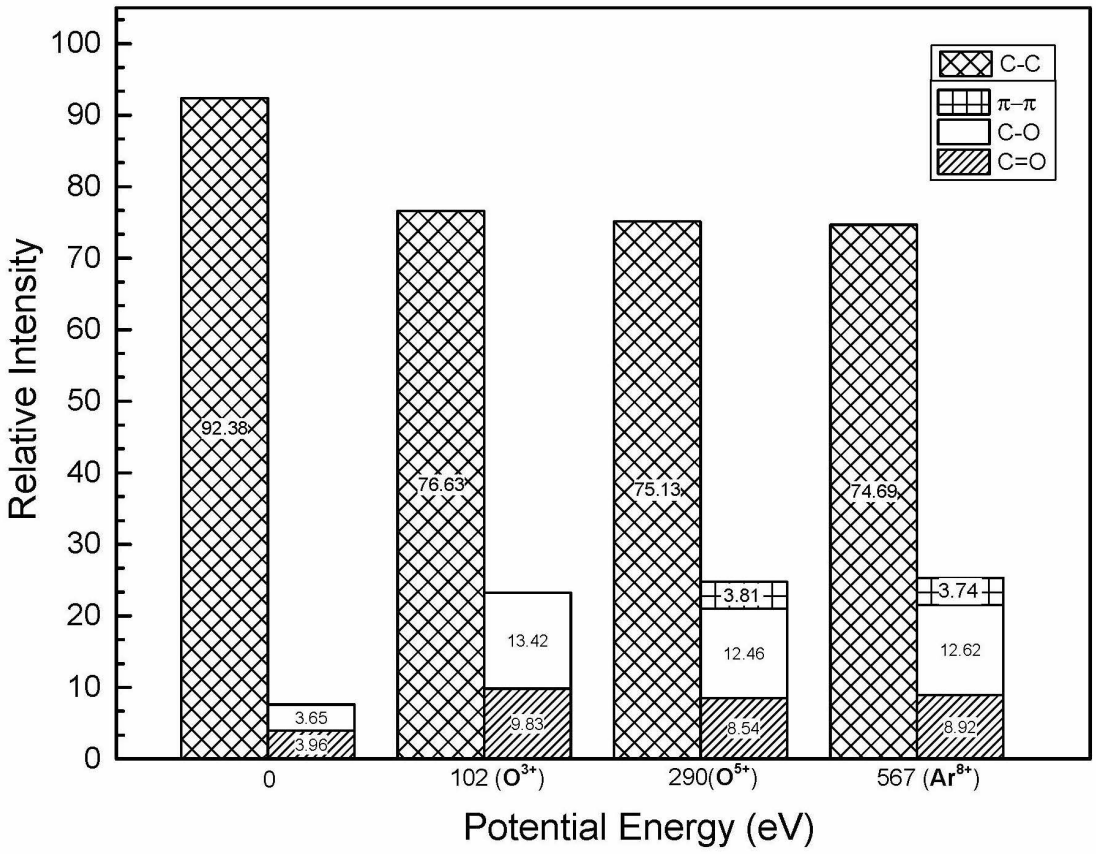


Figure 5.11: Relative intensities of C-C, C-O, C=O bonds with potential energy.

and calculate a slope using the pristine point as a reference for point corresponding to zero dose. This calculation is indicative of a "per-ion effect" that is monotonically increasing for each charge state, where the measured effect is aromatic C-O bond formation at the surface. As additional carbon-oxygen bond formation is a consequence of the bonds broken by the highly charged ion irradiation, the calculated slopes are proportional to the number of bonds broken per ion for each charge state. As shown in the Fig. 5.12, a Q-dependent enhancement is observed for C-O bond breaking at the polycarbonate surface due to highly charged ions with the efficiency of bond breaking scaling with $Q^{1.7}$. Similarly, Q-dependent enhancement is observed for the C-O bond formation at the polycarbonate surface with $Q^{1.8}$ as shown in Fig. 5.13.

The enhancement in irradiation-related surface effects like bond breaking using HCIs can partly be explained by an increased area of interaction with the surface. The interaction of a surface with the HCI begins a few Å above the surface. The Coulombic attractive well of the incoming highly charged ion leads to electron capture from the surface, effectively breaking bonds present at the surface. The interaction volume can be modeled by a sphere centered around the HCI with radius $R_c$ being the minimum distance at which the first electron is captured from the target by the HCI. This $R_c$ in the limiting case of a metal, is given by the classical over the barrier model in atomic units as [83]

$$R_c = \sqrt{2Q}/W \tag{5.1}$$

While this equation changes depending on the dielectric permittivity of the target material, it is instructive to investigate the effect of the volume of interaction of the HCI with the target approximating the target as a metal for a first order calculation. Using the work function for PC as ∼4.26 eV from [116] and choosing $Q = 8$ for illustrative purposes, we calculate the critical radius as $R_c = 25$ a.u. This sphere

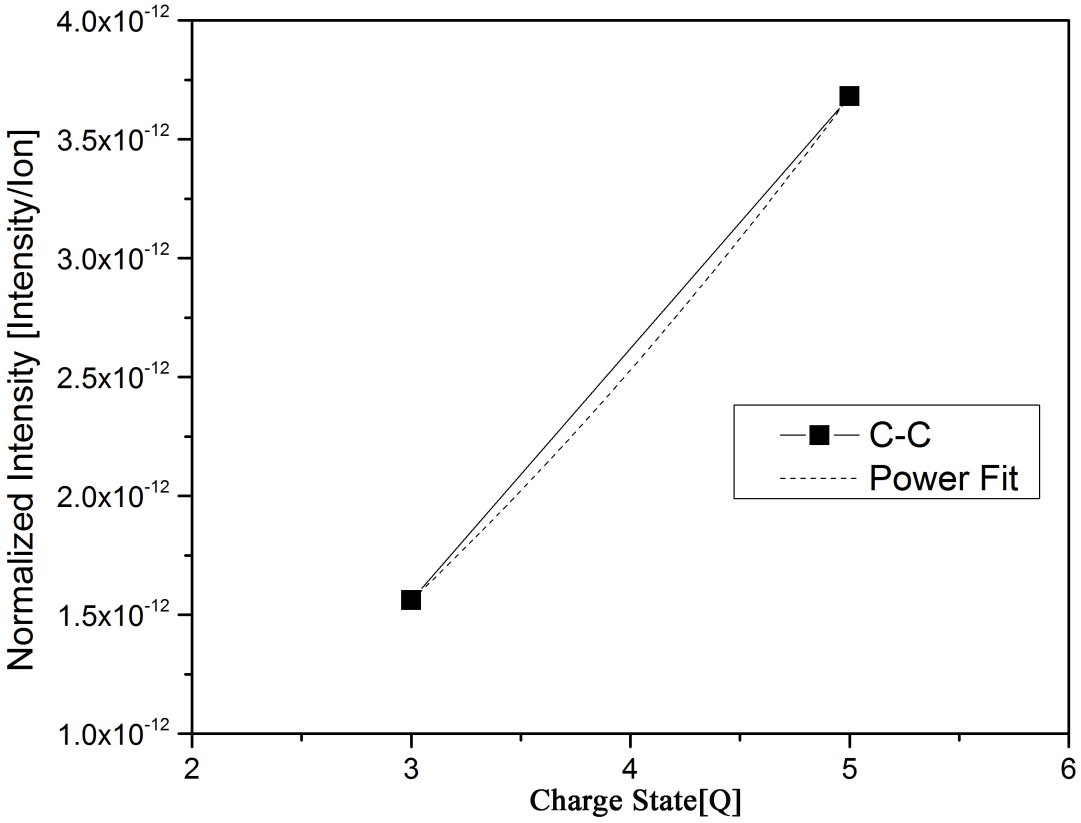


Figure 5.12: Normalized intensity of C-C bonds with charge state of PC irradiated with $O^{3+}$ and $O^{5+}$ ion beams.

representing the interaction volume is centered at the location of the HCI, and is translating with the velocity of the ion. As the ion approaches the target surface, the effective surface area of the target that the HCI is interacting with is the cross-section of the sphere intersecting with the plane of the surface. The velocity of the ion calculated for a kinetic energy of 1 keV is $v = 3.2 \times 10^{-2}$a.u. This velocity will be higher than calculated due to image charge accelerating the ion towards the surface, but typical values lead to an increase in kinetic energy around $\sim$ 50eV, which can be ignored for this first order calculation. As the HCI approaches the surface, the interaction effectively begins when the ion is at a distance of $R_c$ from the surface. At this point, the region of the surface interacting with the ion is only a single point.

The area of interaction at a time $t$ after the ion-surface distance is smaller than $R_c$ is given by

$$A_{eff} = \pi(2R_c vt - v^2 t^2) \tag{5.2}$$

As the sphere passes the plane, the area of interaction with the surface increases until it reaches a maximum, when the HCI has reached the surface, and then decreases again as the HCI passes into the surface. The maximum area of interaction, when the HCI has reached the surface, takes $\sim$ 20 fs since the beginning of its interaction with the surface for the parameters used here. As can be seen, for a fixed kinetic energy, the maximum area of interaction is a circle with radius $R_c$, and $R_c$ depends on $\sqrt{Q}$, leading to a linear dependence of the maximum area of interaction with the charge state Q.

As an example of another system where Q-enhanced bond breaking at the surface has been observed and quantified is the HCI-induced enhanced desorption of hydrogen from a hydrogen-passivated silicon surface[88, 117]. The Q-effect was derived as a fit to a power law of the form $\sim Q^{\gamma}$ in the H-Si system, resulting in a

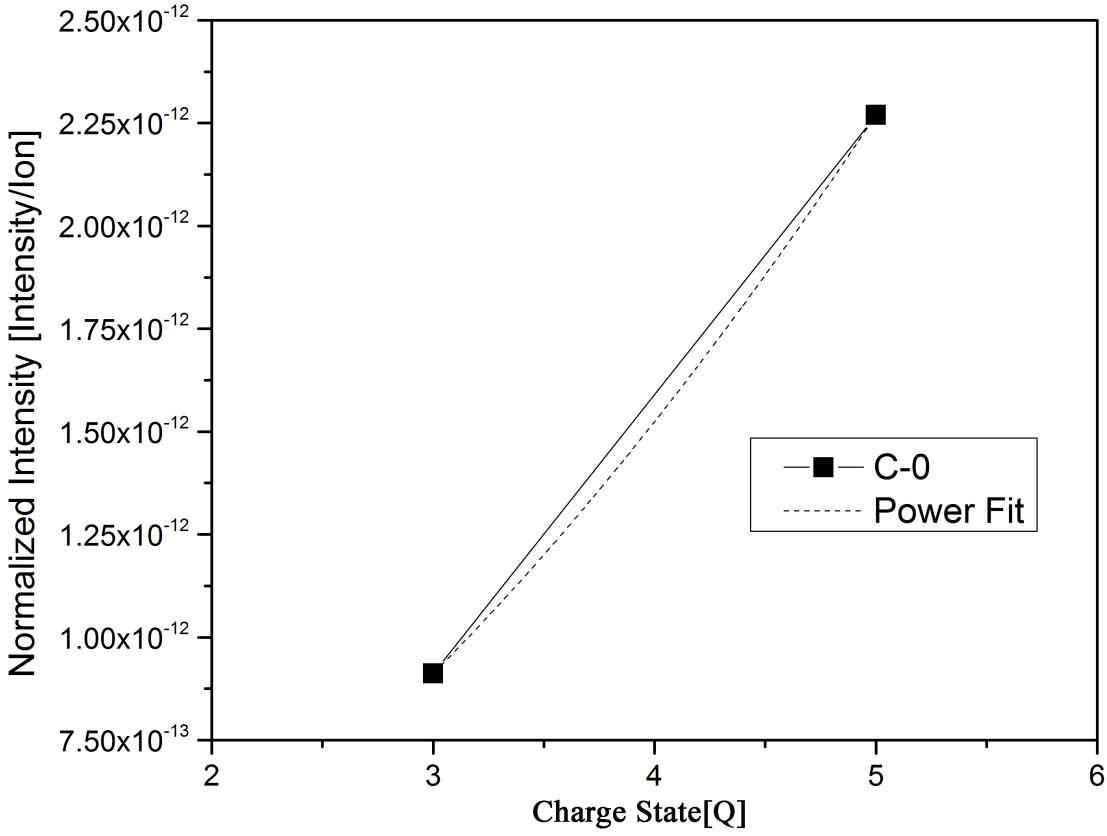


Figure 5.13: Normalized intensity of C-O bonds with charge state of PC irradiated with $O^{3+}$ and $O^{5+}$ ion beams.

$\gamma \sim 4$. The $\gamma$ factor for multiply charged ion induced bond breaking on polycarbonate is not restricted to the measurement quoted here as there may not be a direct lossless correspondence between the dose delivered and the quantified characterization. For our experiment, we did not have oxygen gas blowing across the sample like other experiments involving singly charged ions, yet a comparable increase in the peaks corresponding to carbon-oxygen bonds was measured in the XPS spectra. The low probability for serendipitous replacement of these broken bonds with an oxygen atom as compared to blowing oxygen across the face of the sample can be a high loss channel restricting the calculated $\gamma$ factor to 1.7.

# Chapter 6

# Conclusions and Future work

## 6.1 Conclusions

The research presented in this thesis has focused on three projects. In these the growth and characterization of $Cu_3Si$ nanostructures using reactive deposition epitaxy (RDE) and highly charged ion(HCI) assisted growth techniques was demonstrated. The $Cu_3Si$ nanostructures grown by these two techniques were investigated and compared. The surface modification of polycarbonate(PC) using HCIs was also discussed.

1. Growth of self assembled epitaxial $Cu_3Si$ islands on silicon substrates using the reactive deposition epitaxy(RDE) technique. In this work the underlying causes for the growth of $Cu_3Si$ islands were investigated.

    - $SiO_2$/Si substrates were annealed at 500°C to facilitate void growth at the $SiO_2$/Si interface. Cu was deposited on the annealed samples at varying temperatures and deposition times to initiate the growth of $Cu_3Si$ islands. Optimum temperatures for the growth of $Cu_3Si$ islands was determined.

Growth mechanism of the $Cu_3Si$ islands was identified to be defect assisted.

- Temperature and time dependent growth kinetics were investigated. Activation energies for the growth of $Cu_3Si$ islands on $SiO_2$/Si substrates of (111) and (100) orientations with p and n type dopants were determined from temperature dependent growth kinetics.
- Growth kinetics of $Cu_3Si$ islands was determined to be influenced by a diffusion control mechanism.
- Time dependent growth kinetics was studied to understand the evolution in the shapes of $Cu_3Si$ islands. Shape transition from rectangular to trapezoidal on n-Si(111) and from square to nanowire on p-Si(111) and p-Si(100) substrates was observed. Shape evolution of the $Cu_3Si$ islands are influenced by the strain and results were explained in terms of strain induced shape transition model.
- Differences in the lengths of $Cu_3Si$ nanowires grown on Si(111) and Si(100) substrates were attributed to the difference in the dangling bonds present at the $SiO_2$/Si interface.
- Epitaxial relations of the $Cu_3Si$ islands with Si substrates were determined.

2. Nanopattering of $Cu_3Si$ islands on silicon substrates using highly charged ion beams and identification of their growth behavior and dynamics. In this project HCI induced growth kinetics of $Cu_3Si$ islands was investigated.

    - $SiO_2$/Si substrates were irradiated with highly charged ion beams (HCIs) of argon with varying charge states and fluences to initiate the void growth on the surface. Cu was deposited at 600°C to facilitate the growth of $Cu_3Si$ islands. Potential energy(charge state) and ion fluence dependent growth

kinetics of $Cu_3Si$ on $SiO_2$/Si(111) and $SiO_2$/Si(100) substrates with p type dopants at 600°C was investigated.

- A linear increase in the density of the $Cu_3Si$ islands with charge state and fluence was observed. This is attributed to the HCI induced nucleation of the voids on the surface of the substrates. A potential energy(q) effect was derived as a fit to a power law of the form $\sim q^{\gamma}$ in the $SiO_2$/Si system, resulting in a $\gamma \sim 0.95$.
- Dependence of the $Cu_3Si$ islands dimensions on charge state and ion fluence at 600°C was measured. The observed islands were longer compared to RDE grown islands, which is attributed to the HCI induced void growth mechanism.
- A shape transition from square to nanowire on p-Si(111) and p-Si(100) substrates was observed. Shape evolution of the $Cu_3Si$ islands are influenced by the strain and results were explained in the light of the strain induced shape transition model.
- The epitaxial relations of the $Cu_3Si$ islands with Si substrates were determined.

3. Surface modification of polycarbonate using highly charged ion beams.

- Polycarbonate (PC, Lexan) was irradiated with HCIs of argon and oxygen with varying charge states and ion fluences to modify the surface properties.
- The basic PC molecular structure consisted of C-C, C-O and C=0 bonds with relative intensities of 93%, 3.96% and 3.64%, respectively. The potential energy(charge state) and the ion fluence dependent change in the

relative intensities of C-C, C-O and C=0 bonds was investigated.

- A nonlinear decrease in the relative intensity of the C-C bonds and an increase in the intensities of the C-O and C=O bonds with charge state and ion fluence was observed. This effect is attributed to the HCI induced chain scission and cross-linking mechanisms promoted at the surface due to the HCI-polymer interaction. Chain scission induces breaking of the polymer chains at the surface and the broken nonvolatile bonds join to form a stable configuration by undergoing cross-linking.
- The observed q-enhanced C-C bond breaking and C-O bond formation at the surface was fit to a power law of the form $\sim q^{\gamma}$ in the PC system, resulting in a $\gamma \sim 1.7$.
- A saturation in the bond intensities of the C-O and C=0 bonds at 14% and 10%, respectively with charge state and fluence was observed which is similar quantitatively to measurements made with singly charged ion beams.
- HCI induced modification is more efficient compared to the singly charged irradiation experiments for two reasons: (1) The ion fluences used in our experiment are in the range of $10^{13}$ cm$^{-2}$ compared to that of singly charged experiments fluences $10^{16}$ cm$^{-2}$. (2) The absence of oxygen gas flow across the sample during the experiment unlike that of singly charged ion beam experiments.

## 6.2 Proposals for Future Experiments

Much of the work discussed in this thesis is the growth and characterization of self assembled epitaxial $Cu_3Si$ nanostructures using the e-beam evaporation method in UHV. The main limitations of the experimental work in this thesis is failure to estimate the resistivity of the $Cu_3Si$ nanowires and also the percentage of Si consumed by the $Cu_3Si$ nanostructures. These measurements were limited by the vast requirement of TEM work. Furthermore, TEM specimen preparation by a focussed ion beam(FIB) will take several hours and is prone to contamination during milling. The following recommendations are proposed for future study.

1. Investigate the device applicability of the $Cu_3Si$ nanostructures. The data obtained from this thesis work can be used to assist in the application of $Cu_3Si$ nanowires, e.g. electrodes in Li-ion battery application. However, $Cu_3Si$ is catalytic even at room temperature and would require a capping layer/barrier for the $Cu_3Si$ nanostructures to avoid oxidation. Graphene has been demonstrated to protect Ni-Si, Co-Si, and Fe-Si silicides from oxidation[118]. Hence, a proposed future work project is to grow graphene on the $Cu_3Si$ nanostructures.

2. Investigate the percentage of Si consumed by the $Cu_3Si$ nanostructures with deposition time/thickness. As the dimensions of the smallest feature on the integrated circuits and memory devices shrinks, the percentage of Si consumed by the silicides is important for potential applications such as contacts. The high percentage of Si consumption by silicides is not desirable for various reasons such as degradation of devices and leakage currents. Hence, a proposed future work is to prepare TEM specimens with a FIB and perform TEM analysis to find the percentage of Si consumption.

3. Investigate the resistivity of $Cu_3Si$ nanowires as a function of deposition thickness. Generally, silicides are used as a contact to source, drain and gate terminals in integrated circuits to reduce the contact resistance. $Cu_3Si$ is considered to be a potential candidate for future contact applications for various reasons such as low resistivity, low RC delay and low electromigration of Cu. Hence, a proposed future work is to perform the electrical resistivity measurements of $Cu_3Si$ nanowires with a four point probe method and with scanning tunneling microscope(STM).

4. Investigate time dependent growth kinetics of $Cu_3Si$ nanostructures on HCI irradiated $SiO_2$/Si substrates. Time dependent data is important to understand the shape evolution and growth morphology of $Cu_3Si$ nanostructures with time. Hence, a proposed future work is to irradiate $SiO_2$/Si with HCI beams of varying charge state and fluence. Deposition of Cu at elevated temperatures of varying deposition times/ thickness will lead to the growth of $Cu_3Si$ islands of varying dimensions and shapes.

5. Investigate the growth kinetics of $Cu_3Si$ nanostructures on HCI irradiated Si substrates. Silicon is the most commonly found substrate in integrated circuits and memory devices. So, it is important to understand the growth morphology of $Cu_3Si$ nanostructures on HCI irradiated Si substrates. The data obtained from this thesis work can be used to understand the role of $SiO_2$ in the growth morphology and kinetics of $Cu_3Si$ nanostructures. Hence, a proposed future work is to irradiate silicon substrates with HCI beams of varying charge states and fluences. Deposition of Cu at elevated temperatures on HCI irradiated Si substrates could lead to the growth of $Cu_3Si$ islands.

6. Investigate the possibility of extending HCI facilitated growth of metal silicides

to other systems such as Ni-Si, Co-Si, and Fe-Si. Currently, Ni-Si is used as a contact in integrated circuits[1, 2], and Co-Si and Fe-Si are used as contacts in memory devices[4, 5, 8, 119, 120]. Hence, a proposed future work is to irradiate silicon substrates with HCI beams of varying charge state and fluence, and determine if the deposition of metals such as Ni, Co and Fe at elevated temperatures could lead to the growth of Ni-Si, Co-Si, and Fe-Si silicides.

7. Investigate the possibility of using HCI modified polymer surfaces as a substrate material for optical lenses and display panels. The data from this thesis indicates that HCI irradiation has made PC more hydrophilic which is one of the major requirements of adhesive substrates for thin film growth. Hence, a proposed future work is to deposit antireflection coatings such as $TiO_2$ on the HCI modified PC substrates. The optical transmittance and reflectance spectra could reveal the possibility of utilizing HCI modified PC substrates for such applications.

# Appendices

# Appendix A Image Analysis of SEM Images with Matlab

Image analysis involves processing an image into fundamental components in order to extract statistical data. Image analysis of SEM images in this thesis included finding the dimensions (length, width, area) and density of the $Cu_3Si$ nanostructures.

The steps involved in the image processing of SEM images are listed below.

1. Open/read the image file that needs to be processed. Fig. A.1 and Fig. A.2 show the SEM images of $Cu_3Si$ nanostructures deposited on $SiO_2$/n-Si(111) and $SiO_2$/p-Si(111) at 600°C. Image analysis is performed on two different shaped $Cu_3Si$ nanostructures, i.e triangular and nanowire to extract statistical data.

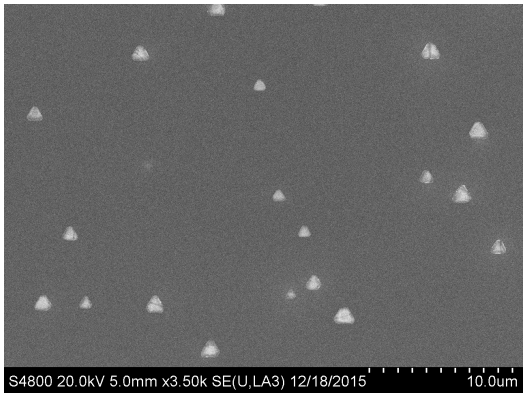


Figure A.1: SEM image of $Cu_3Si$ nanostructures deposited on $SiO_2$/n-Si(111) at 600°C.

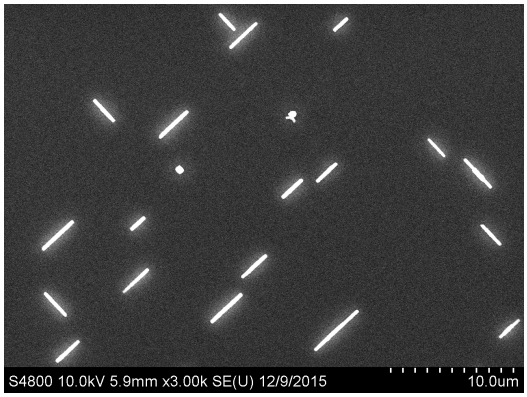


Figure A.2: SEM image of $Cu_3Si$ nanostructures deposited on $SiO_2$/p-Si(111) at 600°C.

2. Crop the label bar present at the bottom of the SEM image. Cropped images are shown in Fig. A.3 and Fig. A.4.

3. Convert grayscale (RGB) image to binary image. A global threshold value (level) is calculated for each image. Level can also be manually specified in the

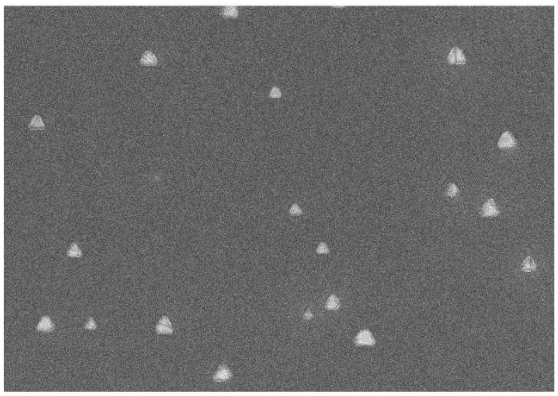

Figure A.3: Cropped SEM image without labels in Fig. 1.

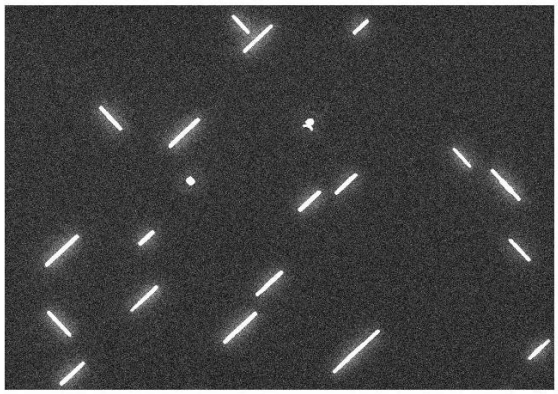

Figure A.4: Cropped SEM image without labels in Fig. 2.

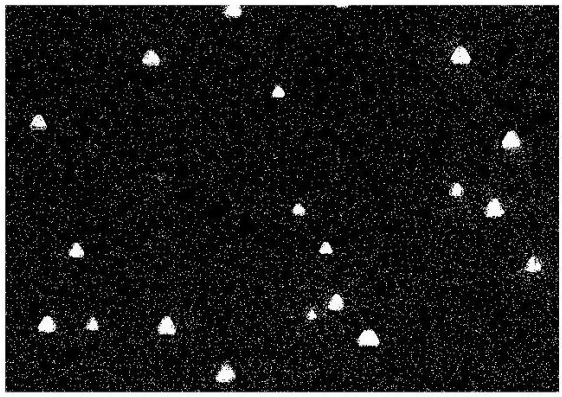

Figure A.5: Binary image of Fig. 3.

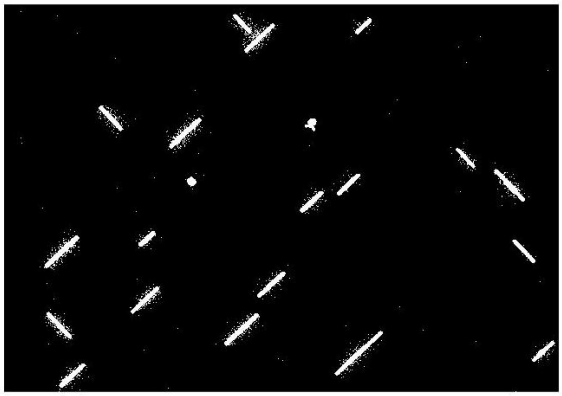

Figure A.6: Binary image of Fig. 4.

range [0,1]. All pixels in the input image with a luminance greater than level are replaced with value 1 (white) and all other pixels with the value 0 (black). Binary images of Fig. A.3 and Fig. A.4 are shown in Fig. A.5 and Fig. A.6

4. Remove the noise. This step is intended to remove small irregular shaped objects present in the image. This is generally achieved by removing all the objects that are below the specified size. Fig. A.7 and Fig. A.8 show the processed images after removing noise objects from Fig. A.5 and Fig. A.6.

5. Smoothen the boundaries of the objects. This is performed by applying con-

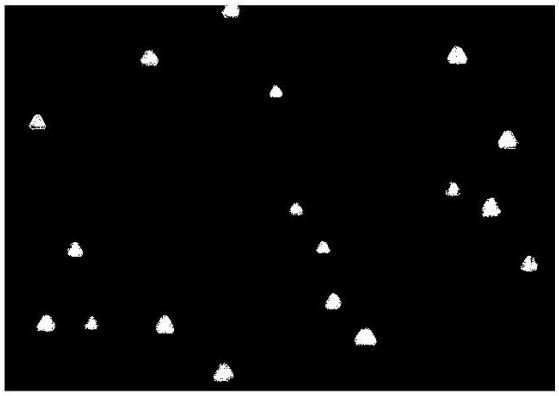

Figure A.7: After removing noise objects from Fig.5.

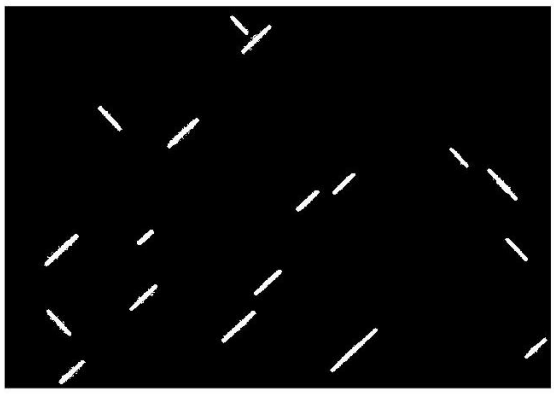

Figure A.8: After removing noise objects from Fig.6.

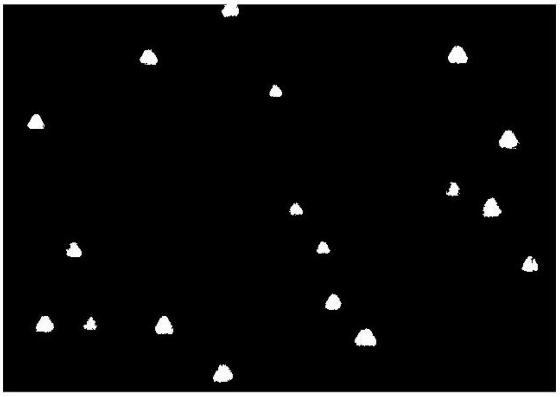

Figure A.9: After erode and dilation operation on Fig.7 .

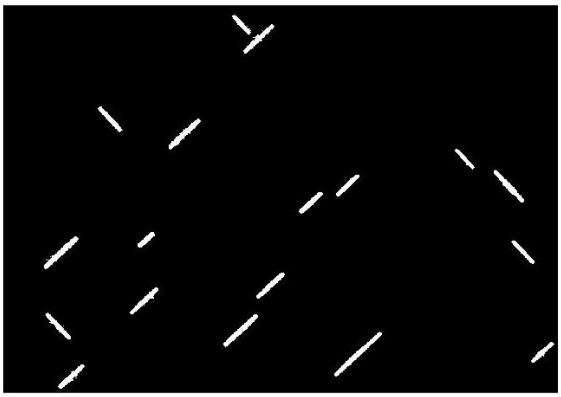

Figure A.10: After erode and dilation operation on Fig.8.

secutive erode and dilate functions. Erode thins the object border and removes noise along the edges of the object. Dilation broadens the objects borders to the actual dimensions. By performing erode and dilation consecutively the original dimensions of the objects are restored. The resultant images after performing consecutive erode and dilute operations on Fig. A.7 and Fig. A.8. are shown in Fig. A.9 and Fig. A.10.

6. Delete any noise that may have arisen due to erode and dilation operations. This is a repetition of step 4. Fig. A.11 and Fig. A.12 corresponds to Fig. A.9

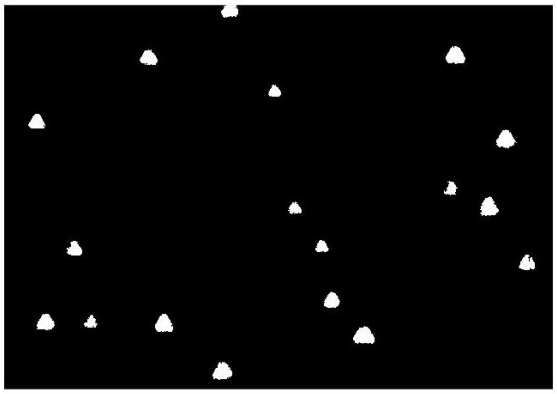

Figure A.11: After removing the noise from Fig. 9.

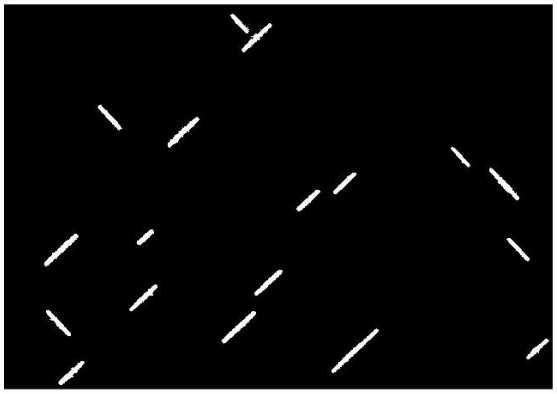

Figure A.12: After removing the noise from Fig. 10.

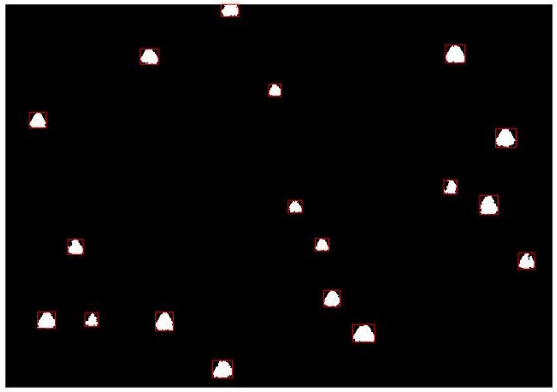

Figure A.13: Fig.11 with bounding boxes around the objects

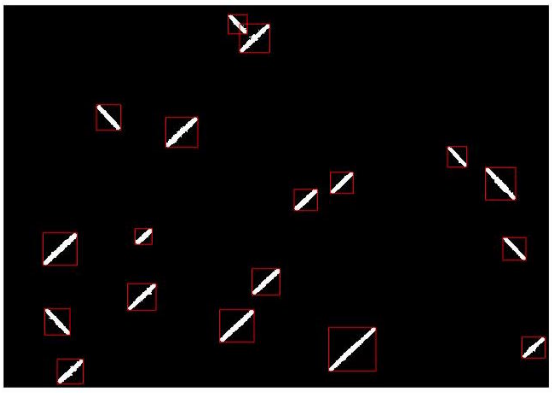

Figure A.14: Fig.12 with bounding boxes around the objects

and Fig. A.10 after removing noise objects.

7. Draw the bounding box around each object. Color of the bounding box is selected to be red to clearly differentiate the boundary. Bounding box drawn around each object in Fig. A.11 and Fig. A.12 are shown in Fig. A.13 and Fig. A.14.

8. Extract the properties of the bounding box using regionprops function in Matlab. Regionprops measures the properties of image regions. Several properties such as dimensions of the bounding box, filled area, perimeter and centroid can

be extracted for each object.

9. Determine the number of objects present in each image.

    - Density of nanostructures = Number of objects in each image/ Image area.

10. Length, width and area of the nanowires were computed for all the objects.

    - Length of the nanowire = length of diagonal of bounding box
    - Area of the nanowires = Filled area inside the bounding box, i.e area of the white pixels.
    - Width of the nanowire = Area/length

11. Length and area of the triangles were computed.

    - Area of triangular nanostructure= Filled area inside the bounding box
    - Approximating the triangle to equilateral then Area would be

$$A = \frac{\sqrt{3}l^2}{4} \tag{1}$$

      Where $A$ is the area of the equilateral triangle and $l$ is the length of the side of a triangle.

    - Length of triangular nanostructure= length of equilateral triangle
    - Length is also computed by determining the length of bounding box around the object.

12. All the extracted statistical data is in terms of pixel length, pixel width and pixel area.

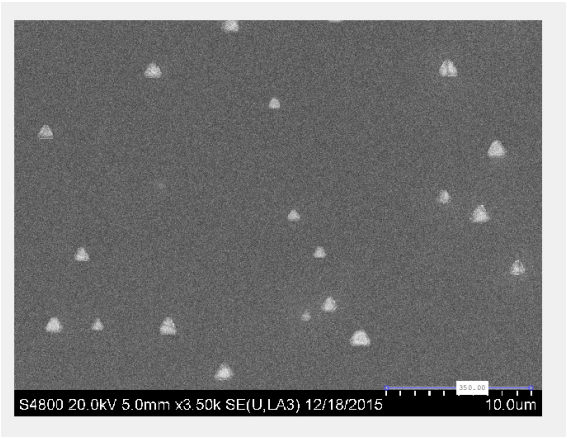


Figure A.15: Pixel and actual dimensions of Fig.1

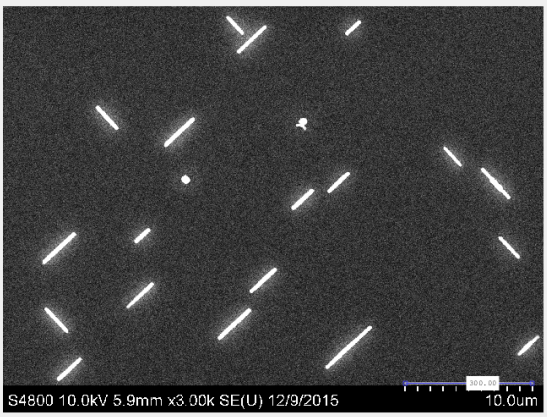


Figure A.16: Pixel and actual dimensions of Fig.2

13. Calibrate pixel data to actual dimensions of the image. Images with pixel dimensions converted to real dimensions are shown in Fig. A.15 and Fig. A.16.

14. Conversion of pixel data to real data is performed by following below procedure

    - From Fig. A.16: Length of 300 pixels = 10000 nm
    - Length of 1 pixel = 10000/300 = 33.33 nm
    - Assuming pixel to be of square: Area of pixel = 1111 $nm^2$

15. Convert length, width and area of objects in pixels to nanometers(nm)

    - Length of each object = length of object in pixels x length of 1 pixel in nm
    - Width of each object = width of object in pixels x width of 1 pixel in nm
    - Area of each object = Area of object in pixels x Area of 1 pixel in $nm^2$

16. Finally average length, width and area of objects in an image is computed

    - Total length = Sum of lengths of all objects

- Total width = Sum of widths of all objects
- Total area = Sum of Areas of all objects
- Average Length = Total length/ Density
- Average Width = Total width/Density
- Average Area = Total Area/Density

## A.1 Matlab Code

```
clear all;
%Enter full path of folder containing images here followed by '/'
path='images/';% if its in matlab document folder
fileId = fopen('data.txt','w'); % open the file into which the
                                    output needs to be written

%Enter minimum size of region that is considered as long wire
pixelThresh = 500; % All the objects smaller than this size will
% be removed
%(pixelThresh differentiates between long wires and short wires)

imageFiles = dir(strcat(path,'*.TIF'));
numOfFiles = length(imageFiles);
% Number of files/images found in a folder/directory

sumLength = 0;
sumWidth = 0;
sumArea = 0;
%avgCounter = 0;
close all;
for iterator = 1:numOfFiles
   sumLength = 0;
   sumWidth = 0;
   currentFileName = imageFiles(iterator).name;
   imageFullPath=strcat(path,currentFileName);
   currentImage = imread(imageFullPath);

   % Cropping the label bar present at the bottom of images
```

```
dimensions=size(currentImage);
currentImage = imcrop(currentImage,[0 0 dimensions(2)
                                    dimensions(1)-65]);
%imcrop returns the values of (start position, width, height)
figure, imshow(currentImage);

%thresholding images to binary
bwImage = im2bw(currentImage);
 figure, imshow(bwImage);

%Delete all noise
%(small particles less than 'pixelThresh' pixels big)
bwImage = bwareaopen(bwImage,pixelThresh,4);
% bwareopen removes all components that has fewer
% than pixelthresh pixels
figure, imshow(bwImage);

%fill holes in regions
bwImage = imfill(bwImage,'holes');
% some wires have holes in middle. Those holes are filled
figure, imshow(bwImage);

%smooth boundaries of regions
 thinnedImage = imerode(bwImage,strel('square',2));
 dilatedImage = imdilate(thinnedImage,strel('square',2));
 figure, imshow(thinnedImage);
 figure, imshow(dilatedImage);

%Delete all noise
%(small particles less than 'pixelThresh' pixels big)
 % again due to broken pieces resulting from above processing
```

```
dilatedImage = bwareaopen(dilatedImage,pixelThresh,4);
 figure, imshow(dilatedImage);

% bounding boxes used for removing artifacts
 R = regionprops(dilatedImage, 'BoundingBox');
 for i = 1:length(R)
   rectangle('Position', R(i).BoundingBox,'EdgeColor','red');
     draws rectangles
end

cc = bwconncomp(dilatedImage);
 %extract all connected components where cc is an array.
%'Extent' property of regionprops gives the ratio between
 %region pixel and bounding box pixels. For wires, this
  ratio is very small. so we remove regions
%where this ratio is > 0.5 which happen to be artifacts
stats = regionprops(cc, 'Extent','PixelIdxList');
toRemove = [stats.Extent] > 0.9; %toRemove is an arrady and
   %of it is equal to no.of components in the image,
 % if statement is correct it stores 1
 % (true stores =1, false=0 )
newImg = dilatedImage;
for i=1:length(toRemove)
    if(toRemove(i)==1) % 1 is artificat
        newImg(stats(i).PixelIdxList) = 0;
       % changing intensity to 0, i
       % i.e removing the objects that are not wires,
      %  pixelidlist consists information
       %  of all the pixels of that components
    end
end
```

```
figure, imshow(newImg);

currentFileName
R = regionprops(newImg, 'BoundingBox');
% R is no. of components in the image
for j = 1:length(R)
     rectangle('Position', R(j).BoundingBox,'EdgeColor','red');
end

R = regionprops(newImg, 'BoundingBox','FilledArea');
counter=0;
for k = 1:length(R)
    p1X=R(k).BoundingBox(1);
    p1Y=R(k).BoundingBox(2);
    p2X=p1X+R(k).BoundingBox(3);
    p2Y=p1Y+R(k).BoundingBox(4);
    %length of wire is length of diagonal of bounding box found using
    %distance formula
    length_wire = sqrt( ((p2X-p1X)*(p2X-p1X)) + ((p2Y-p1Y)*(p2Y-p1Y)));
    width_wire = R(k).FilledArea / length_wire;
    recatangle-area= length*width
    fprintf(fileId,'%d\t%f\t%f\t%f\n',
            counter+1,length_wire,width_wire,R(k).FilledArea);
    counter = counter + 1;
    sumLength = sumLength + length_wire;
    sumWidth = sumWidth + width_wire;
    sumArea = sumArea + R(k).FilledArea;
    %avgCounter = avgCounter + 1;
end

avgLength = sumLength / counter;
```

```
    avgWidth = sumWidth / counter;
    avgArea = sumArea / counter;

fprintf(fileId,'\n%d\t%f\t%f\t%f\n\n\n\n\n\n\n\n\n',
                counter,avgLength,avgWidth,avgArea);
end
fclose(fileId);
```

# Appendix B Procedures

## 1. Wafer Cleaning

Silicon wafers require cleaning before the growth of an oxide layer on the surface. The cleaning steps are intended to remove contaminants present on the surface, passivate the surface and dry the surface without roughening.

Contaminants: There are three different types of contaminants that predominantly affect the surface. They are organics, metals and native oxide.

- Organics: These contaminants are due to skin oils, resist and polymers. They arise due to room air, residue left from the resist and improper cleaning of storage boxes. These contaminants affect oxidation rates and interface properties.
- Metals: Metal contaminants are primarily due to alkali ions and heavy transition metals. These arise during processing steps like chemical plasma etching or ion implantation. These contaminants induce leakage currents and interface trapped charge states.
- Native Oxide: Silicon reacts with the oxygen present in the atmosphere and grows an approximately 1 nm thick oxide layer on the surface of the substrate. This oxide is impure and highly prone to leakage current and induces ion mobility.

The procedure followed for the cleaning of silicon wafers is described below. This procedure in the semiconductor industry is widely known as RCA clean [65].

1. A solution is prepared consisting of $NH_4OH$, $H_2O_2$ and $H_2O$.
   - 5 parts of deionized water ($H_2O$)

- 1 part of aqueous ammonium hydroxide ($NH_4OH$)
- 1 part of aqueous hydrogen peroxide ($H_2O_2$)

Wafers are treated with the above solution for 5 mins at room temperature. This step removes organic residues. Particles are also very effectively removed. This treatment results in the formation of a thin silicon dioxide layer ($\sim$ 1 nm) on the silicon surface, along with certain metallic contamination that can be removed in the subsequent cleaning steps.

2. Triple rinse in DI ($H_2O$) water for 3 mins. Rinsing removes all traces of previous chemicals.

3. A solution is prepared consisting of HF and $H_2O$

   - 1 part of 49% concentrated hydrofluoric acid (HF)
   - 100 parts of deionized water ($H_2O$)

   Wafers are immersed in the above solution for 2 mins to remove the thin oxide and some fraction of ionic contaminants. HF will passivate the silicon surface with a H termination. Passivation reduces organic pickup from the air.

4. Triple rinse in DI ($H_2O$) water for 3 mins. Rinsing removes all traces of previous chemicals.

5. Repeat steps 1, 2, 3 and 4 again.

6. Final step involves blow drying of the wafers using $N_2$ gas.

# 2. Dry Oxidation

Thermal oxidation, familiarly known as dry oxidation in the microelectronic industry, is the most common way to produce a thin layer of high quality oxide on the surface of a wafer. For the present study a Thermcraft horizontal furnace was used to grow high quality $SiO_2$ of 1.5 nm on the surface of Si substrates. The dry oxidation setup and wafer cassettes used are shown in Fig B.1 (a),(b).

## 2.1 Procedure

The steps involved in the oxide growth process in the time domain are shown in Fig. B.2(a) and the possible defects that could be formed are shown in Fig B.2 (b). The general procedure followed for the growth of high quality oxide on silicon wafers is explained below:

- Turn on the furnace and let the furnace reach the set temperature. The set temperature is generally lower than the oxide growth(desired) temperature. Wafers will be pushed into the furnace at the set temperature and will be oxidized at the desired temperature.

- Turn on $N_2$ + 5% $O_2$ gas at the set temperature. Flow rate of the gases is low since the load lock is closed.

- Arrange the wafers in the cassette (shown in Fig B.1(b)). Place the actual wafers at the center of the cassette along with the dummy wafers at both the ends. Turn off $N_2$ gas flow.

- Once the desired temperature is achieved, open the load lock and transfer the wafer cassette into the center of the furnace. Turn on $O_2$ gas flow and increase

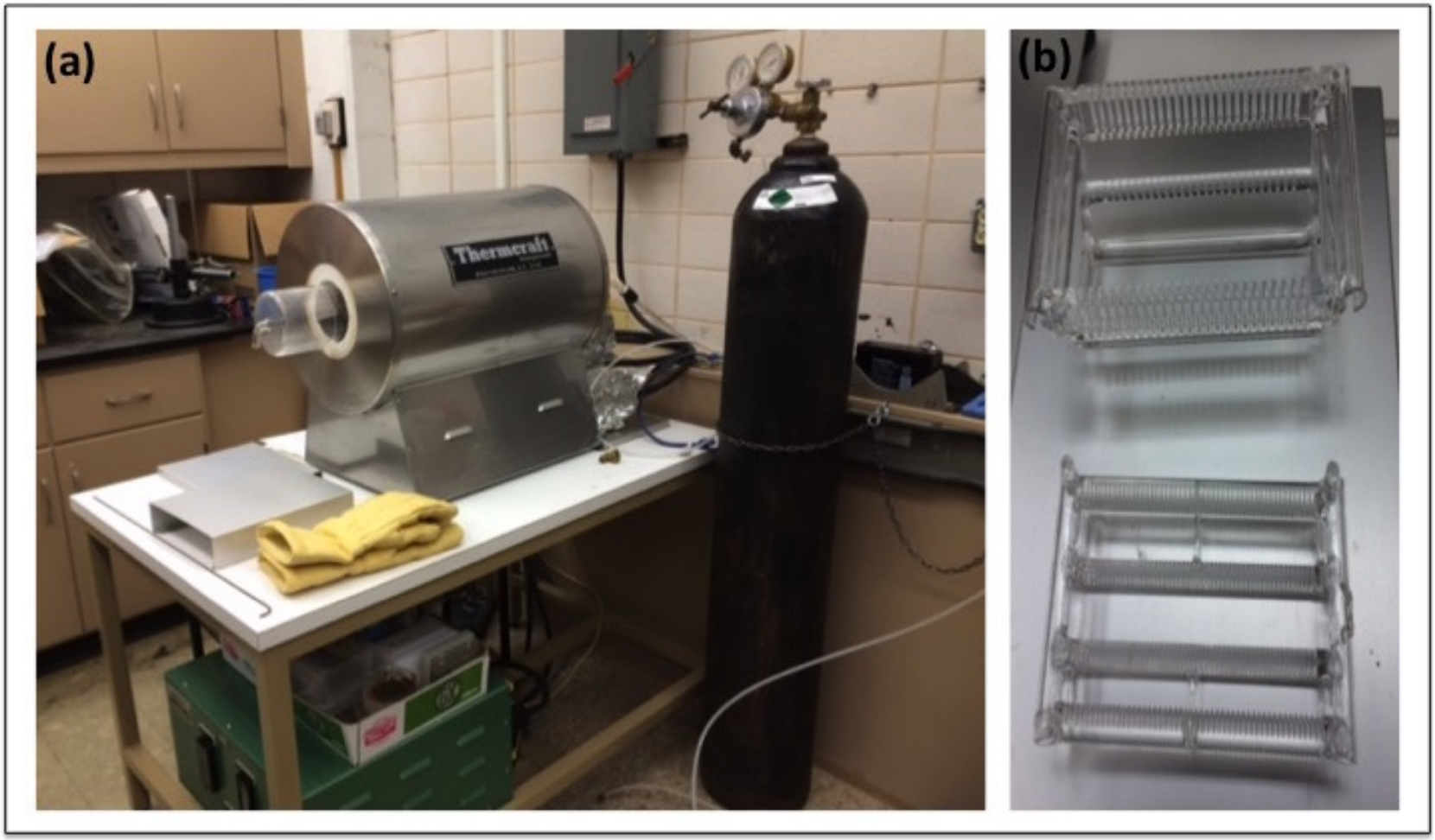


Figure B.1: (a) Dry oxidation apparatus consisting of Thermcraft horizontal surface and oxygen gas tank connected to it. (b) Cassettes used for handling 3 mm wafers.

the flow rate to high.

- Wait for the oxidation to complete. Time required to achieve required thickness can be calculated using Deal-Grove formula[121]. Monitor temperature and gas flow rate.

- Once the desired oxide growth is achieved, ramp down the temperature to the prior set point temperature. Turn off $O_2$ gas flow and turn on $N_2$ gas flow.

- Pull the wafers to the end of the furnace. Let them cool down for a while ($\sim$ 10-15 mins) and pull them out.

- Turn off $O_2$ gas flow and switch off the power supply of the furnace.

A thin $SiO_2$ layer of 1.5 nm was grown on silicon substrate in the hot furnace at 200 °C for 2 hours. The wafers were pushed and pulled at 200 °C .

The possible electrical defects that could be generated during the growth process are interface traps, fixed charge states and trap states. Interface trapped charge states are dangling Si bonds present in the silicon that stick into the silicon dioxide. Fixed charge states are incompletely oxidized silicon. If the silicon is not fully oxidized it gives rise to fixed charge states in the surface widely known as fixed charges states or surface charge states. Oxide trapped charge states are present in the bulk due to broken Si-O bonds. Defects could also arise due to contaminants like $Na^+$ and $K^+$ ions. To minimize the effect due to positive mobile ions ($Na^+$, $K^+$) a small quantity of HCl is used. Cl reacts with mobile ions and neutralizes them. It will increase amount of Cl in the oxide film but this is minor compared to eliminating mobile ions. Interface traps, fixed charge states and oxide trapped states are formed due to stress the wafers experience during ramping up, ramping down, loading and unloading of wafers.To minimize the surface charge state effects $N_2$ gas is used during

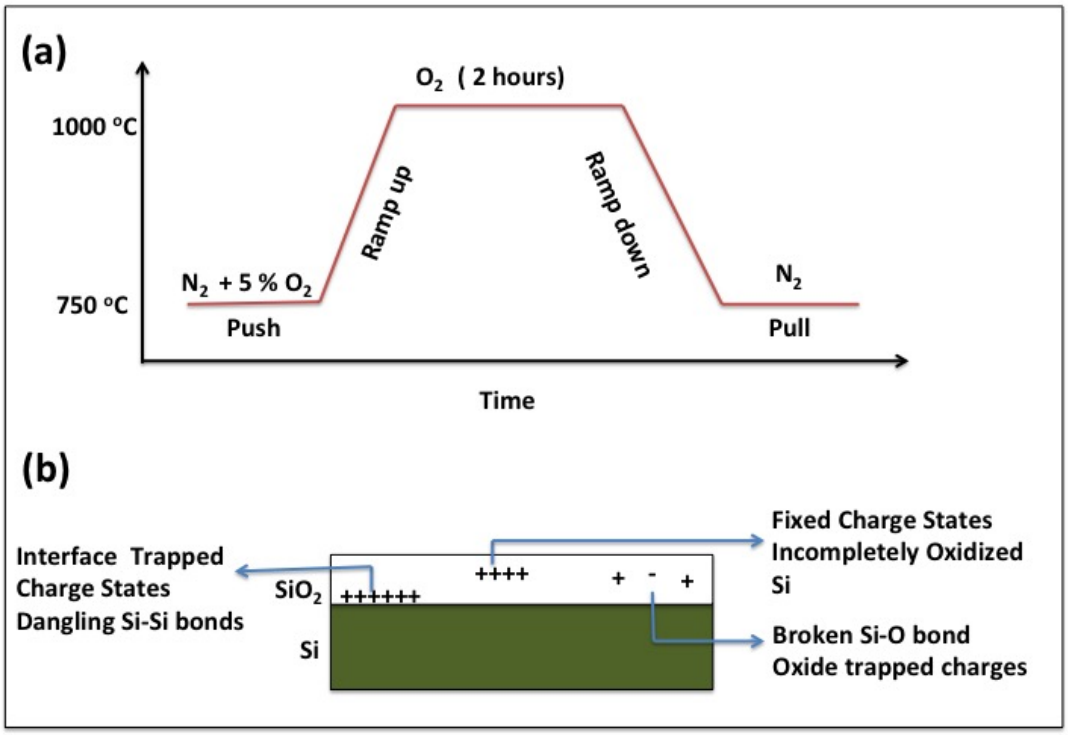


Figure B.2: (a) Dry oxidation growth process. (b) Electrical defects generated during oxide growth

ramp up and ramp down processes. Additional 5%$O_2$ gas was used during the ramp up process to prevent the formation of SiN.

## 2.2 Oxide Growth Kinetics

In this section the growth kinetics and percentage of the oxide layer consumed by the silicon surface are discussed. Oxide growth is diffusion controlled growth kinetics. As soon as the surface is completely oxidized further oxidation will only occur if the oxygen atoms diffuse through the oxide layer to react with the semiconductor at the semiconductor/oxide interface.

$$Si + O_2 = SiO_2 \tag{2}$$

where the molecular weights of Si, $O_2$ and $SiO_2$ are 28, 32 and 60 grams.

$$M = V * \rho_{SiO_2} \tag{3}$$

where M is mass, V is volume and $\rho$ represents density of material

$$M = A * t * \rho_{SiO_2} \tag{4}$$

where t is the thickness of film and A is area of the film

$$t = \frac{M}{A * \rho_{SiO_2}} \tag{5}$$

$$t_{SiO_2} = \frac{M_{SiO_2}}{A * 2.27} \tag{6}$$

$$t_{Si} = \frac{M_{Si}}{A * 2.33} \tag{7}$$

From Equations 3.5 and 3.6 we have

$$\frac{t_{SiO_2}}{t_{Si}} = \frac{M_{Si} * 2.27}{M_{SiO_2} * 2.33} \tag{8}$$

$$\frac{t_{SiO_2}}{t_{Si}} \approx 0.45 \tag{9}$$

The above result implies that 45% of $SiO_2$ is consumed by the silicon substrate.

# 3. Electron Beam Evaporation

Figure B.3 shows the electron beam evaporator used, i.e the a Mcllister Ebeam Evaporator (EVAP). Current ($I_{filament}$) is applied to a tungsten filament to generate free electrons. The potential difference between the filament and the crucible that holds metal(evaporation source) accelerates the electrons towards the crucible. For our depositions Cu pellets were placed inside the crucible. The electron bombardment led to evaporation of the Cu metal. The evaporated Cu will travel in vacuum with minimum (almost zero) scattering and settle on the substrate (Si sample). The flux of atoms reaching the substrate is monitored and controlled using a flux meter. Since such Cu flux is not a good quantitative measure of film thickness, an SEM-EDAX measurement was used to find the average surface coverage of Cu in monolayers. The areas, lengths and widths of nanostructures that resulted from the Cu depositions were analyzed using SEM images and analysis of the images using Matlab.

The electron beam evaporation gun operating procedure is explained below.

- Load the crucible with pure Cu pellets. Check the electrical connections and make sure there is no grounding issue.[Note: This was a common equipment problem]

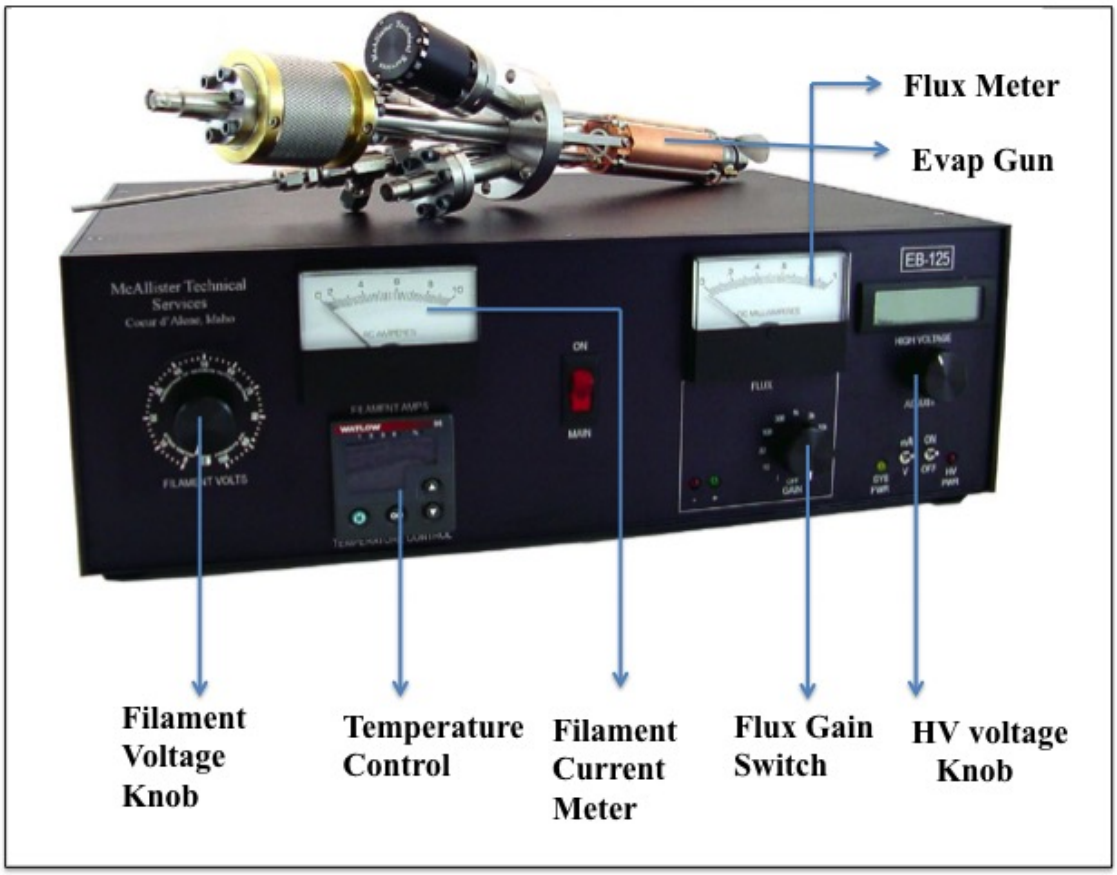


Figure B.3: McAllister electron beam evaporation system. Figure adapted from [122].

- Retract the linear translator away from the evaporator flange. Make sure the shutter is closed.
- Turn on the vacuum pump and wait until the pressure is stabilized. Pressure in the vaccum chamber should be $< 1$ X $10^{-6}$ Torr.
- Turn on the main power supply.
- Connect the water lines and initiate flow.
- Increase the filament current slowly in short increments. Increase slowly until the filament Amps meter displays $\approx$ 5A.
- Switch HV power on, adjust to $\sim$ 800-1000V.
- Move the crucible with the linear translator to a position resulting in maximum indicated emission current.
- Adjust the filament voltage to obtain $\sim$50 mA emission current.
- Wait until the flux monitor reading has stabilized.
- Open the shutter.
- Start evaporating (depositing) until the required thickness is achieved(based on time).
- Close the shutter.
- Retract the linear translator away from the evaporator flange.
- Slowly decrease the filament current to zero.
- Slowly decrease the HV voltage.

- Turn off water lines.
- Wait at least 2 hours for the sample to cool.
- Vent the chamber and unload the sample.

# Appendix C Beam Profiles

To estimate current density on the sample for measurements with ions from the EBIT source, beam profiles were measured with a Faraday cup (FC 2). Beam profiles were measured by translating the Faraday cup in the same plane as the sample with a step-size no greater than 20 mils. The beam profiles, shown in Fig. C.1 to Fig .C.3, were typically Gaussian with a FWHM of ∼1.5mm.

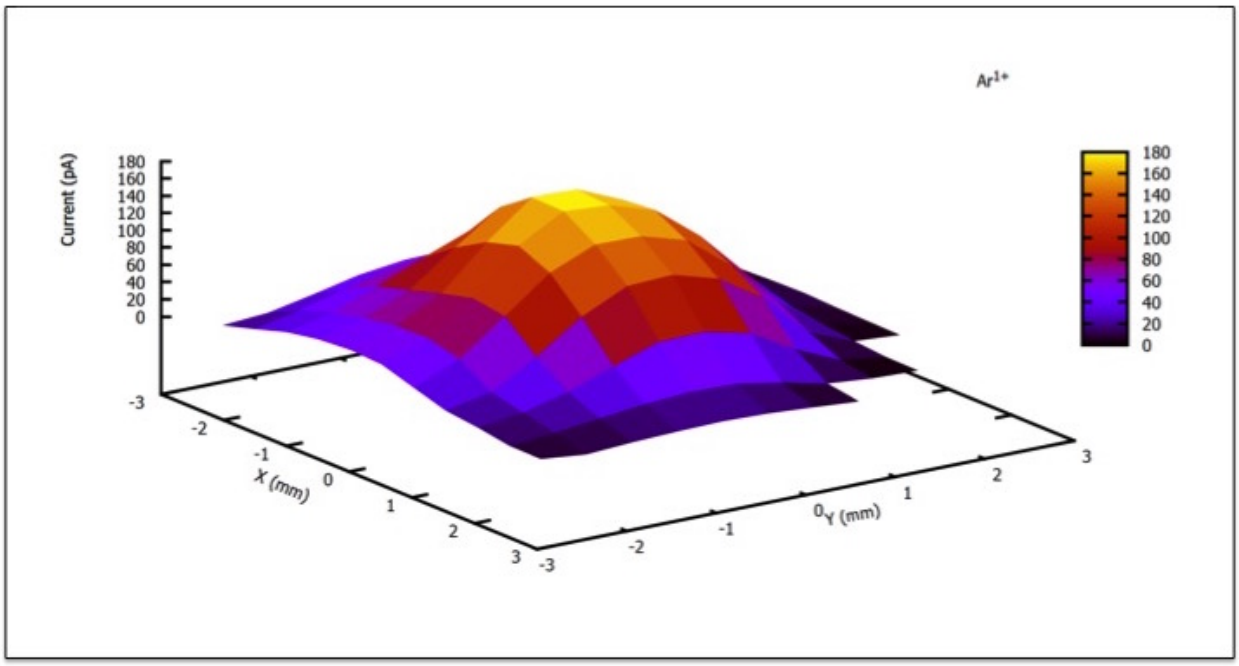


Figure C.1: Beam profile of $Ar^{1+}$ ion.

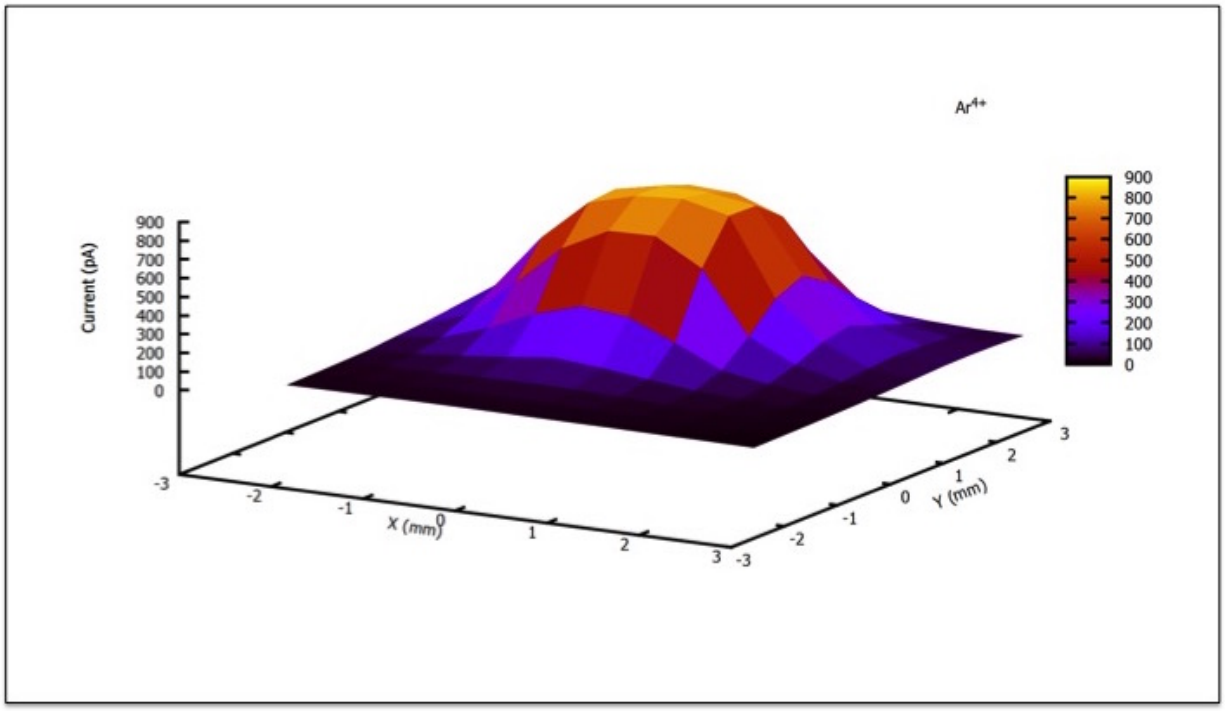


Figure C.2: Beam profile of $Ar^{4+}$ ion.

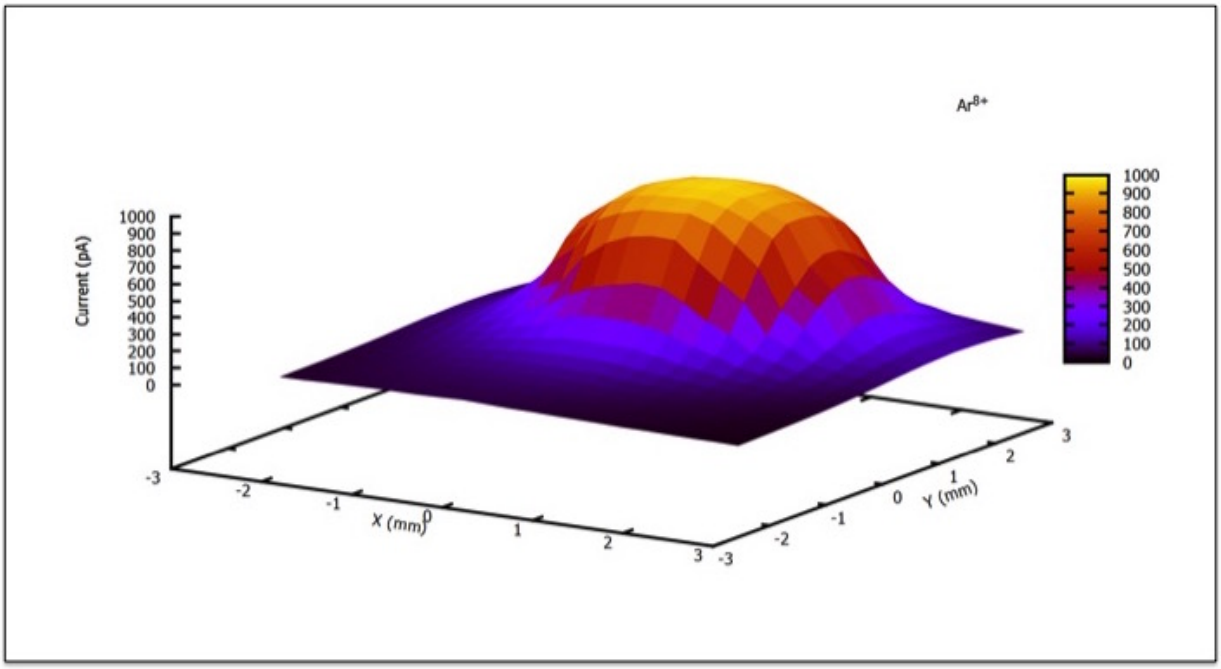


Figure C.3: Beam profile of $Ar^{8+}$ ion.

# Bibliography


[1] F. Deng, R. A. Johnson, P. M. Asbeck, S. S Lau, W. B. Dubbelday, T. Hsiao, and J. Woo. *Journal of Applied Physics*, 81(12):8047–8051, 1997. ISSN 0021-8979.

[2] H. Iwai, T. Ohguro, and S. Ohmi. *Microelectronic Engineering*, 60(1-2):157–169, 2002. ISSN 0167-9317.

[3] Y. Ichikawa, M. Kobayashi, M. Sasase, and T. Suemasu. *Applied Surface Science*, 254(23):7963–7967, 2008. ISSN 0169-4332.

[4] S. H. Brongersma, M. R. Castell, D. D. Perovic, and M. Zinke-Allmang. *Physical Review Letters*, 80(17):3795–3798, 1998. ISSN 0031-9007.

[5] J. C. Mahato, Debolina Das, R. R. Juluri, R. Batabyal, Anupam Roy, P. V. Satyam, and B. N. Dev. *Applied Physics Letters*, 100(26), 2012. ISSN 0003-6951.

[6] H. F. Hsu, T. F. Chiang, H. C. Hsu, and L. J. Chen. *Japanese Journal of Applied Physics Part 1-Regular Papers Short Notes & Review Papers*, 43(7B): 4541–4544, 2004. ISSN 0021-4922.

[7] S. Y. Chen and L. J. Chen. *Applied Physics Letters*, 87(25), 2005. ISSN 0003-6951.

[8] P Muret, K Lefki, T T A Nguyen, A Cola, and I Ali. *Semiconductor Science and Technology*, 9(7):1395, 1994.

[9] Fang-Wei Yuan, Chiu-Yen Wang, Guo-An Li, Shu-Hao Chang, Li-Wei Chu, Lih-Juann Chen, and Hsing-Yu Tuan. *Nanoscale*, 5:9875–9881, 2013.

[10] J. X. Xu, R. H. Yao, and K. W. Geng. *Journal of Vacuum Science & Technology A*, 29(5), 2011. ISSN 0734-2101.

[11] N. C. Cirillo, H. K. Chung, P. J. Vold, M. K. Hibbsbrenner, and A. M. Fraasch. *Journal of Vacuum Science & Technology B*, 3(6):1680–1684, 1985.

[12] S. P. Murarka. *Journal of Vacuum Science & Technology*, 17(4):775–792, 1980. ISSN 0022-5355.

[13] S. P. Murarka, M. H. Read, C. J. Doherty, and D. B. Fraser. *Journal of the Electrochemical Society*, 129(2):293–301, 1982. ISSN 0013-4651.

[14] S. Y. Chen, H. C. Chen, and L. J. Chen. *Applied Physics Letters*, 88(19), 2006. ISSN 0003-6951.

[15] P. G. McCafferty, A. Sellai, P. Dawson, and H. Elabd. *Solid-State Electronics*, 39(4):583–592, 1996. ISSN 0038-1101.

[16] D. Lee, D. K. Lim, S. S. Bae, S. Kim, R. Ragan, D. A. A. Ohlberg, Y. Chen, and R. S. Williams. *Applied Physics a-Materials Science Processing*, 80(6): 1311–1313, 2005. ISSN 0947-8396.

[17] Kaiqi Xu, Yu He, Liubin Ben, Hong Li, and Xuejie Huang. *Journal of Power Sources*, 281:455 – 460, 2015. ISSN 0378-7753.

[18] Y. T. Bie, J. L. Yu, J. Yang, W. Lu, Y. N. Nuli, and J. L. Wang. *Electrochimica Acta*, 178:65–73, 2015. ISSN 0013-4686.

[19] K. Q. Xu, Y. He, L. B. Ben, H. Li, and X. J. Huang. *Journal of Power Sources*, 281:455–460, 2015. ISSN 0378-7753.

[20] F. W. Yuan, C. Y. Wang, G. A. Li, S. H. Chang, L. W. Chu, L. J. Chen, and H. Y. Tuan. *Nanoscale*, 5(20):9875–9881, 2013. ISSN 2040-3364.

[21] J. B. Zhou, N. Lin, Y. Han, J. Zhou, Y. C. Zhu, J. Du, and Y. T. Qian. *Nanoscale*, 7(37):15075–15079, 2015. ISSN 2040-3364.

[22] C. Y. Wen, M. C. Reuter, J. Tersoff, E. A. Stach, and F. M. Ross. *Nano Letters*, 10(2):514–519, 2010. ISSN 1530-6984.

[23] D. Fink, P. S. Alegaonkar, A. V. Petrov, M. Wilhelm, P. Szimkowiak, A. Behar, D. Sinha, W. R. Fahrner, K. Hoppe, and L. T. Chadderton. *Nuclear Instruments & Methods in Physics Research Section B-Beam Interactions with Materials and Atoms*, 236:11–20, 2005. ISSN 0168-583X.

[24] G. M. Wallner, W. Platzer, and R. W. Lang. *Solar Energy*, 79(6):583–592, 2005. ISSN 0038-092X.

[25] M. R. Cleland, L. A. Parks, and S. Cheng. *Nuclear Instruments & Methods in Physics Research Section B-Beam Interactions with Materials and Atoms*, 208: 66–73, 2003. ISSN 0168-583X.

[26] Milton Ohring. volume Academic Press, ISBN: 0-12-524990-X. 1992.

[27] E. Bauer and J. H. Vandermerwe. *Physical Review B*, 33(6):3657–3671, 1986. ISSN 0163-1829.

[28] E. Bauer and H. Poppa. *Thin Solid Films*, 12(167), 1972.

[29] G. D. T Spiller A. Venables and M. Hanbucken. *Curr. Top. Mater. Sci.*, 3(139), 1979.

[30] Brown R Barlow F, Elshabini-Riad A. *New York: McGraw Hill*, 1998.

[31] Robin F.C. *New York: William Andrew Inc*, 1995.

[32] Adachi H. Wasa K, Kitabatake M, 2004.

[33] Mattox D M. *New York: William Andrew Inc*, 1998.

[34] Krisna Seshan. *New York:WILLIAM ANDREW PUBLISHING*, 2002.

[35] Jensen K.F. Hitchman M.L. *New York: Academic Press Ltd*, 1993.

[36] S. A. Chaparro, Y. Zhang, J. Drucker, D. Chandrasekhar, and D. J. Smith. *Journal of Applied Physics*, 87(5):2245–2254, 2000. ISSN 0021-8979.

[37] Ju Wu and Peng Jin. *Frontiers of Physics*, 10(1):7–58, 2015. ISSN 2095-0462.

[38] A. M. Yaremko, V. M. Dzhagan, P. M. Lytvyn, V. O. Yukhymchuk, and M. Y. Valakh. *Physica Status Solidi B-Basic Solid State Physics*, 242(14):2833–2837, 2005. ISSN 0370-1972.

[39] D. Lee and S. Kim. *Applied Physics Letters*, 82(16):2619–2621, 2003. ISSN 0003-6951.

[40] Y. Chen, D. A. A. Ohlberg, and R. S. Williams. *Journal of Applied Physics*, 91 (5):3213–3218, 2002. ISSN 0021-8979.

[41] C. Preinesberger, G. Pruskil, S. K. Becker, M. Dahne, D. V. Vyalikh, S. L. Molodtsov, C. Laubschat, and F. Schiller. *Applied Physics Letters*, 87(8), 2005. ISSN 0003-6951.

[42] Y. Chen, D. A. A. Ohlberg, G. Medeiros-Ribeiro, Y. A. Chang, and R. S. Williams. *Applied Physics Letters*, 76(26):4004–4006, 2000. ISSN 0003-6951.

[43] J. Nogami, B. Z. Liu, M. V. Katkov, C. Ohbuchi, and N. O. Birge. *Physical Review B*, 63(23):art. no.–233305, 2001. ISSN 1098-0121.

[44] R. Ragan, Y. Chen, D. A. A. Ohlberg, G. Medeiros-Ribeiro, and R. S. Williams. *Journal of Crystal Growth*, 251(1-4):657–661, 2003. ISSN 0022-0248.

[45] Zhou Zhang, Lai Mun Wong, Hock Guan Ong, Xin Jiao Wang, Jun Ling Wang, Shi Jie Wang, Hongyu Chen, and Tom Wu. *Nano Letters*, 8(10):3205–3210, 2008. ISSN 1530-6984.

[46] L. J. Chen and K. N. Tu. *Materials Science Reports*, 6(2-3):53–140, 1991. ISSN 0920-2307.

[47] K. C. R. Chiu, J. M. Poate, J. E. Rowe, T. T. Sheng, and A. G. Cullis. *Applied Physics Letters*, 38(12):988–990, 1981. ISSN 0003-6951.

[48] J. Tersoff and R. M. Tromp. *Physical Review Letters*, 70(18):2782–2785, 1993. ISSN 0031-9007.

[49] D. E. Jesson, G. Chen, K. M. Chen, and S. J. Pennycook. *Physical Review Letters*, 80(23):5156–5159, 1998. ISSN 0031-9007.

[50] K. Sekar, G. Kuri, P. V. Satyam, B. Sundaravel, D. P. Mahapatra, and B. N. Dev. *Physical Review B*, 51(20):14330–14336, 1995. ISSN 1098-0121.

[51] Z. A. He, D. J. Smith, and P. A. Bennett. *Physical Review Letters*, 93(25), 2004. ISSN 0031-9007.

[52] Hitachi. *SEM-Hitachi-S-4800-Instruction-Manual*.

[53] Bragg W.L. *Proceedings of the Cambridge Philosophical Society 1912*, pages 43–57.

[54] SOPRA. *GES5 Goniometer Ellipsometer Spectroscopic, 5th Generation*.

[55] Taher M. El-Agez, Ahmed A. El Tayyan, and Sofyan A. Taya. *Thin Solid Films*, 518(19):5610 – 5614, 2010. ISSN 0040-6090.

[56] W. C. Dash. *Journal of Applied Physics*, 27(10):1193–1195, 1956.

[57] S. X. Song, Y. Z. Liu, D. L. Mao, H. Q. Ling, and M. Li. *Thin Solid Films*, 476 (1):142–147, 2005. ISSN 0040-6090.

[58] J. nmahori, T. Oku, and M. Murakami. *Thin Solid Films*, 301(1-2):142–148, 1997. ISSN 0040-6090.

[59] M. A. Nicolet. *Thin Solid Films*, 52(3):415–443, 1978. ISSN 0040-6090.

[60] Jan echal, Josef Polk, Miroslav Kolbal, Petr Bbor, and Tom ikola. *Applied Surface Science*, 256(11):3636 – 3641, 2010. ISSN 0169-4332.

[61] Shaozhou Li, Hui Cai, Chee Lip Gan, Jun Guo, Zhili Dong, and Jan Ma. *Crystal Growth & Design*, 10(7):2983–2989, 2010. ISSN 1528-7483.

[62] Poh-Keong Ng, Jian-Yih Cheng, B. Fisher, and C.M. Lilley. pages 67–70, Oct 2012. doi: 10.1109/NMDC.2012.6527589.

[63] Nitin Kumar, Omkar Parajuli, and Jong-in Hahm. *Applied Physics Letters*, 91 (14), 2007. ISSN 0003-6951.

[64] Omkar Parajuli, Nitin Kumar, Dylan Kipp, and Jong-In Hahm. *Applied Physics Letters*, 90(17), 2007. ISSN 0003-6951.

[65] Puotinen D. Kern, W. *RCA Review*, 31(187), 1970.

[66] G. Weber, B. Gillot, and P. Barret. *Physica Status Solidi a-Applied Research*, 75(2):567–576, 1983. ISSN 0031-8965.

[67] J. K. Solberg. *Acta Crystallographica Section A*, 34(SEP):684–698, 1978. ISSN 0108-7673.

[68] R. R. Chromik, W. K. Neils, and E. J. Cotts. *Journal of Applied Physics*, 87 (9):U3–U3, 2000. ISSN 0021-8979.

[69] M. Mundschau, E. Bauer, W. Telieps, and W. Swiech. *Journal of Applied Physics*, 65(12):4747–4752, 1989. ISSN 0021-8979.

[70] D.J.Fisher.

[71] Thomas Adam. *Lecture Notes, Introduction to MEMS(Microtechnology)*. Rose-Hauman Institute of Technology, Indiana, USA.

[72] Mitsuhiro Shikida, Kazuo Sato, Kenji Tokoro, and Daisuke Uchikawa. *Sensors and Actuators A: Physical*, 80(2):179 – 188, 2000. ISSN 0924-4247.

[73] Osamu Tabata, Ryouji Asahi, Hirofumi Funabashi, Keiichi Shimaoka, and Susumu Sugiyama. *Sensors and Actuators A: Physical*, 34(1):51 – 57, 1992. ISSN 0924-4247.

[74] J T Yates Jr. *Journal of Physics: Condensed Matter*, 3(S):S143, 1991.

[75] M. Uematsu H. Hibino and Y. Watanabeb. *Journal of Applied Physics*, 100, 2006. ISSN 113519.

[76] J D Gillaspy, J M Pomeroy, A C Perrella, and H Grube. *Journal of Physics: Conference Series*, 58(1):451, 2007.

[77] H. Hibino, M. Uematsu, and Y. Watanabe. *Journal of Applied Physics*, 100 (11), 2006. ISSN 0021-8979.

[78] K. Hofmann, G. W. Rubloff, and R. A. McCorkle. *Applied Physics Letters*, 49 (22):1525–1527, 1986. ISSN 0003-6951.

[79] R. Shyam, D. D. Kulkarni, D. A. Field, E. S. Srinadhu, D. B. Cutshall, W. R. Harrell, J. E. Harriss, and C. E. Sosolik. *AIP Conference Proceedings*, 1640(1), 2015.

[80] DREBIT. *A New Generation of Powerful Ion Sources for Medical Particle Therapy*, 2008.

[81] J. Burgdörfer, C. Reinhold, L. Hägg, and F. Meyer. Interaction of highly charged ions with surfaces. *Aust. J. Phys.*, pages 527–542, 1996.

[82] J. Burgdörfer and F. Meyer. *Phys. Rev. A*, 47:R20–R22, 1993.

[83] J. Burgdörfer, P. Lerner, and F. W. Meyer. *Phys. Rev. A*, 44(9):5674, 1991.

[84] Masahide Tona, Satoshi Takahashi, Kazuo Nagata, Nobuo Yoshiyasu, Chikashi Yamada, Nobuyuki Nakamura, Shunsuke Ohtani, and Makoto Sakurai. *Applied Physics Letters*, 87(22):224102, 2005.

[85] L. J. Chen, C. S. Liu, and J. B. Lai. *Materials Science in Semiconductor Processing*, 7(3):143–156, 2004. ISSN 1369-8001.

[86] Y. Meng, F. Ma, Z. X. Song, Y. H. Li, and K. W. Xu. *RSC Adv.*, 6:844–850, 2016. doi: 10.1039/C5RA20864E.

[87] M. N. Murakhmetov I. S. Bitenskii and E. S. Parilis. *Sov. Phys. Tech. Phys.*, 24(618), 1979.

[88] Yasunori Yamazaki and Kenro Kuroki. *Current Opinion in Solid State and Materials Science*, 6(2):169 – 179, 2002. ISSN 1359-0286.

[89] Masahide Tona, Satoshi Takahashi, Kazuo Nagata, Nobuo Yoshiyasu, Chikashi Yamada, Nobuyuki Nakamura, Shunsuke Ohtani, and Makoto Sakurai. *Applied Physics Letters*, 87(22):224102, 2005. doi: http://dx.doi.org/10.1063/1.2136361.

[90] J. F. Ziegler, J. P. Biersack, and U. Littmark. *The stopping and ranges of ions in matter*. Pergamon, New York, 1985.

[91] Ben W. Muir, Sally L. McArthur, Helmut Thissen, George P. Simon, Hans J. Griesser, and David G. Castner. *Surface and Interface Analysis*, 38(8):1186–1197, 2006. ISSN 0142-2421.

[92] B. Jaleh, P. Parvin, N. Sheikh, M. Hajivaliei, and E. Hasani. *Surface & Coatings Technology*, 203(17-18):2759–2762, 2009. ISSN 0257-8972.

[93] Sina Burkert, Marco Kuntzsch, Cornelia Bellmann, Petra Uhlmann, and Manfred Stamm. *Applied Surface Science*, 255(12):6256–6261, 2009. ISSN 0169-4332.

[94] C. Darraud, B. Bennamane, C. Gagnadre, J. L. Decossas, and J. C. Vareille. *Polymer*, 35(11):2447–2451, 1994. ISSN 0032-3861.

[95] R. Navarro-Gonzalez, P. Coll, and R. Aliev. *Polymer Bulletin*, 48(1):43–51, 2002. ISSN 0170-0839.

[96] K. Hareesh, C. Ranganathaiah, P. Ramya, R. Bhargavi, Geetha G. Nair, Sangappa, and Ganesh Sanjeev. *Journal of Applied Polymer Science*, 127(3):2010–2018, 2013. ISSN 0021-8995.

[97] A. Srivastava, T. V. Singh, S. Mule, C. R. Rajan, and S. Ponrathnam. *Nuclear Instruments & Methods in Physics Research Section B-Beam Interactions with Materials and Atoms*, 192(4):402–406, 2002. ISSN 0168-583X.

[98] A. Poirier, G. G. Ross, P. Bertrand, and V. Wiertz. volume 504 of *Materials Research Society Symposium Proceedings*, pages 425–430, 1998. ISBN 1-55899-409-2.

[99] Bhupendra Singh Rathore, Mulayam Singh Gaur, and Kripa Shanker Singh. *Journal of Thermal Analysis and Calorimetry*, 111(1):647–653, 2013. ISSN 1388-6150.

[100] Ziqiang Zhao, Yingmin Liu, Junfeng Dai, and Yan Chen. *Nuclear Instruments & Methods in Physics Research Section B-Beam Interactions with Materials and Atoms*, 262(2):205–208, 2007. ISSN 0168-583X.

[101] H. Dong and T. Bell. *Surface & Coatings Technology*, 111(1):29–40, 1999. ISSN 0257-8972.

[102] R. L. Clough. *Nuclear Instruments & Methods in Physics Research Section B-Beam Interactions with Materials and Atoms*, 185:8–33, 2001. ISSN 0168-583X.

[103] H. Biederman, D. Slavinska, H. Boldyreva, H. Lehmberg, G. Takaoka, J. Matsuo, H. Kinpara, and J. Zemek. *Journal of Vacuum Science & Technology B*, 19(6):2050–2056, 2001. ISSN 1071-1023.

[104] P. K. Goyal, V. Kumar, Renu Gupta, S. Mahendia, Anita, and S. Kumar. *Vacuum*, 86(8):1087–1091, 2012. ISSN 0042-207X.

[105] H. Kupfer and G. K. Wolf. *Nuclear Instruments & Methods in Physics Research Section B-Beam Interactions with Materials and Atoms*, 166:722–731, 2000. ISSN 0168-583X.

[106] T. Asmus and G. K. Wolf. *Nuclear Instruments & Methods in Physics Research Section B-Beam Interactions with Materials and Atoms*, 166:732–736, 2000. ISSN 0168-583X.

[107] B. S. Elman, D. J. Sandman, and M. A. Newkirk. *Applied Physics Letters*, 46 (1):100–102, 1985. ISSN 0003-6951.

[108] B. J. Bachman and M. J. Vasile. *Journal of Vacuum Science & Technology a-Vacuum Surfaces and Films*, 7(4):2709–2716, 1989. ISSN 0734-2101.

[109] G. S. Chang, K. H. Chae, C. N. Whang, E. Z. Kurmaev, D. A. Zatsepin, R. P. Winarski, D. L. Ederer, A. Moewes, and Y. P. Lee. *Applied Physics Letters*, 74 (4):522–524, 1999. ISSN 0003-6951.

[110] K. A. Zimmerman, S. C. Langford, J. T. Dickinson, and R. P. Dion. *Journal of Polymer Science Part B-Polymer Physics*, 31(9):1229–1243, 1993. ISSN 0887-6266.

[111] G. Zschornack, V. P. Ovsyannikov, F. Grossmann, A. Schwan, and F. Ullmann. *Journal of Instrumentation*, 5, 2010. ISSN 1748-0221.

[112] F. Dehaye, E. Balanzat, E. Ferain, and R. Legras. *Nuclear Instruments & Methods in Physics Research Section B-Beam Interactions with Materials and Atoms*, 209:103–112, 2003. ISSN 0168-583X.

[113] A. Poirier and G. G. Ross. volume 3413 of *Proceedings of the Society of Photo-Optical Instrumentation Engineers (Spie)*, pages 235–244. 1998. ISBN 0-8194-2867-1.

[114] Friedrich Aumayr, Stefan Facsko, Ayman S. El-Said, Christina Trautmann, and Marika Schleberger. *Journal of Physics-Condensed Matter*, 23(39), 2011. ISSN 0953-8984.

[115] M. R. Adams and A. Garton. *Polymer Degradation and Stability*, 41(3):265–273, 1993. ISSN 0141-3910.

[116] D.K.Davis. *Journal of Physics,D:Applied Physics*, 2, 1969. ISSN 1533-1537.

[117] K Kuroki, T Takahira, Y Tsuruta, N Okabayashi, T Azuma, K Komaki, and Y Yamazaki. *Physica Scripta*, 1999(T80B):557, 1999.

[118] O. Vilkov, A. Fedorov, D. Usachov, L. V. Yashina, A. V. Generalov, K. Borygina, N. I. Verbitskiy, A. Grüneis, and D. V. Vyalikh. *Scientific Reports*, 3:2168 EP –, 07 2013.

[119] Shih-Wei Hung, Terry Tai-Jui Wang, Li-Wei Chu, and Lih-Juann Chen. *The Journal of Physical Chemistry C*, 115(31):15592–15597, 2011.

[120] Chung-Yang Lee, Ming-Pei Lu, Kao-Feng Liao, Wei-Fan Lee, Chi-Te Huang, Sheng-Yu Chen, and Lih-Juann Chen. *The Journal of Physical Chemistry C*, 113(6):2286–2289, 2009.

[121] B. E. Deal and A. S. Grove. *Journal of Applied Physics*, 36(12), 1965.

[122] E-Beam Evaporator Manual. volume West 280 Prairie Avenue Coeur d'Alene. Idaho 83815.